

Damage Detection in Civil and Aerospace Structures with Fiber Optic Sensors

by

Niell Glen Elvin

Bsc. Engineering , University of the Witwatersrand
Johannesburg, South Africa (1994)

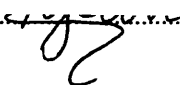
Submitted in partial fulfillment of the requirements for the degrees of

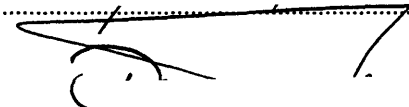
Master of Science in Civil and Environmental Engineering
and
Master of Science in Aeronautics and Astronautics

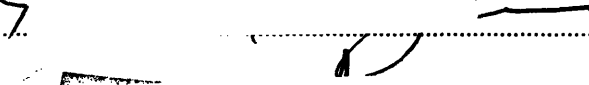
at the


MASSACHUSETTS INSTITUTE OF TECHNOLOGY
September 1995

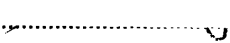
© Massachusetts Institute of Technology 1995. All rights reserved.

Author.....
Department of Civil and Environmental Engineering
and. Department of Aeronautics and Astronautics
August 11, 1995

Certified by
Assistant Professor Christopher K. Y. Leung
Thesis Supervisor

Certified by.....
Professor Paul A. Lagace
Thesis Supervisor

Accepted by
Professor Harold Y. Wachman
Chairman, Department Graduate Committee
Department of Aeronautics and Astronautics

Accepted by
Professor Joseph Sussman
Chairman, Department Committee on Graduate Students
Department of Civil and Environmental Engineering

MASSACHUSETTS INSTITUTE
OF TECHNOLOGY

OCT 25 1995

Barker Eng

LIBRARIES

Damage Detection in Civil and Aerospace Structures with Fiber Optic Sensors

by

Niell Glen Elvin

Submitted to the Department of Civil and Environmental Engineering
and
Department of Aeronautical and Astronautical Engineering
on August 11, 1995, in partial fulfillment of the
requirements for the degrees of
Master of Science in Civil and Environmental Engineering
and
Master of Science in Aeronautical and Astronautical Engineering

Abstract

The objective of this research is to investigate the performance of fiber optic sensing schemes that can accurately and reliably monitor the integrity and state of damage in civil and aerospace structures. The work presented in this thesis focuses on developing the combined electromagnetic and mechanical analysis required to study the behaviour of fiber optic sensing for two specific applications: (1) locating and monitoring tension cracks in concrete structures, and (2) detection of delamination cracks in composite and concrete structures.

Microbend fiber sensors that bridge the faces of tension cracks in concrete are studied as a possible means of determining the existence and extent of common damage in concrete structures. Delamination damage characterization by birefringent and interferometric sensors positioned parallel to delamination damage in typical aerospace composites and concrete structures is also investigated.

The microbend tension crack sensor was found to be able to detect cracks in the 0.01 mm crack opening range which makes them ideal for inspection of concrete structures. The study of delamination damage sensors showed the ability of these sensors to detect delamination crack lengths in the 1 mm rang making them suitable for monitoring delaminations in advanced composite flexural members. The delamination sensors investigated in this research have also shown potential use for structural integrity monitoring in reinforced concrete structures with 0.1 meter delamination lengths being detectable.

Thesis Supervisor: Christopher K. Y. Leung

Title: Assistant Professor of Civil and Environmental Engineering

Thesis Supervisor: Paul A. Lagace

Title: MacVicar Faculty Fellow, Professor of Aeronautics and Astronautics

Acknowledgments

This thesis is a tribute to all those who on hearing that I was doing a joint degree in civil and aerospace engineering remarked : 'What do you do, design runways ?' To my knowledge this is the first attempt (at least at MIT) of doing a joint degree in two such diverse branches of engineering. I hope that my effort warrants interest from others since I believe that there are important lessons to be learned from both sides.

For the opportunity of working in two departments, their interest, opinions and unique perspectives of the civil and aerospace industries I thank my supervisors Chris Leung and Paul Lagace.

I am as always grateful to the continued support of my parents through my long academic career. My brother deserves special thanks for being both a good friend and for providing invaluable advice. I recognize that without my family's help this thesis would not appear in its present form if at all.

I thank the many friends that help make MIT the special place it is.

Contents

1	Introduction	16
2	Electromagnetic Wave Propagation	19
2.1	Optical Wave guide Basics	19
2.1.1	Basic Electromagnetic Definitions	19
2.1.2	Wave Guide Definition	20
2.1.3	Wave Guide Characterization	20
2.2	Analysis of EM Transmission in a Slab Wave Guide	21
2.3	Solution of the Helmholtz Equation by the Beam Propagation Method	23
2.3.1	Formulation of the Beam Propagation Method	24
2.3.2	The Vassallo Finite Difference Beam Propagation Method . .	24
2.3.3	The FFT Beam Propagation Method	25
2.4	Solution of the Helmholtz equation for a Symmetric Slab Wave Guide	27
2.5	Solution of the BPM for a curved slab wave guide	29
2.6	Wave Guides used for Sensing	34
3	Mechanical Behaviour of an Optic Fiber Under Bending	42
3.1	Introduction	42
3.2	Physical Model of Fiber Matrix Interaction	43
3.3	The Finite Element Model	44
3.4	Finite Element Results	45
3.5	Beam on Elastic Foundation Analysis of Fiber Behaviour	47
3.6	Calculation of Equivalent Foundation Stiffness	50

4	Combined Mechanical and Electrical Behaviour of an Optic Fiber Under Bending	61
4.1	Introduction	61
4.2	Method of Combined Mechanical and Electrical Analysis	61
4.3	Results of the Combined Electro-Mechanical Analysis	63
4.3.1	Electric power Loss for Various Crack Opening Displacements and Fiber Orientations	63
4.3.2	Electric Power Loss for Various Jacket Stiffnesses	65
4.3.3	Electric Power Loss for Various Cut-off Frequencies	67
5	Discussion of Results and Recommendations	71
5.1	Summary of findings	71
5.1.1	Crack Opening	71
5.1.2	Jacket Stiffness	72
5.1.3	Cut-off Frequency	72
5.1.4	Fiber Orientation	73
5.2	Conclusion	73
6	Application of Fiber Optic Sensing in Delamination Detection	75
6.1	Introduction	75
6.2	Mechanics of delaminated flexural members	77
6.2.1	Introduction	77
6.2.2	Fundamental Equations in Complex Potential Plane Elasticity Theory	77
6.2.3	Derivation of Complex Potentials for the Problem of the Cantilever Beam with Elliptical Hole	81
6.2.4	Derivation of Stresses and Strains	86
6.3	Validation of Theoretical Results	86
6.3.1	Introduction	86
6.3.2	Example Problem 1 Description	86
6.3.3	Example Problem 2 Description	87

6.3.4	Description of the BEM Model	88
6.3.5	Influence of a Horizontal Crack on the Global Strain Field in a Cantilever Beam	89
6.4	Crack Detection by Fiber Optic Sensors	90
6.4.1	Interferometric Optic Sensors	91
6.4.2	Bragg Grating Sensors	91
6.4.3	Birefringent Optic Sensors	92
6.4.4	Integral Strain Field Mapping	93
6.4.5	Interpretations of the Integral Strain Field Maps	94
6.4.6	Effects of Finite Boundary Conditions	95
6.5	Case Studies	96
6.5.1	Case Study 1. Delamination Detection in $[0_m/\pm 45_n/90_k]_s$ Ad- vanced Composite Laminates.	97
6.5.2	Implications	104
6.5.3	Case Study 2. Delamination study in Reinforced Concrete Beams	104
7	Conclusion	130
A	BPM Example Problem	132

List of Figures

2-1	Geometric propagation of EM waves along a curved optic wave guide.	37
2-2	Physical model of a slab waveguide.	37
2-3	An array of lenses equivalent to the beam propagation expressed in Equation (2.32).	38
2-4	Refractive index profile and normalized input electric field for a mono-mode step index slab wave guide.	38
2-5	Electric field attenuation at discrete distances for a constant curvature wave guide. Radius of curvature is 8 mm.	39
2-6	Electric field attenuation for various constant radii of curvature. Propagation length = 5 mm	39
2-7	Rate of power attenuation for various constant radii of curvature. . .	40
2-8	Comparison of theoretical solution obtained by Marcuse and BPM results.	40
2-9	Rate of power attenuation through S - curve of various radii.	41
3-1	Physical model of oblique fiber bridging Mode I crack.	53
3-2	Equivalent physical model showing prescribed transverse and longitudinal displacements.	53
3-3	Finite element model of fiber bridging crack faces.	54
3-4	Detail of finite element mesh at the fiber matrix connection.	55
3-5	In-plane, σ_x and σ_y , stresses in a jacketed fiber at one fiber diameter from the crack face.	55
3-6	In-plane, σ_x and σ_y , stresses in a fiber without jacket.	56

3-7	Comparison of deflected shape between fiber center-line, outer radius and jacket matrix interface.	56
3-8	Fiber Deflected shape for the case of jacket free fiber.	57
3-9	In-plane, σ_x and σ_y , stresses in a jacketed fiber at two fiber diameters from the crack face.	57
3-10	Stress concentration at the debonded zone	58
3-11	Radius of curvature along fiber center-line.	58
3-12	Beam on elastic foundation model of an embedded fiber in an elastic matrix.	59
3-13	Beam on elastic foundation model for an oblique embedded fiber in an elastic matrix.	59
3-14	Comparison of Finite Difference and theoretical solution for beam on a linearly varying foundation stiffness, β	60
3-15	Comparison of Finite Element and Finite Difference results for the center-line deflection of the fiber with various assumed stiffnesses, β	60
4-1	Effect of Crack Opening Displacement and fiber orientation on electric power attenuation by the finite element method (FEM) and the finite difference method (FD)	69
4-2	Effect of Jacket Elastic Modulus on electric power attenuation.	69
4-3	Effect of Cut-off Frequency on electric power attenuation.	70
6-1	Physical elasticity model of weakened cantilever beam.	109
6-2	Comparison of derived theoretical solution with Savin's solution for the normalized tangential Stress $\frac{\sigma_{\theta J}}{Qh^2}$ on the hole edge.	109
6-3	Boundary Element Model of weakened cantilever beam.	110
6-4	Comparison of BEM and theoretical solutions (σ_x) at various distances from the elliptic hole.	111
6-5	Comparison of BEM and theoretical solutions (σ_y) at various distances from the elliptic hole.	112

6-6	Comparison of BEM and theoretical solutions (σ_{xy}) at various distances from the elliptic hole.	113
6-7	Rotation of Birefringent axes due to applied stress.	114
6-8	ϵ_x Sensitivity map at sensor position $f/h = 0.1$	115
6-9	ϵ_y Sensitivity map at sensor position $f/h = 0.1$	115
6-10	ϵ_{xy} Sensitivity map at sensor position $f/h = 0.1$	115
6-11	Effect of sensor position on theoretical sensor reliability.	116
6-12	Effect of finite beam depth on ϵ_x sensor reliability.	116
6-13	Effect of finite beam depth on ϵ_y sensor reliability.	117
6-14	Effect of finite beam depth on ϵ_{xy} sensor reliability.	117
6-15	Effect of crack length (2a) on sensor reliability. Normalizing parameter is the maximum shear sensitivity component.	118
6-16	Schematic layout of laminated cantilever beam.	119
6-17	Allowable applied load of $[0_m/\pm 45_n/90_k]_s$ laminate. $k = 100-m-2n$.	119
6-18	Engineering elastic modulus of $[0_m/\pm 45_n/90_k]_s$ laminate. $k = 100-m-2n$	120
6-19	Load to elastic modulus ratio for all n of $[0_m/\pm 45_n/90_k]_s$ laminate. $k = 100-m-2n$	120
6-20	Effect of crack length (a) on the strain difference ($\delta\epsilon_x$) for delaminated beam. Crack position at beam mid-point $c = 62.5$ mm and $d = 0$. Fiber position at $f = 0.8 h = 10$ mm.	121
6-21	Effect of crack length (a) on the strain difference ($\delta\epsilon_y$) for delaminated beam. Crack position at beam mid-point $c = 62.5$ mm and $d = 0$. Fiber position at $f = 0.8h = 10$ mm.	121
6-22	Influence line for normalized sensitivity ($\delta\epsilon_y$). Crack Length $a = 1$ mm. Crack Position $c = 62.5$ mm. Fiber position at $f = 22.5$ mm. Normalizing sensitivity given by Calero sensor of $5\mu\epsilon$ over 152 mm. .	122
6-23	Normalized stresses under point load acting on unweakened beam. Normalizing factor taken as the maximum stress.	123

6-24	Normalized stress difference between cracked and uncracked beam subjected to point load. Normalizing factor equal to maximum stress difference.	124
6-25	Influence lines for normalized sensitivity ($\delta\epsilon_y$) for various crack heights d/h . Beam height $h = 25$ mm. Crack Length $a = 1$ mm. Normalizing sensitivity given by Calero sensor of $5\mu\epsilon$ over 152 mm.	125
6-26	Influence lines for normalized sensitivity for various crack lengths a . Crack position $c = 62.5$ mm. Crack depth $d = 0$ mm. Normalizing sensitivity given by Calero sensor of $5\mu\epsilon$ over 152 mm.	125
6-27	Influence lines for normalized sensitivity ($\delta\epsilon_y$) for two cracks. Crack positions at $c_1 = 31.25mm$ and $c_2 = 93.75mm$. Crack depths at $d = 0mm$. Crack lengths $a = 1mm$. Normalizing sensitivity given by Calero sensor of $5\mu\epsilon$ over 152 mm.	126
6-28	Schematic representation of a moving load test for an aircraft component.	126
6-29	Reinforced concrete cross section.	127
6-30	Reinforced concrete beam and sensor layout.	127
6-31	Effect of crack length (a) on the strain difference ($\delta\epsilon_x$) for delaminated concrete beam. Crack position at $c = 2$ m and $d = 0.165$ m . Fiber position at $f = 0.8$ $h = 0.152$ m.	128
6-32	Effect of crack length (a) on the strain difference ($\delta\epsilon_y$) for delaminated concrete beam. Crack position at $c = 2$ m and $d = 0.165$ m . Fiber position at $f = 0.8$ $h = 0.152$ m.	128
6-33	Influence lines for normalized sensitivity ($\delta\epsilon_y$) for a simply supported beam. Crack position at $c = 2m$. Crack depths at $d = 0.165$ m. Fiber position at $f = 0.8$ $h = 0.152$ m. Normalizing sensitivity given by Calero sensor of $5\mu\epsilon$ over 152 mm.	129
A-1	Input fundamental mode for a straight slab waveguide.	137
A-2	Input and transformed waveguide index.	137
A-3	FFT components of the input electric field.	138

A-4 Output electric field after propagation of 3 mm in a 5 mm radius of curvature fiber.	138
--	-----

Notation - Electromagnetic analysis

a	Radius of optical fiber core.
c	Speed of light in vacuum.
B	Magnetic flux density vector.
D	Electric flux density vector.
E	Electric field intensity vector.
E_i	Electric field intensity vector component in i direction.
EM	Electromagnetic.
H	Magnetic field intensity vector.
J	Current density vector.
k_i	Wavenumber in medium i, $i = 0$ corresponds to vacuum.
NA	Numerical aperture.
n_i	Refractive index of medium i, $i = 0$ corresponds to vacuum.
P	Poynting vector.
r	Axial distance from core center.
TE	Transverse Electric Waves.
u	Eigenvalue of slab waveguide core.
v	Normalized (or cut-off) frequency.
w	Eigenvalue of slab waveguide cladding.
α	Power attenuation loss.
β	Propagation constant.
ϵ_i	Magnetic permittivity of material i, $i = 0$ corresponds to vacuum.
λ	Wavelength.
μ_o	Magnetic permeability of free space.
σ_i	Magnetic conductivity of material i, $i = 0$ corresponds to vacuum.
Φ	Time invariant electric field intensity vector.
ϕ	Direction invariant electric field intensity.
ω	Wave frequency.
$\nabla_{\mathbf{T}}$	Transverse Laplacian operator = $\frac{\partial^2}{\partial x^2} + \frac{\partial^2}{\partial y^2}$.

Notation - Mechanical analysis

- l_f Fiber free length.
- R Fiber radius.
- t Fiber jacket thickness.
- u Crack opening displacement.
- β equivalent foundation modulus.
- δ Fiber-tip displacement.
- θ Fiber-Crack incidence angle.

Notation - Delamination Analysis

a	Major ellipse half axis.
b	Minor ellipse half axis.
c	Crack position coordinate (x-direction).
d	Crack position coordinate (y-direction).
E	Young's modulus.
f	Fiber sensing position (y-coordinate).
FPF	First Ply Failure Load.
h	Half beam depth.
J	Second moment of area of the beam.
k	Number of 90° plies in $[0_m / \pm 45_n / 90_k]_s$ laminate.
l	Beam length.
m	Number of 0° plies in $[0_m / \pm 45_n / 90_k]_s$ laminate.
n	Number of $\pm 45^\circ$ plies in $[0_m / \pm 45_n / 90_k]_s$ laminate.
Q	Total applied tip force.
U	Airy stress function.
U_o	Airy stress function for uncracked member.
$\delta\epsilon$	Strain difference between cracked and uncracked member.
$\Delta\epsilon$	Absolute integral of weakened to unweakened strain difference.
ϵ_i	Strain component in the i-direction.
ψ	Complex analytical stress function.
χ	Complex analytical stress function.
ν	Poisson's ratio.
σ_i	stress component in the i-direction.

Chapter 1

Introduction

In the U.S alone, billions of dollars per year are spent on the inspection and repair of existing structural components. In concrete structures, the high cost of structural repair is due partly to the cost of manual inspection and the lack of reliable techniques for detection of damage at an early age. In advanced composites, the non-destructive evaluation techniques which are used for damage monitoring tend to be expensive and unreliable. Fiber optic sensors can potentially offer a solution to existing structural integrity monitoring problems due to their high sensitivity, low weight, immunity to electromagnetic interference such as lightning, continuous monitoring capabilities, their ability to detect distributed strains and their relatively cheap price. Another advantage of fiber optic sensors is the relative ease with which they can be embedded into curing materials such as reinforced concrete and advanced composites, which makes them ideal for integrity monitoring in civil and aerospace structures.

Previous work in structural damage sensor assessment has concentrated on experimental determination of sensor reliability under conditions in which the position and extent of damage is known. In practice, the location and extent of the damage is unknown and can greatly influence the ability of previously proposed sensing schemes to detect the damaged zone. This work focuses on theoretical and numerical electro-mechanical analysis to provide guidelines for the design and placement of fiber optic sensors. The factors effecting fiber optic system design are (a) crack length (or open-

ing), (b) relative position of the fiber sensor to the crack, (c) orientation of the fiber relative to the damaged zone, (d) mechanical properties of the fiber and structural material and (e) optical properties of the fiber.

The sensing of two typical failure modes in civil and aerospace structures are studied in this work. In particular, the feasibility of using fiber optic sensors to detect (a) tension cracks in concrete structures, (b) delamination damage in advanced composites and in reinforced concrete structures.

The first four chapters of this work deal with the evaluation of the combined electromagnetic and mechanical behaviour of micro-bend fiber optic sensors used for tension damage detection. The key parameters required for successful optic sensor design are identified and their effects on sensor performance are investigated. Chapter 2 explains the electromagnetic concepts required for the investigation of light wave propagation through optical waveguides and presents the Beam Propagation Method which allows the modelling of wave propagation through arbitrary sensor geometry. Chapter 3 focuses on presenting the mechanics of crack bridging fibers using three-dimensional finite element analysis and beam on elastic foundation models. Chapter 4 and 5 combines the electromagnetic and mechanical analysis to investigate the effects of various material and geometric parameters on crack sensor performance. Chapter 6 concludes the section on tension crack detection by explaining the parameters required for successful fiber optic sensor design.

Chapter 7 focuses on the feasibility of using fiber optic strain sensors for delamination detection by monitoring changes in strain caused by delamination, formation and growth. Effects of various parameters on crack detectability are investigated in this section. Two case studies are presented to show the applicability of fiber sensors in delamination detection for advanced aerospace composites and similar debonding damage in reinforced concrete structures.

The conclusion of the thesis outlines the research undertaken and presents the aims of future research.

Chapter 2

Electromagnetic Wave Propagation

2.1 Optical Wave guide Basics

2.1.1 Basic Electromagnetic Definitions

This section develops some of the basic electromagnetic concepts used further in this thesis.

An electromagnetic wave traveling in medium i , has speed, c_i given by :

$$c_i = \frac{\lambda_i \omega}{2\pi} \quad (2.1)$$

The frequency of propagation is related to the wave number k by :

$$k = \frac{\omega}{c_0} \quad (2.2)$$

The refractive index of a material is given by the ratio of light velocities :

$$n_i = \frac{c_0}{c_i} \quad (2.3)$$

where c_0 is the velocity of light in vacuum and is given by :

$$c_0^2 = \frac{1}{\mu_0 \epsilon_0} \quad (2.4)$$

The light velocity in a non-magnetic medium is given by :

$$c_i^2 = \frac{1}{\mu_0 \epsilon_i} \quad (2.5)$$

Using equations (2.3) to (2.6) it can be shown that :

$$\epsilon_0 = \frac{\epsilon_i}{n_i^2} \quad (2.6)$$

Substituting equations (2.3) and (2.5) into equation (2.2) and squaring gives :

$$k^2 = \frac{\omega^2 \mu_0 \epsilon_i}{n_i^2} \quad (2.7)$$

2.1.2 Wave Guide Definition

Any optical device which is able to guide electromagnetic energy in the optical frequencies along a well-defined path is known as an optical wave guide.

Essentially any medium consisting of a transparent dielectric material of low optical loss can serve as a transmission medium for guided optical waves if the refractive index of the material on the outside of the wave guide is less than the refractive index on the inside.

2.1.3 Wave Guide Characterization

Commercially available optical wave guides consist of a central core made of glass or plastic dielectric through which most of the electromagnetic energy is transmitted. The core is surrounded by a different dielectric material whose refractive index is slightly (less than 0.5%) lower than that of the core. The little electromagnetic field which is carried in the cladding decays rapidly to zero with distance from the core.

Figure (2-1) shows the geometric representation of a mono-mode EM wave propagating in a bent step refractive index optic wave guide. Note that electro-magnetic energy is lost through the cladding in the bend.

In Figure (2-1), the following symbols are used :

- n_1 Refractive index at fiber center.
- n_2 Refractive index of cladding.
- a Diameter of core.

2.2 Analysis of EM Transmission in a Slab Wave Guide

This section describes the analysis of a straight slab wave guide. Circular fiber transmission is not considered since as shown in section (2.6), circular fiber behaviour is computationally and mathematically more difficult to model than slab wave guide behaviour but can be approximately modelled by changing the material characteristic in the slab wave guide analysis. [6]

EM wave guide propagation theory has its roots in Maxwell's equations:

$$\nabla \times \mathbf{E} = -\frac{\partial \mathbf{B}}{\partial t} = -\mu_0 \frac{\partial \mathbf{H}}{\partial t} \quad (2.8)$$

$$\nabla \times \mathbf{H} = \frac{\partial \mathbf{D}}{\partial t} + \mathbf{J} = \epsilon_i \frac{\partial \mathbf{E}}{\partial t} + \sigma_i \mathbf{E} \quad (2.9)$$

The magnetic field vector, \mathbf{H} , can be eliminated from these two equations by taking the curl of equation (2.8), to give :

$$\nabla \times \nabla \times \mathbf{E} = \mu_0 \frac{\partial}{\partial t} (\nabla \times \mathbf{H}) \quad (2.10)$$

Expanding the left hand side of equation (2.10) with standard vector calculus techniques and substituting equation (2.9) into the right hand side leads to :

$$\nabla(\nabla \cdot \mathbf{E}) - \nabla^2 \mathbf{E} = -\mu_0 \epsilon_i \frac{\partial^2 \mathbf{E}}{\partial t^2} - \mu_0 \sigma_i \frac{\partial \mathbf{E}}{\partial t} \quad (2.11)$$

In the case of propagation through an homogeneous, isotropic medium with no free charge, $\nabla \cdot \mathbf{E} = 0$, the wave equation can be rewritten as :

$$\nabla^2 \mathbf{E} = \mu_0 \epsilon_i \frac{\partial^2 \mathbf{E}}{\partial t^2} + \mu_0 \sigma_i \frac{\partial \mathbf{E}}{\partial t} \quad (2.12)$$

Equation (2.12) is solved by assuming harmonic wave propagation in the z - direction. Hence every component of the electric and magnetic field is then given by :

$$\Phi = \mathbf{E}(x, y, z) e^{j\omega t} \quad (2.13)$$

Assuming that the medium is lossless gives $\sigma_i = 0$ and substituting equation (2.7) into equation (2.12) gives :

$$(\nabla^2 + k^2 n_i^2) \Phi = 0 \quad (2.14)$$

In the case of an electric field propagating along one direction, say the z direction, Maxwell's Equation reduces to the Helmholtz equation.

$$(\nabla^2 + k^2 n_i^2) \Phi_z = 0 \quad (2.15)$$

In general the Helmholtz Equation needs to be solved to find the the electric field distribution in 3 dimensions in an optical wave guide. The next section deals with solving the Helmholtz equation.

2.3 Solution of the Helmholtz Equation by the Beam Propagation Method

A general algebraic solution of the Helmholtz equation is not possible. Various numerical tools including, finite-difference [14], effective-index [7], Rayleigh-Ritz [15] and hybrid methods have been proposed. Lately the Beam Propagation Method (BPM) has had increasing success with more than 20 articles being written on the subject in 1994 alone. The BPM was first proposed by Fleck et al. (1976) [4] for the solution of high energy laser beam propagation but has since been extended to the solution of propagation of EM waves in any medium with small variations in refractive index.

The traditional BPM relies on two assumptions :

- (1) The field propagates along only one direction, the z axis with no backward traveling field.
- (2) The field can be considered paraxial, that is the optical rays essentially propagate along the central axis of the wave guide. This condition is realized when there are no abrupt changes in wave guide geometry, wave guide indices or wave guide curvature.

Under these conditions, the stationary electric field Φ is given by :

$$\Phi(x, y, z) = \phi(x, y, z)e^{-jkn_az}, \quad (2.16)$$

The Helmholtz equation (2.15) can be rewritten as a parabolic equation in ϕ :

$$\frac{\partial \phi}{\partial z} = -j \frac{\nabla_T + k^2(n_i^2 - n_a^2)}{2n_a k} \phi(x, y, z) \quad (2.17)$$

where $\nabla_T = \frac{\partial^2}{\partial x^2} + \frac{\partial^2}{\partial y^2}$ and the term $\frac{\partial^2 \phi}{\partial z^2}$ is ignored due to the Fresnel assumption of no rapid fluctuations in electric field. The Fresnel assumption is valid when there are no abrupt changes in fiber geometry.

Since no more power than the input power can be carried in the waveguide, the boundary condition is :

$\phi = 0$ as $r = \sqrt{x^2 + y^2} \rightarrow \infty$

2.3.1 Formulation of the Beam Propagation Method

Various solution techniques have been proposed to solve equation (2.17) including Fast - Fourier transform techniques (FFT) [3] and Rayleigh-Ritz methods.[16] Vassallo [14] proposed a finite difference technique which has the added advantages that it is potentially faster than the FFT method and can be extended to take into account the backward propagating field. This section summarizes both the FFT BPM and Vassallo's finite difference BPM.

2.3.2 The Vassallo Finite Difference Beam Propagation Method

In general the sensing of the backward propagating field is difficult since the electrical energy associated with this type of propagation is small and in practice extremely accurate equipment is needed for backward field detection. Vassallo has analysed the effect of ignoring the backward propagating field and has shown that for paraxial wave propagation, the effect of neglecting the backward propagating field is negligible and hence only the forward propagating field is considered here. Ignoring the backward propagating field means that equation (2.17) can be used directly. Using the standard Crank-Nicholson finite difference algorithm [10] in the z direction at any point $z_m = m\Delta z$, equation (2.17) can be rewritten as :

$$\frac{\phi^{m+1} - \phi^m}{\Delta z} = -j\mathbf{M}\phi^{m+\frac{1}{2}} \quad (2.18)$$

where :

$$\mathbf{M} = \frac{\nabla_T + k^2(n_i^2 - n_a^2)}{2n_a k} \quad (2.19)$$

Equation (2.19) can be evaluated by a standard central finite difference scheme, and $\phi^{m+\frac{1}{2}} = \frac{\phi^m + \phi^{m+1}}{2}$ indicates that the average value of the ϕ between successive dis-

cretization points. Simplifying equation (2.18) gives :

$$\left(\mathbf{M} + \frac{2}{j\Delta z}\right)\phi^{m+1} = \left(\frac{2}{j\Delta z} - \mathbf{M}\right)\phi^m \quad (2.20)$$

where ϕ^0 is the initial field input into the system.

The energy flow carried by the electromagnetic wave in any direction is calculated by the Poynting vector :

$$\mathbf{P} = \mathbf{E} \times \mathbf{H} \quad (2.21)$$

\mathbf{H} is the electromagnetic field vector which can be calculated using equations (2.10) and (2.14), giving :

$$\mathbf{H} = \frac{1}{j\omega\mu_0} \nabla \times \mathbf{E} \quad (2.22)$$

The power carried in the z-direction at position z^m is given by evaluating the time averaged Poynting vector in the z - direction over the cross sectional area of the waveguide:

$$P_z = \frac{1}{2} \int_A \phi(x, y, z^m) H(x, y, z^m) dA \quad (2.23)$$

The attenuation (or loss) of signal is given as :

$$\alpha = 10 \log_{10} \frac{P_{in}}{P_{out}} \quad (2.24)$$

where P_{in} is the input power and P_{out} is the measured power at the propagation distance of interest.

2.3.3 The FFT Beam Propagation Method

The FFT BPM is derived for the one-dimensional wave propagation equation in which case equation (2.17) becomes :

$$\frac{\partial \phi}{\partial z} = -j \frac{\frac{\partial^2}{\partial x^2} + k^2(n_i^2 - n_a^2)}{2n_a k} \phi(x, z) \quad (2.25)$$

Expressing $\phi(x, z)$ as a Fourier series having a finite number of terms gives :

$$\phi(x, z) = \sum_{n=-N/2+1}^{N/2} \phi_n(z) \exp(jk_{xn}x) \quad (2.26)$$

where k_{xn} denotes the discrete transverse wavenumbers defined by :

$$k_{xn} = \frac{2\pi}{L}n \quad (2.27)$$

where L is the width of the computational area.

The actual computation of equation (2.26) can be performed using the widely available Fast-Fourier transform (FFT) algorithm. Substituting (2.26) into (2.25) gives :

$$\frac{\partial \phi_n}{\partial z} = \frac{j}{2n_a k} (k_{xn}^2 + k^2(n_i^2 - n_a^2)) \phi_n \quad (2.28)$$

Solving equation (2.28) by assuming :

$$\phi_n(z) = \phi_{n1} e^{-j\beta z} \quad (2.29)$$

where β is the propagation constant and is assumed constant over a small distance in the z-direction (Δz).

Substituting (2.29) into (2.28) and solving for β gives :

$$\beta = -\frac{k_{xn}^2 - k^2(n_i^2 - n_a^2)}{2n_a k} \quad (2.30)$$

Substituting the expression for β into (2.28) and allowing for small step lengths (Δz) in the z-direction gives :

$$\phi_n(z + \Delta z) = \exp(j\Delta z \frac{k_{xn}^2 - k^2(n_i^2 - n_a^2)}{2n_a k}) \phi_n(z) \quad (2.31)$$

(2.31) is usually written in the form :

$$\phi_n(z + \Delta z) = \exp(j \frac{\Delta z}{2} \frac{k_{xn}^2}{2n_a k}) \times \exp(-j \Delta z \frac{k(n_i^2 - n_a^2)}{2n_a}) \times \exp(j \frac{\Delta z}{2} \frac{k_{xn}^2}{2n_a k}) \phi_n \quad (2.32)$$

Taking the inverse FFT of equation (2.32) recovers the solution ϕ of the Fresnel Equation (2.17).

Equation (2.32) can be interpreted as the propagation of the electric wave through a series of equivalent lenses as shown in Figure (2-3).

The first term on the right hand side of (2.32) represents the propagation of the wave through an homogeneous medium with an effective index of n_a and length $\Delta z/2$. The second term of equation (2.32) corresponds to a phase shift associated with propagation through a thin lens and the third term corresponds once again to propagation through an homogeneous medium of length $\Delta z/2$.

2.4 Solution of the Helmholtz equation for a Symmetric Slab Wave Guide

The objective of this section is to find the first fundamental mode of a straight slab wave as shown in figure (2-2). In the case of no change of electric field in the z-direction and y-direction and using equation (2.16), equation (2.15) can be simplified to :

$$\frac{\partial^2 \phi}{\partial x^2} + k^2(n_i^2 - n_a^2)\phi = 0 \quad (2.33)$$

To allow for guided modes in the core :

In medium 2 we have $n_a > n_2$ for $|x| > a$

In medium 1 we have $n_1 > n_a$ for $|x| < a$

Equation (2.33) is solved for the first symmetric mode (TE_0) in medium 1 by assuming

:

$$\phi_1 = A_1 \cos(k\sqrt{n_1^2 - n_a^2}x) + B_1 \sin(k\sqrt{n_1^2 - n_a^2}x) \quad (2.34)$$

For the symmetric mode $B_1 = 0$.

Equation (2.33) is solved for the first symmetric mode (TE_0) in medium 2 by assuming

:

$$\phi_2 = A_2 e^{-k\sqrt{n_a^2 - n_2^2}x} + B_2 e^{k\sqrt{n_a^2 - n_2^2}x} \quad (2.35)$$

The boundary condition $\phi = 0$ when $x = \infty$ gives $B_2 = 0$.

From equation (2.22), the magnetic field in the z-direction is given by :

$$H_z = \frac{1}{j\omega\mu_0} \frac{\partial\phi_y}{\partial z} \quad (2.36)$$

Hence the magnetic field in medium 1 is given by :

$$H_{z1} = \frac{k\sqrt{n_1^2 - n_a^2}}{j\omega\mu_0} A_1 \sin(k\sqrt{n_1^2 - n_a^2}x) \quad (2.37)$$

and in medium 2 by :

$$H_{z2} = \frac{k\sqrt{n_a^2 - n_2^2}}{j\omega\mu_0} A_2 e^{-k\sqrt{n_a^2 - n_2^2}x} \quad (2.38)$$

On the interface between the different media ϕ_y and H_z must be continuous. The continuity for ϕ_y gives :

$$A_2 = A_1 \frac{\cos(k\sqrt{n_1^2 - n_a^2}a)}{e^{-k\sqrt{n_a^2 - n_2^2}a}} \quad (2.39)$$

The continuity condition for H_z leads to :

$$\sqrt{n_1^2 - n_a^2} \tan(ka\sqrt{n_1^2 - n_a^2}) = \sqrt{n_a^2 - n_2^2} \quad (2.40)$$

Equation (2.40) can be rewritten as :

$$u \tan(u) = w \quad (2.41)$$

where :

$$u = k\sqrt{n_1^2 - n_a^2}a \quad (2.42)$$

$$w = k\sqrt{n_a^2 - n_2^2}a \quad (2.43)$$

and

$$v^2 = u^2 + w^2 \quad (2.44)$$

It can be shown [13] that for the propagation of a single eigenmode $v < \pi/2$ the fiber has mono-mode propagation.

Solving equation (2.40) for n_a gives the full solution to the electromagnetic wave equation.

2.5 Solution of the BPM for a curved slab wave guide

Hocker and Burns (1977) [6] showed that a circular fiber optic can be reduced to a slab wave guide by using the effective wave guide method. This method replaces a circular wave guide by a slab wave guide by changing the refractive index of the cladding material. The advantage of the effective index method is that it reduces the two-dimensional BPM problem to a one-dimensional problem and hence the number of computations can be reduced by approximately N operations (where N is the number of sample points taken in the one-dimensional case). Typical number of step per BPM analysis is 2500 steps (where the step length Δz is taken to be equal to $2 \mu m$ and the propagation length is 5 mm). Danielson (1984) [2] has reported computational time savings in the order of 100 when the effective index method is used.

Hocker and Burns (1977) [6] also compared the effective-index solution for a two dimensional square waveguide and found that the difference between the effective-index solution and a more rigorous three dimensional solution was a maximum of 10 percent for all values of the cut-off frequency (v). Ramaswamy (1974) [11] found

similar accuracies to Hocker and Burns (1977) [6] in experimental studies. A further geometric assumption in the effective index method presented here, is that the power loss in a circular fiber can be approximated by calculating the power loss in a slab waveguide. The validity of the geometric approximation can be deduced from the comparison of slab (without the effective index approximation) and circular step-index guides presented by Love and Winkler (1978) [8] who found that for small radii of curvatures (which dominate power loss in a generally curved waveguide), the slab waveguide give approximately the same results (to within 20 percent) of the circular waveguide. The results presented by Love and Winkler (1978) were also found by Snyder et al (1975) [12]. Preliminary calculations using the step-index method show that for small curvatures, the geometric approximation of the rectangular waveguide to the circular waveguide can give accurate solutions to within 10 percent.

In the case of a slab wave guide, the numerical finite difference evaluation of \mathbf{M} in the left hand side of equation (2.19) is :

$$\mathbf{M}\phi = \frac{\frac{\partial^2 \phi}{\partial x^2} + k^2(n_i^2 - n_a^2)}{2n_a k} \quad (2.45)$$

$$\mathbf{M}\phi = \frac{1}{2n_a k} \left[\frac{\phi_{p-1} + [k^2(n_i^2 - n_a^2) - 2]\phi_p + \phi_{p+1}}{\Delta x^2} \right] \quad (2.46)$$

where m indicates the x position of the finite difference grid, such that $x = m\Delta x$. In matrix form \mathbf{M} can be rewritten as :

$$\mathbf{M} = \frac{1}{2n_a k} \begin{pmatrix} -\frac{2}{\Delta x^2} + k^2(n_i^2 - n_a^2) & \frac{1}{\Delta x^2} & 0 & \dots & \dots \\ \frac{1}{\Delta x^2} & -\frac{2}{\Delta x^2} + k^2(n_i^2 - n_a^2) & \frac{1}{\Delta x^2} & 0 & \dots \\ 0 & \frac{1}{\Delta x^2} & \frac{2}{\Delta x^2} + k^2(n_i^2 - n_a^2) & \dots & \dots \\ \dots & 0 & \frac{1}{\Delta x^2} & \dots & \dots \\ \dots & \dots & \dots & \dots & \dots \\ \dots & \dots & \dots & \dots & 0 \end{pmatrix}$$

$$\begin{pmatrix}
\dots & \dots & & 0 \\
\dots & \dots & & 0 \\
\dots & \frac{1}{\Delta x^2} & & 0 \\
\dots & \dots & & 0 \\
\dots & \frac{1}{\Delta x^2} & -\frac{2}{\Delta x^2} + k^2(n_i^2 - n_a^2) &
\end{pmatrix} \quad (2.47)$$

The left hand side is seen to be tridiagonal and efficient sparse matrix methods can be used to solve the linear system of equations.

In order to satisfy the curvature paraxiality condition, the curved wave guide can be conformally mapped into an equivalent straight wave guide with refractive index : [5, 1]

$$n_i^{new} = n_i^{old} \left(1 + \frac{x}{R}\right) \quad (2.48)$$

The input electric field at $z = 0$ is taken to be the first fundamental mode developed in the previous section so that no attenuation occurs due to mode dispersion when propagation occurs through a straight fiber. The input electric field is normalized to unity by taking $A_1 = 1$ in equations (2.37) to (2.39).

The BPM analysis for various radii of curvature is performed on a standard mono-mode lossy fiber in order to check whether existing manufactured optic fibers can be used in future sensing applications. The optical characteristics of the fiber are :

- Core diameter : $6\mu m$.
- Core refractive index : 1.4613.
- Cladding refractive index : 1.458.
- Light wavelength : $1.3\mu m$.
- Propagation step : $\Delta z = 2\mu m$.
- Propagation distance : 5 mm.

- Grid spacing : $\Delta x = 0.5\mu m$.
- Grid length : $128\mu m$.

The refractive index profile and input electric field is given in Figure (2-4).

In order to check the numerical accuracy the of the BPM, fundamental mode propagation and power attenuation through a straight fiber is studied. Attenuation losses of -0.009 dB is caused by numerical inaccuracies as a consequence of the finite difference discretization in the x and z directions.

The effect of electromagnetic field propagation along a curve of constant radius is shown in Figure (2-5). The downward movement in peak value of the propagated wave and the carrying of energy in the outer radius cladding shows the typical curvature attenuation of the electric field by energy loss through the cladding. Appendix A shows an example calculation of the BPM algorithm for a constant radius curve.

Figure (2-6) shows the power attenuation through curves of various radii. Radii of less than 8 mm show significant power loss while radii greater than 12 mm show insignificant loss. Total power loss is dependent both on radius of curvature and distance of propagation along the curve.

Figure (2-7) shows the rate of power loss with distance occurring in the fibers for various radii of curvature. The large power loss occurring at the beginning of the curve is due to transition losses. During the transition portion of the propagation, the input straight slab fundamental mode changes to the curved waveguide fundamental mode as shown in Figure (2-5). Transition loss occurs due to the dispersion of energy within the transition length as the input fundamental mode changes to the curved fundamental mode.

The constant rate of power loss after initial transition loss is the steady state power

loss. Marcuse (1971) [9] obtained an approximate closed form solution for the steady state bend loss of constant curvature wave guides given by :

$$\alpha = 4.34 \frac{wu^2 e^{-\frac{2w^3 R}{\sqrt{n_2^2 k^2 - u^2}} + wa}}{v^2 \sqrt{n_2^2 k^2 - u^2} \left(\frac{a}{2} + \frac{1}{w}\right)} \text{ in dB/unit length} \quad (2.49)$$

The comparison of the theoretical solution and numerical solution is shown in Figure (2-8).

The relative contribution to total power loss of the steady state propagation and transition loss in an arbitrarily curved wave guide is dependent on :

- Propagation distance - steady state propagation loss dominant.
- Radius of curvature - both losses dominant.
- Changes in curvature - transition loss dominant.

For small distance propagation along a curvature changing fiber, the transition loss is dominant. This effect can be studied by calculating the curvature loss in a constant radius "S" curve. An "S" curve has the characteristics of having two transition losses. The rate of attenuation with distance in a "S" curve is shown in Figure (2-9). The large transition losses occur near propagation distances of 0 and 5 mm corresponding to the position of abrupt curvature change.

The abrupt decrease in attenuation loss at propagation distances of 5 mm (just before the large transition losses) shown in Figure (2-9) corresponds to break down in the BPM paraxial assumption. The abrupt change in curvature at this distance requires the propagating fundamental electric field to change abruptly which violates the paraxial assumption. Since the constant bend radius loss is re-established after approximately 8 mm, it can be noted that after the break down in paraxial assumptions which occur over a short distance (between approximately 5 and 5.5 mm) the field eventually behaves consistently with the paraxial assumptions. It must be noted that the BPM results give no indication whether the transition losses after the abrupt

curvature change are accurately calculated. It can be concluded that the break down in paraxial assumptions lead to small inaccuracies with respect to total power losses provided that the BPM assumptions are not violated frequently and thus make up only a small percentage of the total power loss.

2.6 Wave Guides used for Sensing

It is suggested here that fiber optic sensors relying on detection of host material damage by curvature change, should be step-indexed mono-mode cylindrical fibers. This type of fiber has the advantage of being more sensitive to curvature loss than other fibers since slight deviations from straight transmission causes electromagnetic loss into the cladding and the fiber. In sensing applications where the inclusion of the sensing element causes strength loss in the host material (such as in strain sensing of composites), the mono-mode fiber has the added advantages of having a smaller diameter.

The success of the fiber optic sensor is dependent both on the sensitivity of the sensing and detection device. Though the production cost of fibers are essentially independent of sensitivity, the cost of detection equipment is strongly dependent on sensitivity. Expensive detection equipment is capable of detecting losses in the 0.01 dB range while relatively inexpensive detection equipment operates in the 5 dB sensing range. Hence, it is advisable to design the fiber with optimal sensitivity so as to reduce the detection equipment cost and at the same time avoid excessive power loss at each crack (otherwise only a small number of cracks can be detected with each fiber).

For desirable fiber sensor design, a theoretical model relating crack opening to the optimal power loss needs to be developed. This is the focus of the next 3 chapters of the present thesis.

Bibliography

- [1] R. Baets and P.E. Lagasse. *Loss calculations and design of arbitrary curved integrated-optic waveguides*. J. Opt. Soc. Am. **73**. 177-182 (1983)
- [2] P. Danielson. *Two-dimensional propagating beam analysis of an electrooptic waveguide modulator*. IEEE J. Quantum Electron. **20**. 1093-1097 (1984)
- [3] M. D. Feit and J. A. Fleck. *Computation of mode properties in optical fiber waveguides by a propagating beam method*. Appl. Opt. **19**. 1154-1164 (1980)
- [4] J. A. Fleck, J. R. Morris and M. D. Feit. *Time dependent propagation of high energy laser beams through the the atmosphere*. Appl. Phys. **10** 129-160 (1976).
- [5] M. Heiblum and J. Harris. *Analysis of curved optic waveguides by conformal transformation*. IEEE J. Quantum Electron. **11**. 75-83 (1975)
- [6] G. B. Hocker and W.K. Burns. *Mode dispersion in diffused channel waveguides by the effective index method*. Appl. Opt. **16**. 113-118 (1977)
- [7] R.M. Knox and P.P. Toullos. *Integrated circuits for the millimeter through optical frequency range*. Proceedings of M.R.I. Symposium on Submillimeter Waves. J.Fox ed. (Polytechnic, Brooklyn). 99-107 (1970)
- [8] J.D. Love and C. Winkler. *Power attenuation in bent multimode step-index slab and fibre waveguides*. Electron. Lett. **14**. 32-34. (1978)
- [9] D. Marcuse. *Bending Loss of the assymetric slab waveguide*. Bell Sys. Tech. J. **50**. 2551-2563 (1971)

- [10] W.H. Press et al. *Numerical recipes in FORTRAN: the art of scientific computing*. (Cambridge University Press, Cambridge). (1992)
- [11] V. Ramaswamy. *Strip Loaded Film Waveguide*. Bell Sys. Tech. J. **53**. 697-704 (1974)
- [12] A.W. Snyder, I. White and D.J. Mitchell. *Radiation from bent optical waveguides*. Electron. Lett. **11**. 332-333. (1975)
- [13] W. van Etten. *Fundamentals of Optical Fiber Communication*. (Prentice Hall, New York). (1991)
- [14] C. Vassallo. *Reformulation of the beam-propagation method*. J. Opt. Soc. Am. A **10**. 2208-2216 (1993)
- [15] R.G. Walker. *The design of ring resonators for integrated optics using silver ion-exchange waveguide*. Ph.D. dissertation (Glasgow University, Glasgow). (1981)
- [16] D. Yevick and B. Hermansson. *New formulation of the matrix beam propagation method: application to rib waveguide*. IEEE J. Quantum Electron. **25**. 221 (1989)

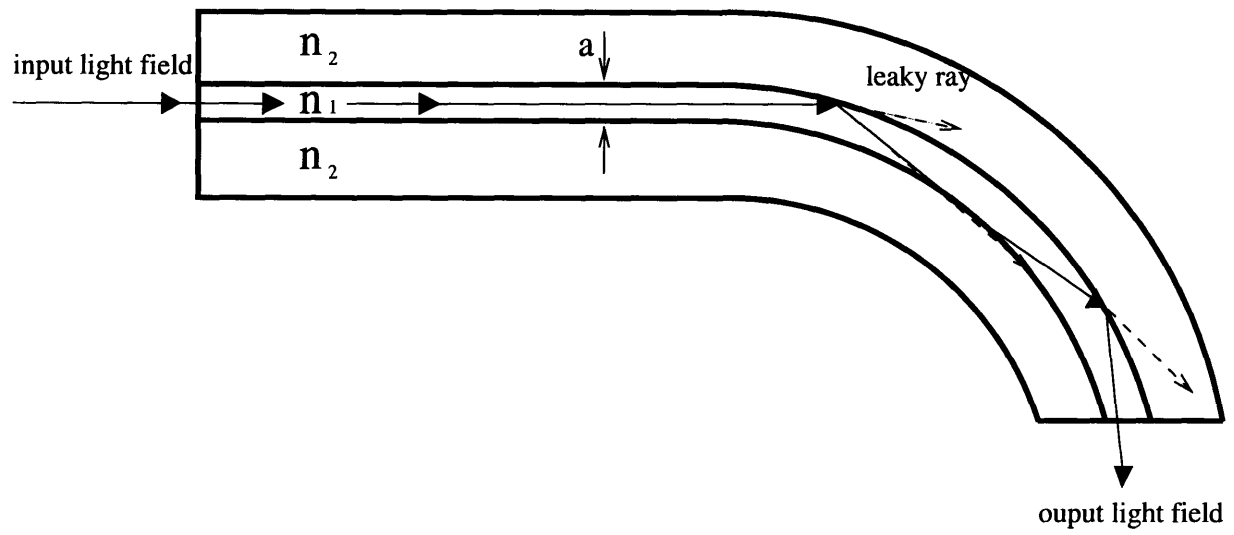


Figure 2-1: Geometric propagation of EM waves along a curved optic wave guide.

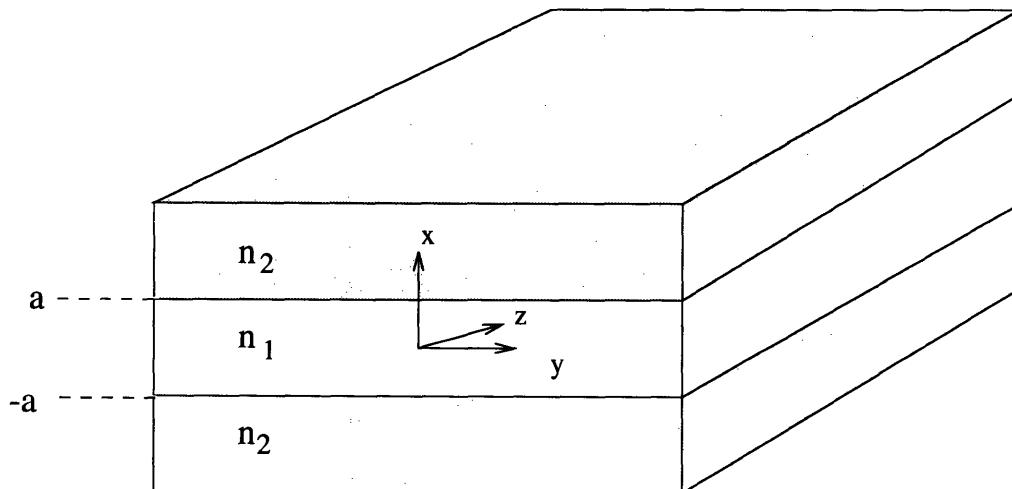


Figure 2-2: Physical model of a slab waveguide.

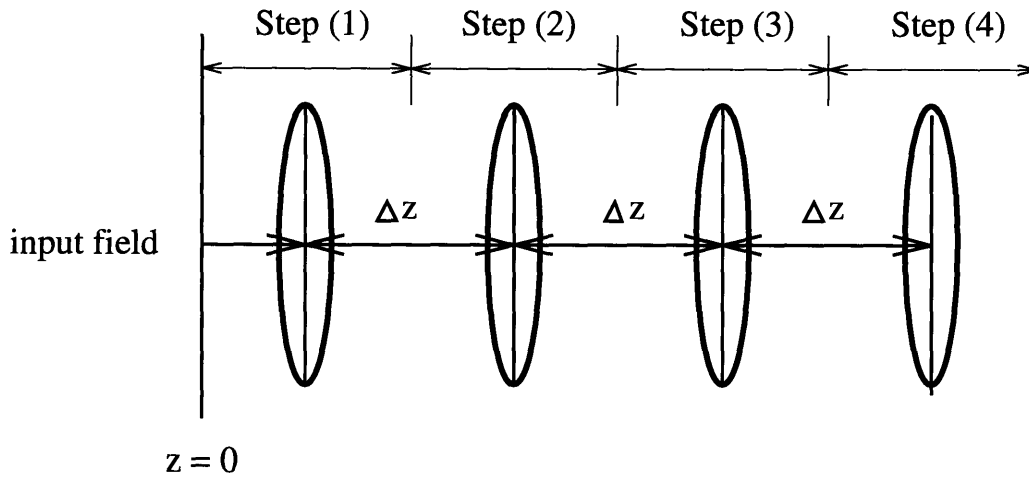


Figure 2-3: An array of lenses equivalent to the beam propagation expressed in Equation (2.32).

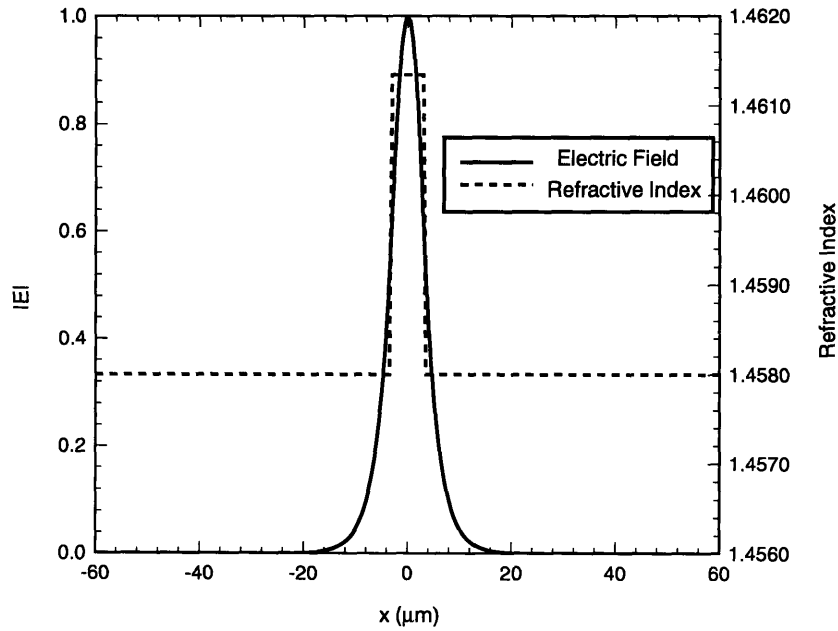


Figure 2-4: Refractive index profile and normalized input electric field for a mono-mode step index slab waveguide.

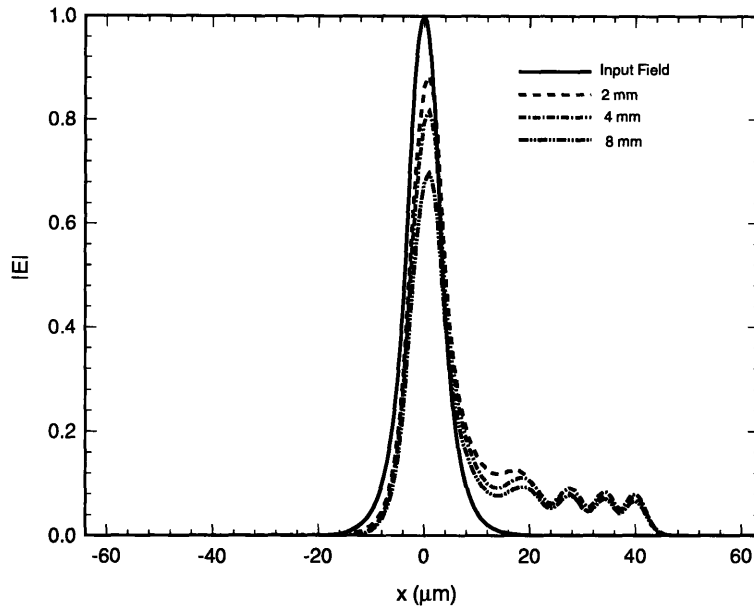


Figure 2-5: Electric field attenuation at discrete distances for a constant curvature wave guide. Radius of curvature is 8 mm.

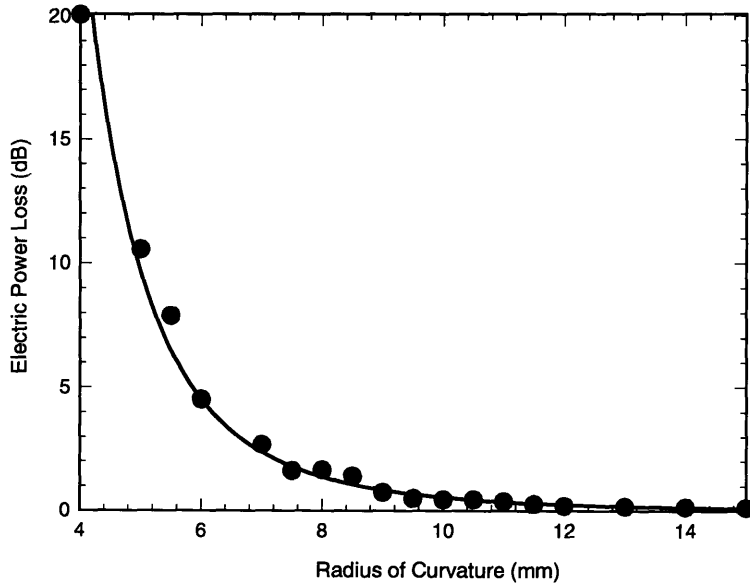


Figure 2-6: Electric field attenuation for various constant radii of curvature. Propagation length = 5 mm

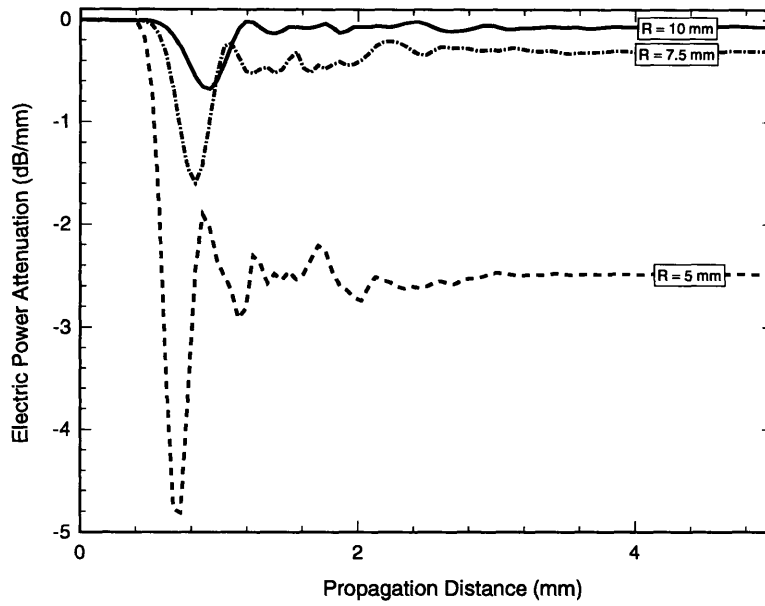


Figure 2-7: Rate of power attenuation for various constant radii of curvature.

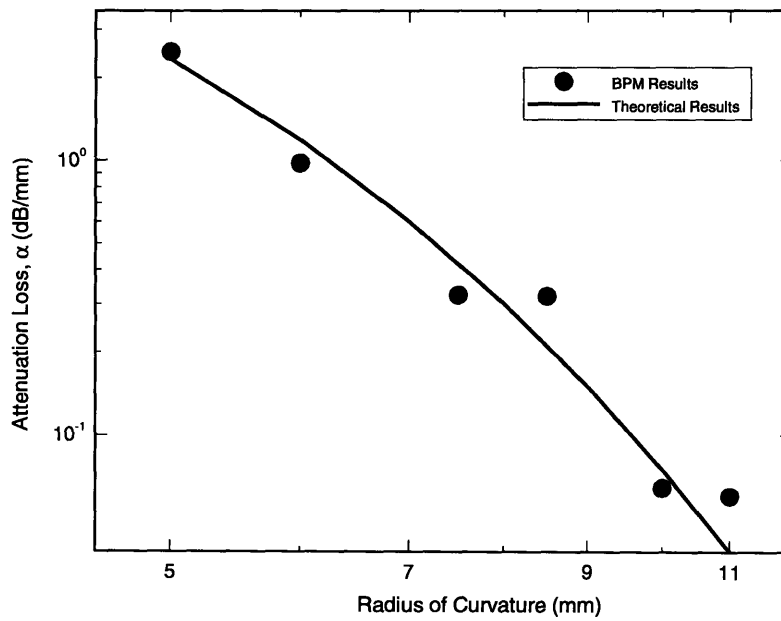


Figure 2-8: Comparison of theoretical solution obtained by Marcuse and BPM results.

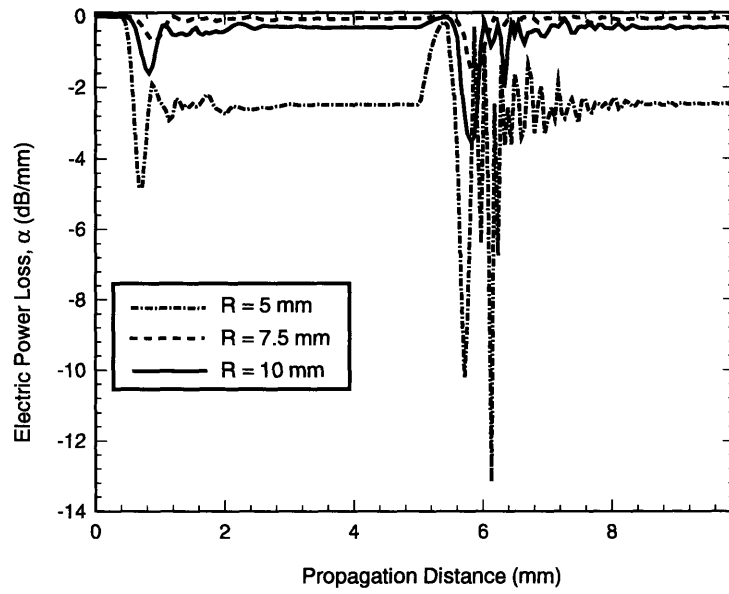


Figure 2-9: Rate of power attenuation through S - curve of various radii.

Chapter 3

Mechanical Behaviour of an Optic Fiber Under Bending

3.1 Introduction

Chapter 2 has shown that electric field attenuation in an optic waveguide is strongly dependent on the axial curvature distribution of the fiber. This section deals with the numerical modelling of the mechanical behaviour of an optic fiber sensor in a matrix material.

The mechanical behaviour of reinforcing fibers in cracked matrix material have been investigated by several authors. The mechanical model proposed by Leung [1] analyzed the behaviour of a steel fiber embedded in an elastic matrix by assuming that the continuum interaction of a fiber bearing on the matrix could be modelled as a beam on an elastic foundation. Stang and Shah [3] proposed a theoretical model of a fiber subjected to pullout with debonding. Previous models have the problems of either assuming the fiber to act in plane strain or subject to pure Mode I crack opening. The model proposed in this section is an extension of Leung [1] beam on elastic foundation model with the equivalent matrix stiffness being calculated by a three dimensional finite element analysis. The effect on the equivalent foundation stiffness of a soft bedding layer such as a fiber jacket is also included in this section.

3.2 Physical Model of Fiber Matrix Interaction

A crack occurring in a material can propagate under three modes (labelled I, II and III). The analysis presented herein only considers the in-plane propagation modes (I and II) caused by tension and shear action in one plane. General out of plane crack propagation is ignored in the analysis since electromagnetic tools for analysing generally curved three dimensional waveguides have not yet been developed and it is unlikely that the paraxial assumption of mode propagation used in the BPM is valid.

Only analysing in-plane crack propagation means that the assumed physical model is as shown in Figure (3-1). Figure (2.1) shows a generally oriented fiber in the crack plane, bridging an opening crack. Due to the orientation of the fiber to the crack face, far field applied tension will cause coupled shear, bending and extension in the fiber. This work focuses on Mode I (tension) crack propagation, though the work can readily be extended to Mode II (shear) crack action by varying the prescribed displacements on the fiber.

Morton and Groves [2] have shown that for a fiber crossing the crack faces, the physical model shown in Figure (3-1) above can be reduced to the one shown in Figure (3-2). The assumption in Figure (3-2) is that the fiber is located at such a distance from the crack tip that the rigid body crack face movements can be considered parallel. This assumption allows for the modelling of half the fiber and corresponding matrix due to symmetry.

Figure (3-2) shows the geometric changes in the fiber undergoing a crack opening, u has two components given by :

$$\delta = u \sin \theta \quad (3.1)$$

$$l_f = (R + t) \tan \theta + u \cos \theta \quad (3.2)$$

The dimensions of a standard mono-mode optic fiber typically used for fiber optic sensing are :

- Fiber radius : $R = 62.5 \mu m$.
- Fiber jacket thickness : $t = 37.5 \mu m$

3.3 The Finite Element Model

The physical model given in Section (3.2) above can be further simplified by assuming a fixed far boundary at a distance of 5 fiber diameters from the fiber center which by Saint Venant's principle should allow for complete stress homogenization meaning that there is no variation in stresses along the far boundary. Figure (3-3) shows the mathematical model derived from the physical model with the far boundary assumption. The materials in the model are assumed isotropic and linearly elastic with material constants :

- Glass fiber : Young's Modulus 70 GPa. Poisson Ratio 0.2.
- Plastic jacket : Young's Modulus 3 GPa. Poisson Ratio 0.2.
- Cement Matrix : Young's Modulus 20 GPa. Poisson Ratio 0.2.

The assumptions behind the Finite Element Scheme are :

- Separation between fiber and matrix on the tension zone is allowed for by leaving a thin zone free of elements at the fiber-matrix interface. The length of the separated zone is taken to be one fiber diameter which approximately corresponds to the length of the tensile zone. It must be noted that the effect of various assumed material properties in the separated zone (E varying from zero for complete fiber-matrix separation to E equal to matrix stiffness for no separation) only effects the center line deflection by approximately 5% which is considered to be adequately accurate for this analysis.

- Loading corresponding to the prescribed deflections are governed by Mode I and Mode II crack movements.

Eight node linear brick elements with various meshing schemes were used to compare mesh sensitivity. The mesh shown in Figure (3-4) was chosen since it was found to optimize both accuracy and computational time. The final finite element model has the following characteristics.

- Number of elements 2460.
- Number of nodes 2736.
- Radial far boundary at 5 fiber diameters.
- Axial far boundary at 12 fiber diameters.

3.4 Finite Element Results

The effects of varying fiber-matrix incidence angle and crack opening displacement is presented elsewhere. The results of simulations on a fiber with incidence angle of 30° with crack opening of $0.2\mu m$ is presented in this section in order to clarify some key features in the finite element model for a typical fiber orientation and crack opening displacement.

The band plots presented in Figures (3-5 a) and (3-5 b) show the in-plane stress distributions at a distance of one fiber diameter from the crack face for a fiber with a soft jacket coating. Figures (3-6 a) and 3-6(b) show the in-plane stress plots for a fiber with no jacketing material. Comparing Figures (3-5) and (3-6) shows that for the jacketed fiber, the jacket material carries most of the stresses and only relatively small stresses are transferred to the matrix. The stresses at the far boundary are found to be homogeneous thus validating the far boundary assumption.

Figure (3-7) shows that the difference in deflected shape between the glass fiber center

line, the fiber outer radius and jacket-matrix boundary. The relatively small difference in deflected shape between the fiber center line and fiber outer radius implies that the fiber center-line remains almost parallel to the outer radius. The relatively large difference in deflection between the fiber center line and jacket interface implies that most of the deflection occurs within the jacket and hence most stress transferal occurs within the jacket region. The difference in deflected shapes of the fiber and jacket can be seen by comparing the deflections at the crack face and along the line marked A. The matrix-jacket interface has essentially zero deflection past the crack face while the glass fiber has deflections past line A. The fiber enters the matrix at the crack face, thus the deflections of the jacket to the left of the crack face are due to the free applied fiber deflections, while deflection to the right of the crack face include the effect to matrix jacket interaction. Figure (3-8) shows the deflected shape of the fiber with no jacketing material. Notice that there are substantial deflections in the matrix past the crack faces. Hence it can be concluded that the presence of a jacket help to reduce the deflections (and the stresses) in the matrix.

Figures (3-5) and (3-7) show that most stress transferal occurs within the jacket. Figures (3-9) show the in-plane stress distribution at two fiber diameters from the crack face in a jacketed fiber. Comparing Figures (3-9) and (3-5) it can be seen that the stresses in the matrix at a distance of two fiber diameters is substantially less than the stresses at one fiber diameter. Spalling of the matrix is associated with micro-cracks and defects occurring within the material. Due to the rapid decay of stresses in the matrix and the associated small stresses transferal from fiber to matrix, it is unlikely that the matrix will spall or crush and the linear elastic assumption for the matrix behaviour is valid.

The apparently anomalous phenomena of tensile stresses (σ_{yy}) above the debonded zone in Figure (3-9) are due to the large tensile stresses associated with the end of the debonded zone. Figure (3-10) shows the relatively large (σ_{yy}) stresses at the end of the debonded zone. Similarly zones of stress concentrations occur in the x-y plane where the debonded zone ends as shown in Figures (3-5). By filling the debonded

gap with low stiffness material it was found that the magnitude of the stress concentrations could be reduced, and the effect of the material had no significant effect on changing the deflected shape of the fiber center-line.

Figure (3-11) shows the small radius of curvature in the fiber associated with the 0.2 mm crack opening.

3.5 Beam on Elastic Foundation Analysis of Fiber Behaviour

Leung [1] showed that the action of an embedded fiber in a matrix material subjected to bending deflection can be modelled as a beam on an elastic foundation provided that the shear stiffness of the matrix material is much smaller than the in-plane stiffness of the fiber.

The equivalent stiffness of the three dimensional behaviour is studied in the following way.

Consider an elastic beam on a soft founding material as shown in Figure (3-12).

The response of this beam can be analyzed by solving the following differential equations :

For Beam 1 :

$$\frac{d^4 y_1}{dz_1^4} = 0 \quad (3.3)$$

For Beam 2:

$$\frac{d^4 y_2}{dz_2^4} = 4\beta^4 y_2 \quad (3.4)$$

where :

y is the deflection at any point.

z is the distance along the beam.

β is the relative stiffness term = k/EI .

k is the stiffness of the foundation.

E is the Modulus of Elasticity of the beam.

I is the Moment of Inertia.

The boundary conditions are :

$$y_1 = u \quad \text{at} \quad z_1 = 0. \quad (3.5)$$

$$y_1'' = 0 \quad \text{at} \quad z_1 = 0 \quad (\text{Zero Moment Condition}). \quad (3.6)$$

The kinematic and static equivalence at the beam-matrix connection gives :

$$y_1 = y_2 \quad \text{at} \quad z_1 = l \quad (3.7)$$

$$vy_1' = y_2' \quad \text{at} \quad z_1 = l \quad (3.8)$$

$$y_1'' = y_2'' \quad \text{at} \quad z_1 = l \quad (3.9)$$

$$y_1''' = y_2''' \quad \text{at} \quad z_1 = l \quad (3.10)$$

The zero deflection and slope conditions at the far boundary gives :

$$y_2 = 0 \quad \text{at} \quad z_2 = \infty \quad (3.11)$$

$$y_2' = 0 \quad \text{at} \quad z_2 = \infty \quad (3.12)$$

Here a prime denotes a differentiation with respect to axial distance z .

The solution of this differential equation is :

For $z_1 < l$:

$$y_1 = u_1 \left(\frac{z^3 \beta^3 - 3z\beta(l^2 \beta^2 + 2l\beta + 1)}{2l^3 \beta^3 + 6l^2 \beta^2 + 6l\beta + 3} + 1 \right) \quad (3.13)$$

For $z_2 > 0$

$$y_2 = u_1 \frac{3e^{(-\beta z_2)} [(l\beta + 1)\cos(\beta z_1) - l\beta \sin(\beta z_1)]}{2l^3 \beta^3 + 6l^2 \beta^2 + 6l\beta + 3} \quad (3.14)$$

The schematic representation in Figure (3-13) shows that in general the stiffness of the equivalent foundation can be taken as a monotonically increasing function with length of fiber embedded in the matrix. This is due to the fact that at the crack face, the bearing matrix area is negligible.

The generalized differential equation for a straight fiber with arbitrary founding stiffness properties can be expressed by :

$$\frac{d^4 y}{dz^4} = -\beta^4(z)y \quad (3.15)$$

It must be noted that equation (3.15) is still linear even though the relative stiffness term β is any function of z .

In this case the variation in stiffness is assumed linear and the governing equation becomes :

$$\frac{d^4 y}{dz^4} = -\beta^4 z y \quad (3.16)$$

The boundary conditions are the same as in equations (3.5) to (3.12).

The standard method of solution of this type of non-homogeneous differential equation is by substituting $y = \sum a_i z_i$. The substitution gives the following solution :

$$y = \sum_{i=1}^4 a_i \sum_{k=0}^{\infty} \frac{(-1)^k (4\beta)^{4k} z^{(5k+i-1)}}{(5k+i-1)!} \prod_{j=0}^{k-1} (5j+i) \quad (3.17)$$

Here the a_i 's are constants determined by the boundary conditions.

Since the product in equation (3.17) is generally difficult to evaluate, a finite differ-

ence scheme is used to estimate the differential equation (3.16) and is compared to the analytical solution in equation (3.17).

The finite difference scheme used is the Central Difference Method which gives the following scheme :

$$\frac{y_{n-2} - 4y_{n-1} + 6y_n - 4y_{n+1} + y_{n+2}}{\Delta z^4} = -\beta v^4 z_n y_n \quad (3.18)$$

Equation (3.18) leads to a tridiagonal symmetric stiffness matrix, which can be efficiently solved by sparse matrix reduction.

Figure (3-14) shows that there is essentially no difference between the finite difference and theoretical solutions for the linearly increasing foundation stiffness.

3.6 Calculation of Equivalent Foundation Stiffness

This section deals with the calculation of the foundation stiffness provided by the jacket and matrix. Considering the jacket and matrix as two equivalent springs in series, a single parameter for relative stiffness β can be used to describe the action of the fiber. β is chosen in such a way so that it best approximates (in a least squares sense) the fiber response calculated by the finite element method.

In general for a specific glass fiber the relative stiffness parameter β will depend on the following model properties :

- Matrix elastic modulus.
- Jacket elastic modulus.
- Fiber orientation.

- The jacket thickness to fiber radius ratio which governs the relative stiffness of the jacket.

For a specific set of model parameters, the finite difference scheme given by equation (3.18) is solved for a range of β values until the best-fit beta is found. This relative stiffness term is then taken to be the equivalent stiffness of the jacket and matrix. Figure (3-15) shows the comparison of the fiber center-line deflections for the fiber in Section (3.2) obtained by the finite element and finite difference results. Figure (3-15) also shows the effect of various β stiffnesses on the obtained deflected shape. For this case $\beta = 7.72$ per meter gives the best fit stiffness.

Bibliography

- [1] C. K. Y Leung and V. C Li. *Effect of Fiber Inclination on Crack Bridging Stress in Brittle Fiber Reinforced Brittle Matrix Composites*. J. Mech. Phys. Solids. **40**. 1333-1362. (1992)

- [2] J. Morton and G. W. Groves. *The cracking of composites consisting of discontinuous ductile fiber in a brittle matrix - effect of fiber orientation*. J. Mat. Sci. **9**. 1436-1445. (1975)

- [3] H. Stang and S. P. Shah. *Failure of fiber reinforced composites by pull out fracture*. J. Mat. Sci. **21**. 953-958. (1986)

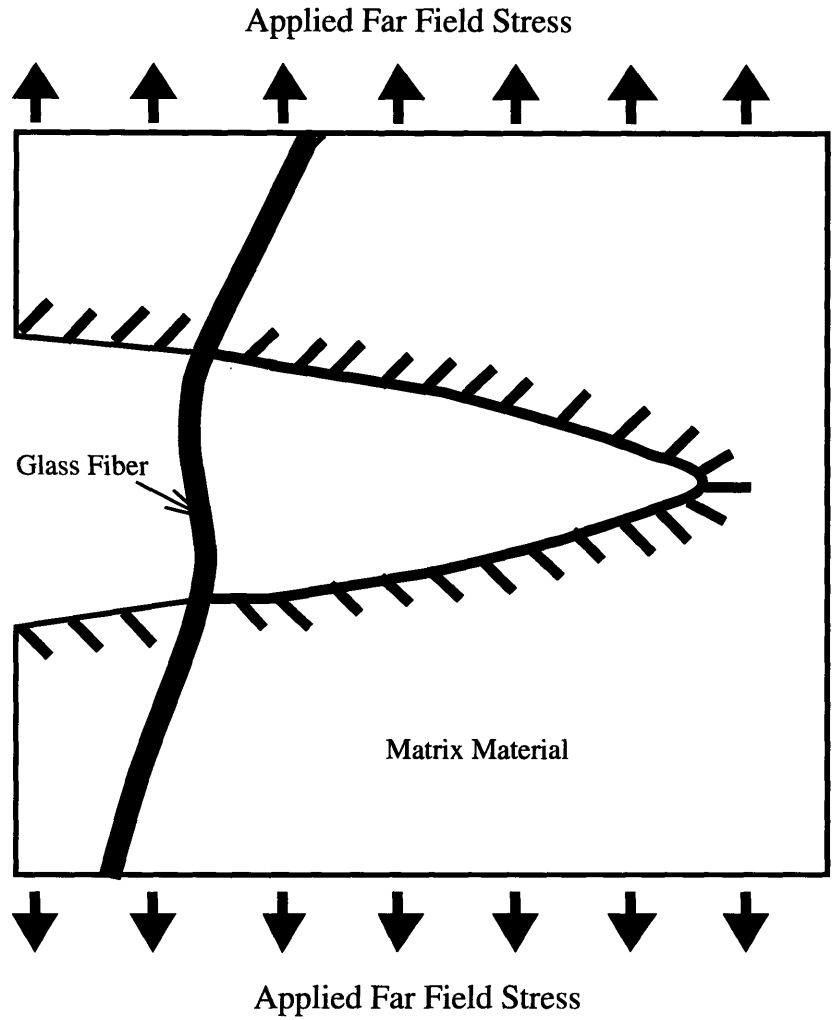


Figure 3-1: Physical model of oblique fiber bridging Mode I crack.

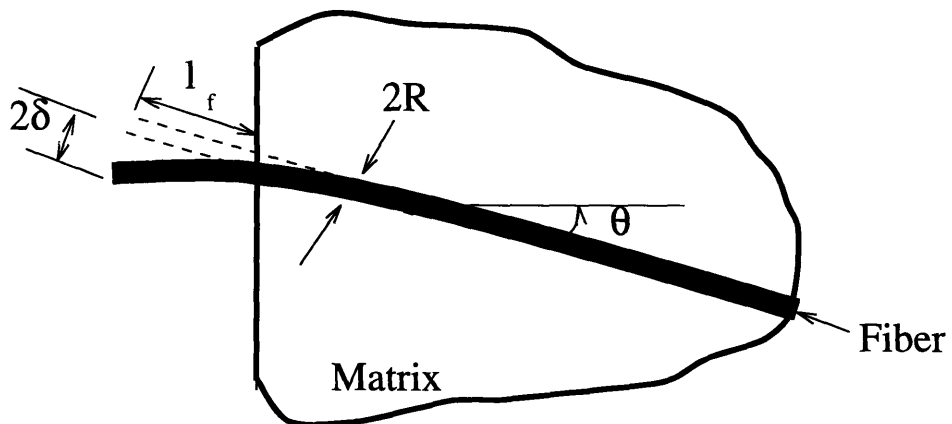


Figure 3-2: Equivalent physical model showing prescribed transverse and longitudinal displacements.

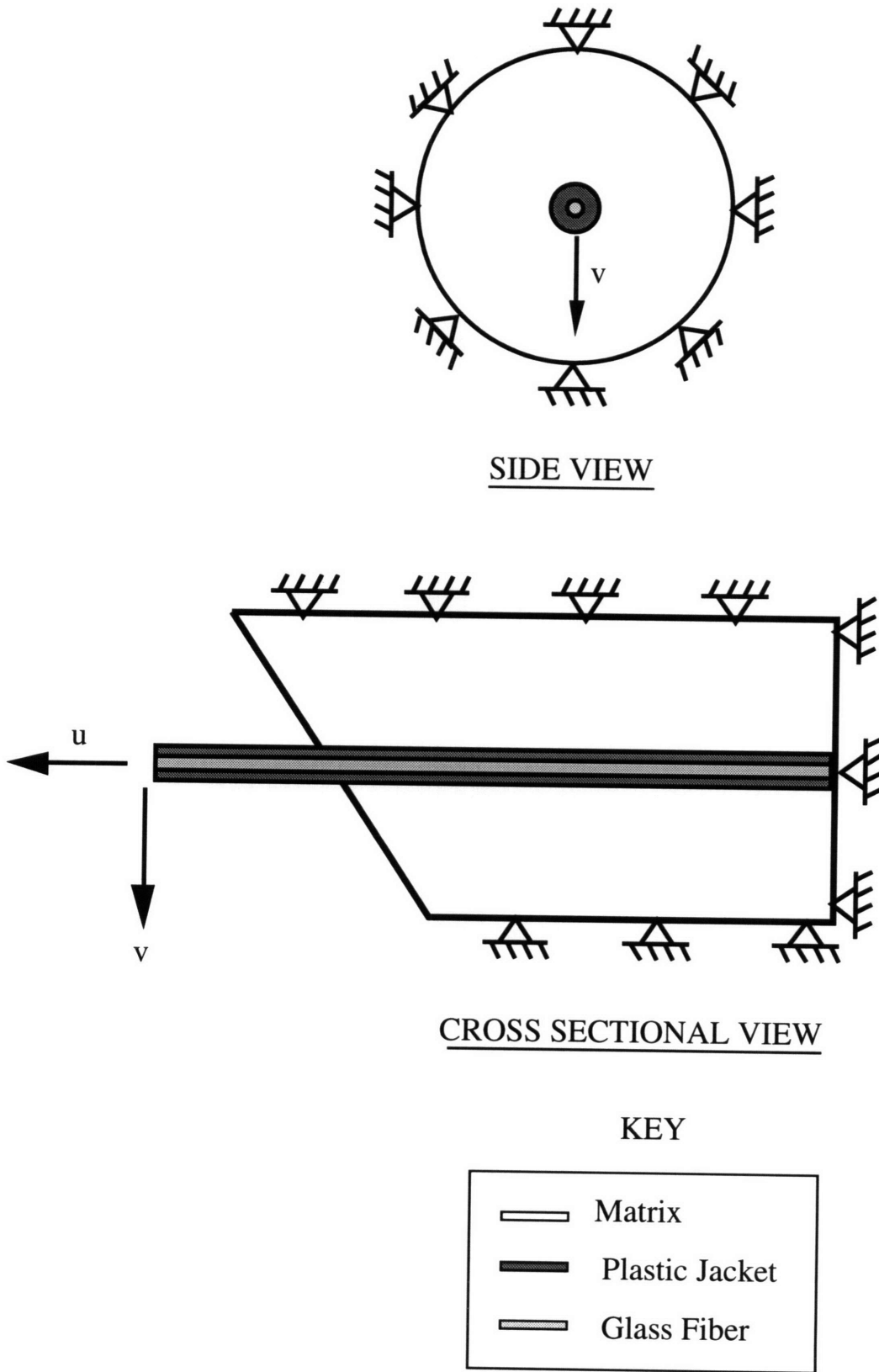


Figure 3-3: Finite element model of fiber bridging crack faces.

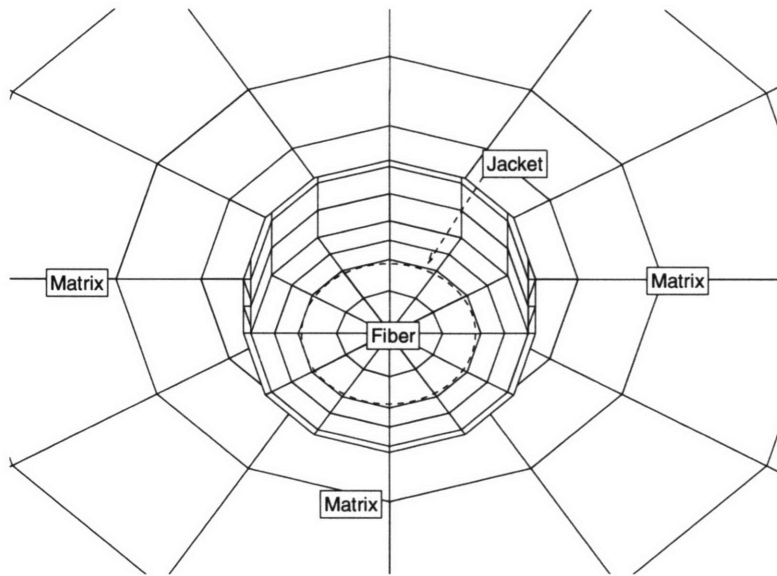


Figure 3-4: Detail of finite element mesh at the fiber matrix connection.

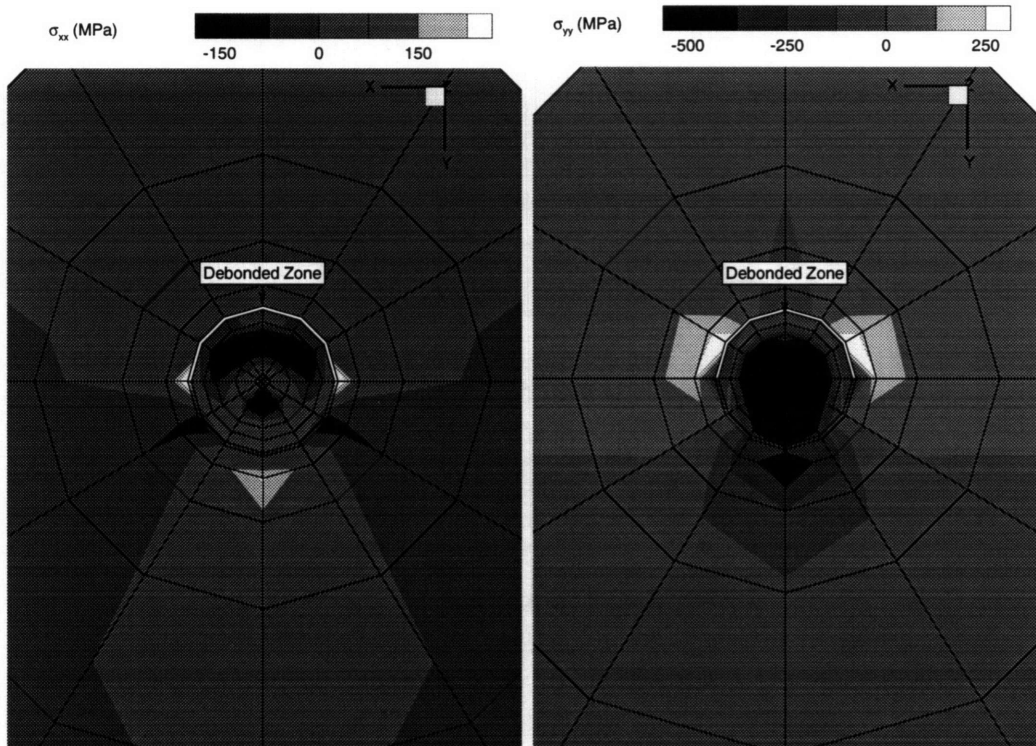


Figure 3-5: In-plane, σ_x and σ_y , stresses in a jacketed fiber at one fiber diameter from the crack face.

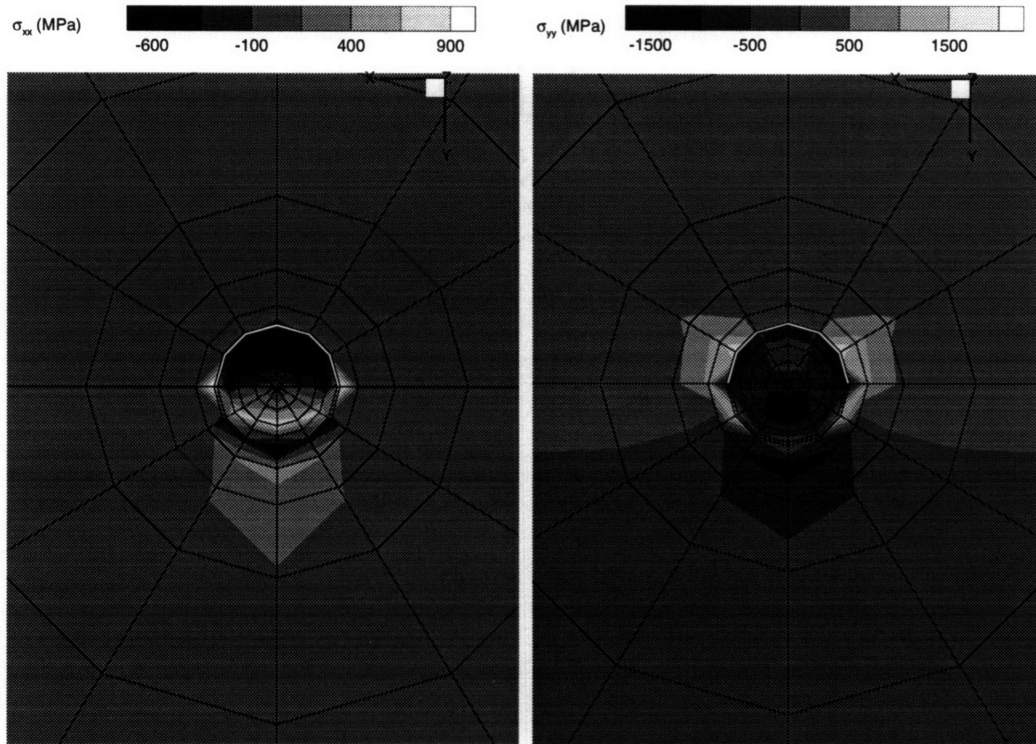


Figure 3-6: In-plane, σ_x and σ_y , stresses in a fiber without jacket.

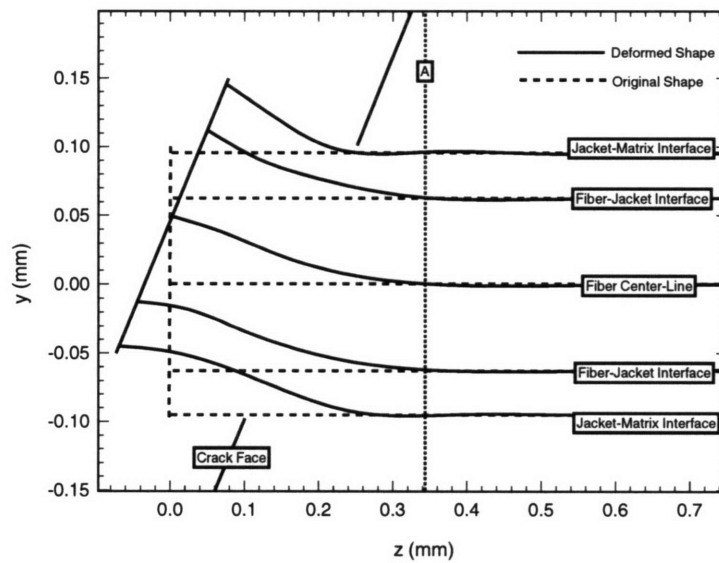


Figure 3-7: Comparison of deflected shape between fiber center-line, outer radius and jacket matrix interface.

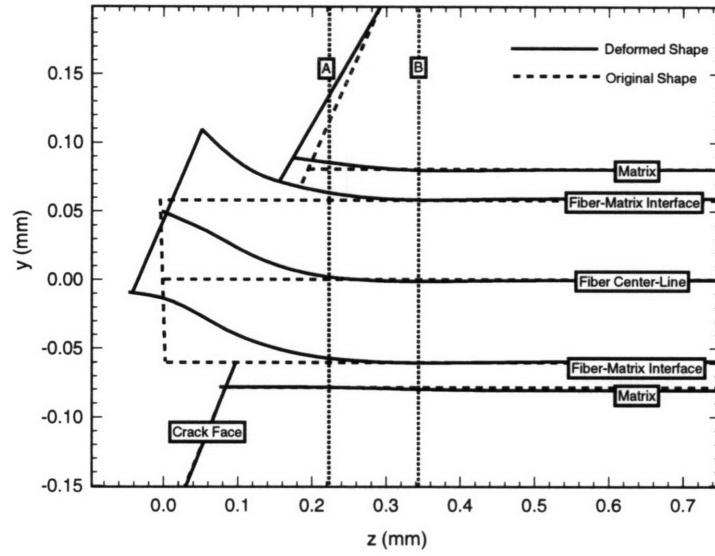


Figure 3-8: Fiber Deflected shape for the case of jacket free fiber.

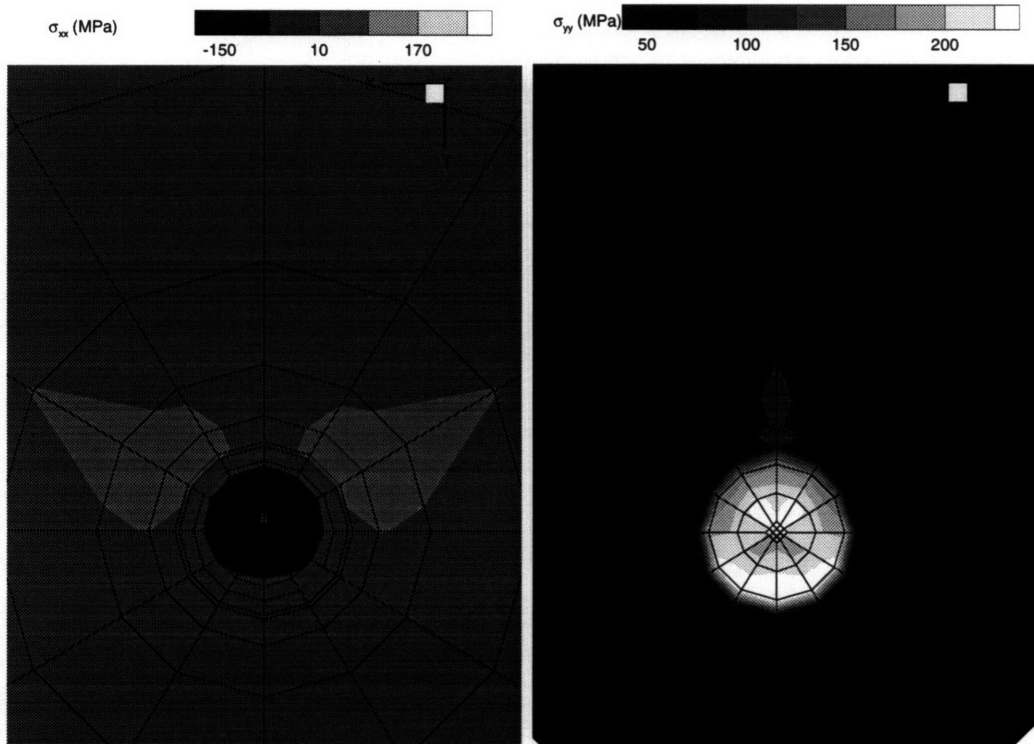


Figure 3-9: In-plane, σ_x and σ_y , stresses in a jacketed fiber at two fiber diameters from the crack face.

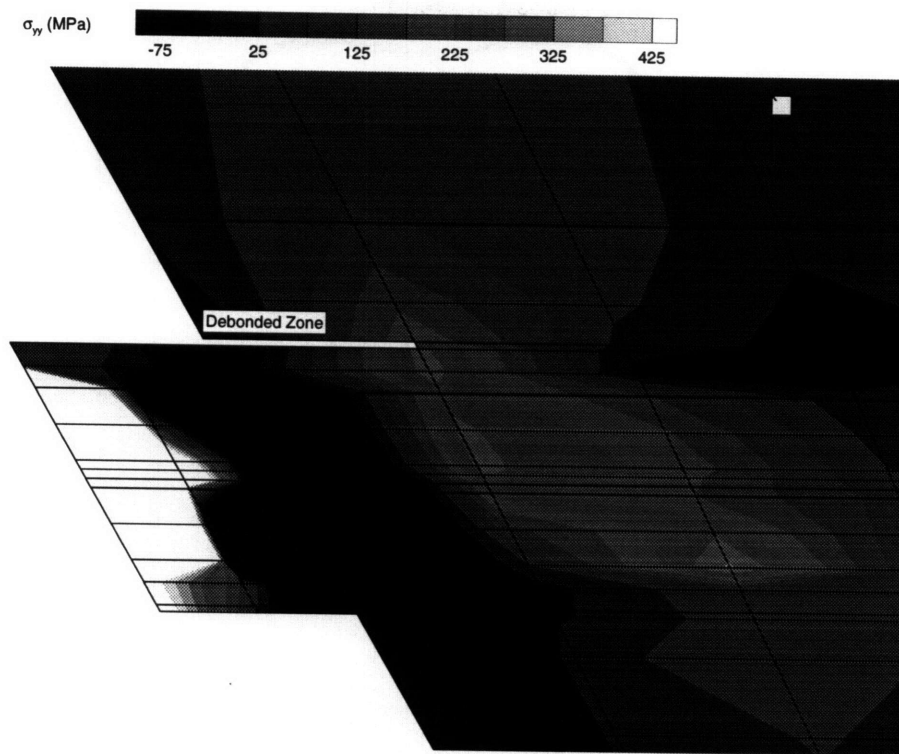


Figure 3-10: Stress concentration at the debonded zone

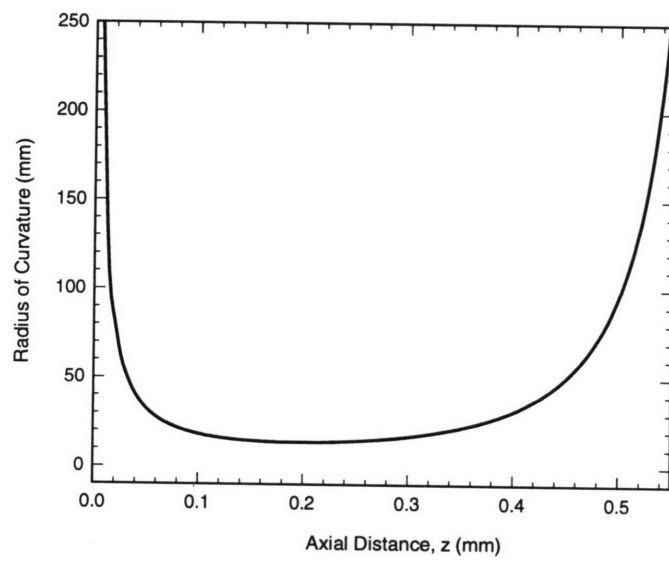


Figure 3-11: Radius of curvature along fiber center-line.

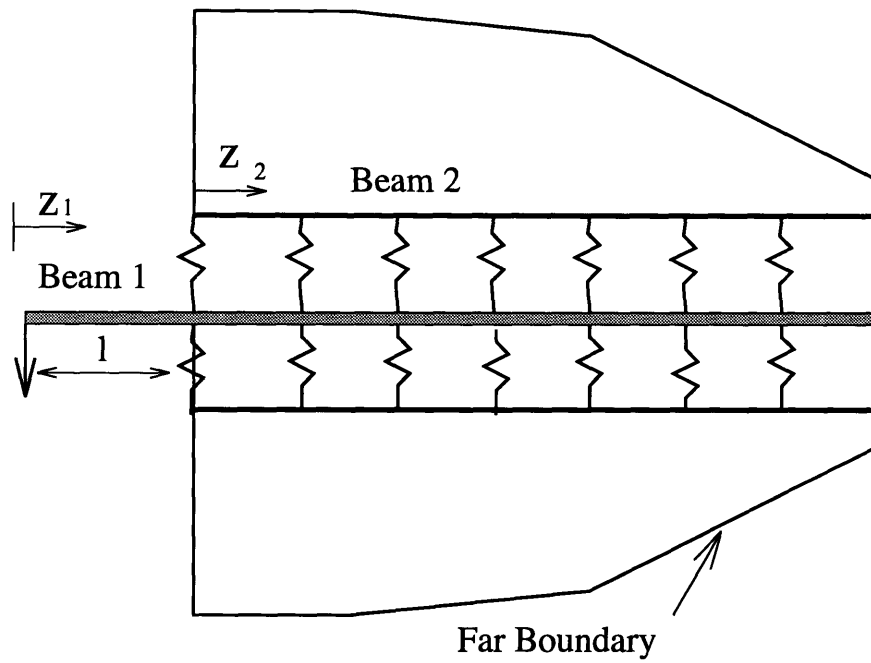


Figure 3-12: Beam on elastic foundation model of an embedded fiber in an elastic matrix.

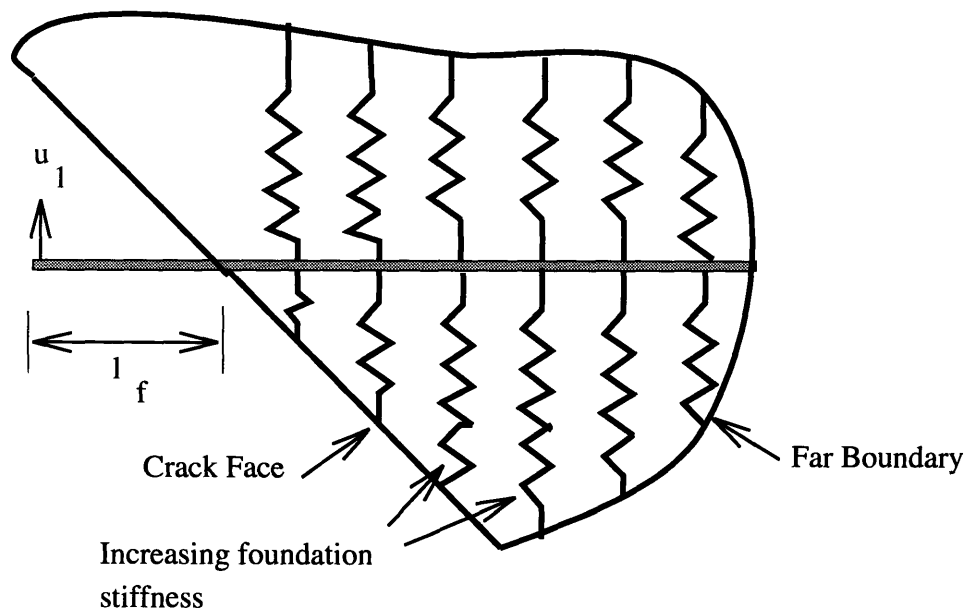


Figure 3-13: Beam on elastic foundation model for an oblique embedded fiber in an elastic matrix.

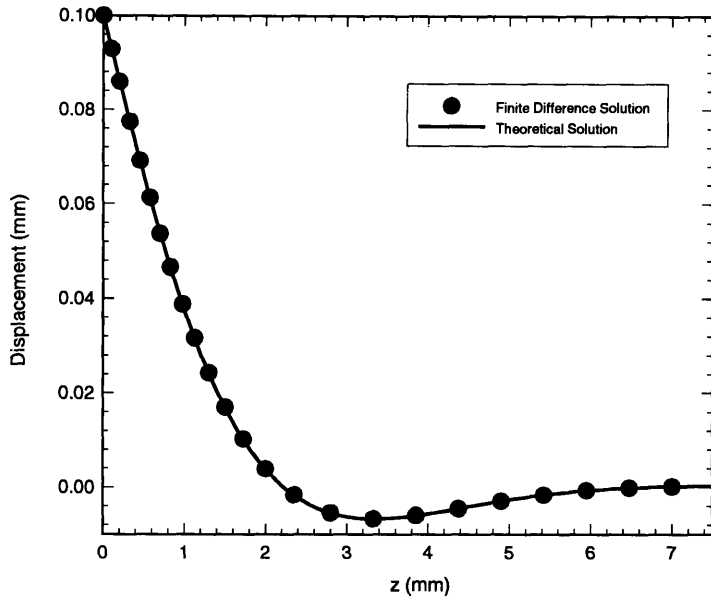


Figure 3-14: Comparison of Finite Difference and theoretical solution for beam on a linearly varying foundation stiffness, β .

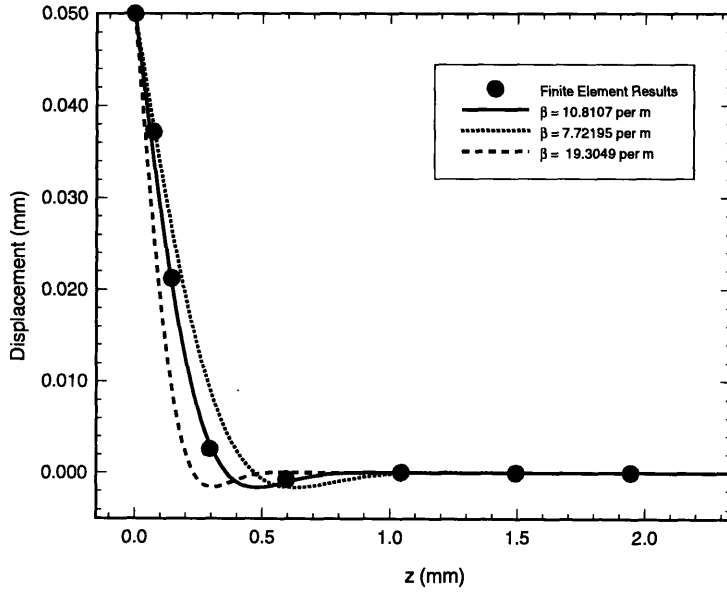


Figure 3-15: Comparison of Finite Element and Finite Difference results for the center-line deflection of the fiber with various assumed stiffnesses, β .

Chapter 4

Combined Mechanical and Electrical Behaviour of an Optic Fiber Under Bending

4.1 Introduction

Chapter 2 described the Beam Propagation Method (BPM) as a method of solving the electro-magnetic propagation problem of an arbitrarily curved optic fiber. Chapter 3 presented a method of finding the radii of curvatures in an inclined fiber bridging an open crack. This chapter presents results of the electro-mechanical behaviour of the fiber in order to find the electrical power loss associated with crack opening.

4.2 Method of Combined Mechanical and Electrical Analysis

This section presents the analysis method for calculating power attenuation in a fiber optic embedded in a tension cracked matrix. The basic algorithm for calculating electric power loss in a fiber optic sensor is :

- Select fiber geometry, material properties and crack opening.

- Calculate the fiber center-line deflection using the three dimensional finite element model.
- Find the equivalent foundation properties of the jacket and matrix material using the beam on an elastic foundation model.
- Using the equivalent foundation properties found in the previous step accurately calculate the fiber's center-line deflection.
- Calculate the radii of curvatures associated with the fiber deflection.
- Calculate the electric power attenuation caused by the changes in curvature found in the previous step

The fiber curvature cannot be accurately calculated directly from the finite element model since for accurate BPM calculations, step length increments of approximately $5\mu m$ are needed. In the 3D finite element analysis, element sizes less than 0.2 mm lead both to excessively long solution times and meshing problems associated with the limited aspect ratio of elements required for computational accuracy. The beam on an elastic finite difference model is used as a better physical approximation of the fiber action than a simple spline fit between the node displacements. Each three dimensional finite element simulation (including pre-processing, solution and post-processing) requires approximately 10 hours of computer time on a DEC 5000/25 workstation as opposed to 0.5 hours for the finite difference beam model. Due to the large time saving of the finite difference beam model over the finite element model, this pilot study only simulates four finite element cases for each particular geometric or material property change described in this section while other results are garnered using the finite difference beam on equivalent foundation model. This section investigates the effect of : (a) crack opening displacement (b) jacket elastic modulus, (c) fiber inclination angle at crack and (d) optical fiber characteristics, on electric power attenuation.

4.3 Results of the Combined Electro-Mechanical Analysis

This section presents the electric power attenuation associated with various fiber orientations and crack openings. Since the plastic jacket stiffness can be varied dependent on type of plastic used, the effect of jacket stiffness is also analysed.

4.3.1 Electric power Loss for Various Crack Opening Displacements and Fiber Orientations

Electric Power attenuation of fiber angles (θ) of 0 to 60° and crack opening displacements of 0.1 to 0.3 mm are investigated in this section. The model's mechanical characteristics are :

- Glass Fiber Radius = 100 μm .
- Plastic Jacket thickness = 50 μm .
- Cement Matrix Elastic Modulus = 20 GPa.
- Plastic Jacket Elastic Modulus = 3 GPa.
- Glass Fiber Elastic Modulus = 70 GPa.
- Poisson's ratio of all material = 0.2.

The model's optical characteristics are taken from the mono-mode optic fiber data provided by the Brown Fiber Optic Laboratory [1] :

- Waveguide width = 6 μm .
- Equivalent fiber core refractive index = 1.4613
- Equivalent fiber cladding refractive index = 1.458.
- Wavelength = 1.3 μm .

The equivalent foundation stiffness is assumed linearly dependent on jacket stiffness and fiber orientation. Hence :

$$\beta = a + b\theta + cE_j \quad (4.1)$$

where a, b and c are constants to be fitted by the FD analysis to the FEM analysis. The constants a, b and c are assumed independent of each other and β is assumed independent of the crack opening displacements. The constants a, b and c are calculated as follows :

1. Fix jacket elastic modulus $E_j = 3GPa$.
2. Fix fiber orientation θ .
3. Carry out the FEM analysis for four different crack openings.
4. Find modulus β by FD analysis that provides best fit to the FEM results.
5. Calculate the average foundation modulus β for the particular fiber orientation under the four crack opening displacements.
6. Repeat steps (2) to (5) for various fiber orientations θ .
7. Calculate the correlation coefficient of the fit for various fiber orientations to check the assumption of crack opening independence.

The comparison of the Finite Element results (FEM) and Finite Difference (FD) results generated by the above algorithm are presented in Figure (4-1) for various fiber orientations and crack openings. The FEM results differ from the FD results due to numerical inaccuracies associated with the FEM and the least square equivalent foundation fit, the match shows some statistical scatter with the average modulus being used in the FD analysis. The correlation coefficient between the FEM results and the average modulus FD analysis is 0.99 which is close to 1 and shows that the assumptions of independence is valid.

Figure (4-1) shows that for all fiber orientations, electric power attenuation increases as crack opening displacement increases. For fiber orientation angles of less than 45 degrees, power attenuation increases with increasing orientation angles (at the same crack opening displacement). For fiber angles greater than 45 degrees the power attenuation decreases. In chapter 2 it was noted that total power loss increases with decreasing radius of curvature. Total power loss also increases with increasing propagation distance along a constant curvature. Optic propagation length monotonically increases (and hence electric power loss increases) with increasing crack opening displacement.

Equation (3.1) shows that the applied fiber displacement increases with increasing fiber angle orientation. Radius of curvature increases (and hence electric power loss decreases) with increasing applied displacement which explains the increasing power loss at fiber orientations less than 45 degrees. Investigation of equation (3.14) shows that radius of curvature is dependent both on applied fiber displacement and on relative stiffness (β) of the founding layer. As fiber orientation angle increases the effective matrix bearing area of the fiber decreases and hence the stiffness decreases. Since in Figure (4-1) electric power loss decreases for fiber orientation angles greater than 45 degrees, the effect of foundation stiffness decrease and free fiber length increase dominates over increase in applied displacement. The increasing fiber free length is probably a dominant effect since it causes a reduction in fiber curvature which leads to a reduction in power loss. Hence for a set crack opening displacement, a fiber orientation around 45 degrees maximizes the electric power loss.

4.3.2 Electric Power Loss for Various Jacket Stiffnesses

This section analyzes the effect of jacket stiffness on electric power loss. The effect of jacket stiffness is assumed to be independent of fiber orientation in determining the overall equivalent foundation modulus β as shown by equation (4.1). The effect of jacket stiffness is studied in the following way :

1. Fix crack opening displacement $u = 0.2mm$.
2. Fix fiber orientation θ .
3. Carry out the FEM analysis for four different jacket moduli.
4. Find modulus β from FD analysis that best fits the FEM results.
5. Calculate the average foundation modulus β for the particular fiber orientation under the four jacket stiffnesses.
6. Repeat steps (2) to (5) for various fiber orientations θ .
7. Calculate the correlation coefficient of the fit for various fiber orientations to check whether the jacket elastic modulus is independent of fiber orientation (correlation coefficient equal to 1 shows independence).

Figure (4-2) shows the electric power loss for various jacket stiffnesses and fiber orientations. The correlation coefficient is 0.96 for all jacket stiffnesses showing that the assumption behind independent behaviour of the jacket material and fiber orientation is valid. Figure (4-2) shows that as discussed in the previous section the radius of curvature decreases (and hence electric power loss increases) with increasing stiffness. Figure (4-2) once again shows the competing effects of decreased bearing area leading to decreased stiffness and increasing fiber applied displacement leading to increased optic propagation length. From Figure (4-2) it can be interpreted that a fiber oriented at 45 degree has increasing sensitivity with jacket stiffness. The practical limit to jacket stiffness is discussed in the next chapter.

The foundation modulus is best fitted in a least square sense by the function :

$$\beta = 13.0925 - 0.1725\theta + 1.1078E_j \quad (4.2)$$

where θ is given in degrees and E_j is in GPa. As expected foundation stiffness increases with increasing jacket stiffness and decreases with increasing fiber crack-face orientation.

4.3.3 Electric Power Loss for Various Cut-off Frequencies

This section analyses the effect of the electro-magnetic characteristics of the optic waveguide on the overall sensitivity of the optic fiber sensor. The electric power loss for fixed radius of curvature is strongly dependent on :

- wave number, k .
- width of optic core, a .
- refractive index of core, n_1 .
- Refractive index of cladding, n_2 .

The above parameters can be combined into a dimensionless number known as the cut-off frequency introduced as v in equation (2.44). The cut-off frequency has the advantage that it is independent of n_a which can only be determined by solving the non-linear equation (2.40). The slab core eigenvalue (u) and slab cladding eigenvalue (w) given by equation (2.42) and (2.43) are related by equation (2.44). Combining equation (2.42) through (2.44) gives :

$$v = k\sqrt{n_1^2 - n_2^2}a \quad (4.3)$$

The Marcuse relationship equation (2.49) suggests that for a constant curvature slab guide, increasing cut-off frequency (for mono-mode waveguides) leads to decreasing sensitivity. Equation (4.3) shows that decreased cut-off frequency can be achieved through either reducing the slab width ($2a$) or the difference in cladding to core refractive index (n_1 to n_2). Figure (4-3) verifies the trend suggested by Marcuse equation for varying curvatures for fixed crack opening displacement ($u = 0.2$ mm) and jacket stiffness (3 GPa). Figure (4-3) shows a reverse in trend between the 45° and 60° fiber for very sensitive (i.e. small cut-off frequency) fibers due to the fact that increasing light propagation length dominates over reduction in radius of curvature caused by increasing free length.

The practical implication of reducing the cut-off frequency is discussed in the following chapter.

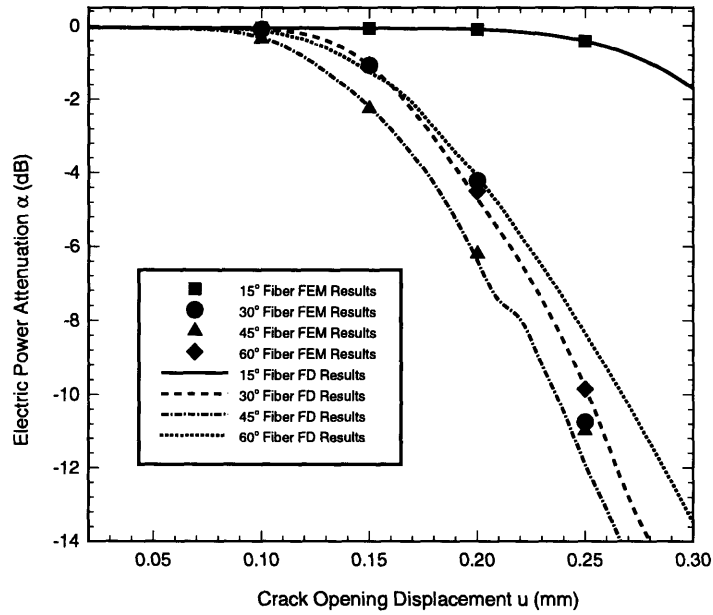


Figure 4-1: Effect of Crack Opening Displacement and fiber orientation on electric power attenuation by the finite element method (FEM) and the finite difference method (FD)

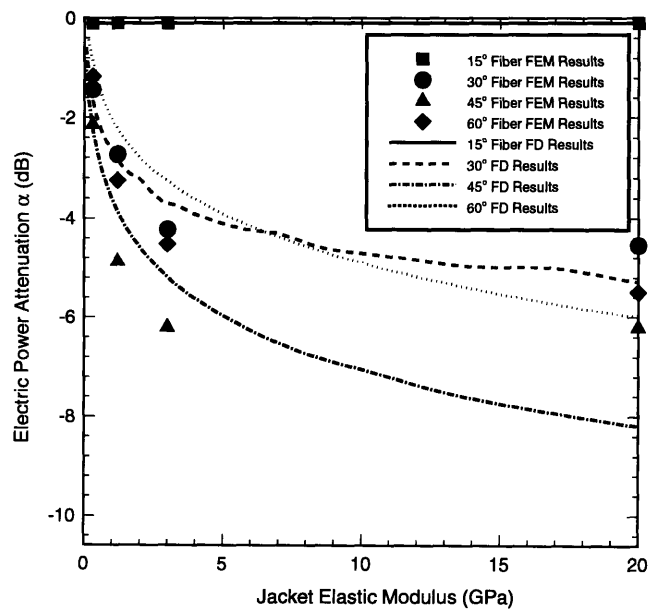


Figure 4-2: Effect of Jacket Elastic Modulus on electric power attenuation.

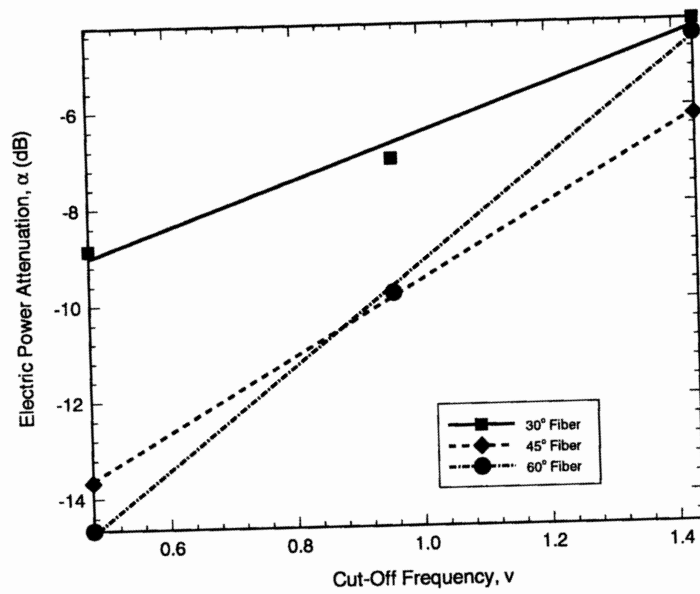


Figure 4-3: Effect of Cut-off Frequency on electric power attenuation.

Chapter 5

Discussion of Results and Recommendations

5.1 Summary of findings

Chapter 4 has concentrated on studying the electro-mechanical behaviour of fiber optic sensors used for tension crack detection by crack bridging. The main findings are :

1. Electric power loss increases with increasing crack opening.
2. Electric power loss increases with increasing jacket stiffness.
3. Electric power loss increases with decreasing cut-off frequency.
4. Electric power loss is maximum for fiber-crack incidence angles around 45° .

It is desirable to increase electric power loss (within practical limits) since power loss is directly linked to crack detectability. This section focuses on some of the practical aspects of changing the above parameters.

5.1.1 Crack Opening

Voss and Wanser [2] have experimentally shown the feasibility of using surface-mounted crack bridging sensors for detecting cracks with opening displacements in

the millimeter range. For practical structures, this magnitude of crack opening is easily detectable by visual inspection and exceeds the required opening detectability of approximately 0.2 mm for concrete structures by an order of magnitude. In general, the integrity monitoring of concrete structures in critical applications such as power plants and water retaining structure should allow sensing of cracks in the 0.1 mm range. For reliable structure integrity monitoring, the sensing scheme should allow for adequate warning of cracks approaching the critical opening. Adequate warning for a 0.1 mm critical crack opening, implies that the sensing scheme should be able to detect cracks less than 0.1 mm in length. Having set the required crack opening displacement range in accordance with the structural application, the other sensing parameters need to be modified in order to allow for sufficient sensitivity.

5.1.2 Jacket Stiffness

Investigation of the effect of jacket stiffness has shown increasing sensitivity with increasing jacket stiffness. Jacketing material is required also to (i) prevent chemical attack, subsequent embrittlement and final failure of the glass fiber and (2) to protect the matrix material from spalling due to large stress transferal. Damage of the matrix by spalling causes a reduction of the equivalent foundation modulus and for power loss to decrease. Consequently spalling limits the increase of power loss by increasing jacket stiffness. The effect of a damaging matrix requires non-linear analysis and is beyond the scope of this work. The randomness of spalling also makes it difficult to interpret results quantitatively.

5.1.3 Cut-off Frequency

Low cut-off frequency optic fibers are often called lossy due to the fact that the electric signal rapidly attenuates due to large radius bends making the fiber unsuitable for waveguide propagation over long distances. Large radius bends can be introduced in a sensing system due to fabrication, differential temperature and creep strains. Though increased sensitivity is achieved through cut-off frequency reduction, careful design

is needed to ensure adequate signal propagation. The commercially available fiber which have been used throughout the simulations in this work has been tested not to suffer from excessive power loss due to fabrication, creep and temperature effects.

5.1.4 Fiber Orientation

In the case when the likely orientation of the tension damage is known (such as flexural cracks in concrete beams), the orientation of the fiber can be controlled so as intersect the crack at 45° . In the case when the orientation of the crack is unknown, it is possible that intersection may occur at very low incidence angles causing undetectable power loss. In such cases, a network of sensors is needed in order to ensure crack-fiber intersection within sensing range. Another advantage of network sensing is that it allows for accurate location of the crack through a system of triangulation. The obvious disadvantage of network sensing is that fabrication can be expensive.

5.2 Conclusion

This section has developed a three dimensional electro-mechanical model to study the effects of sensing parameters on tension crack detection. The major finding is that commercially manufactured crack-bridging optic fibers can be successfully used to detect crack openings of practical magnitudes occurring in concrete structures. Four possible design parameters effecting crack detectabilty have been identified, namely (a) crack opening displacement, (b) founding material stiffness which is mainly affected by fiber jacket stiffness, (c) optical characteristics of the fiber and (d) fiber orientation. The manipulation of the sensing parameters can allow a fiber-sensor designer to select a feasible crack detection layout with differing material and geometrical properties.

Bibliography

- [1] L. Reinhart. *Personal Communcation*. (1994).
- [2] K. F. Voss and K. H. Wanser. *Fiber sensors for monitoring structural strain and cracks*. Second European conf. on Smart Structures and Materials. (Glasgow). 144-147. (1994).

Chapter 6

Application of Fiber Optic Sensing in Delamination Detection

6.1 Introduction

Recent advances in adaptive materials have focused on the ability of the material to recognize when it has been damaged. Traditional methods of structural integrity monitoring through non-destructive evaluation (NDE) techniques such as ultrasound C-scan [9] and x-ray detection [5] requires considerable time and experience. Furthermore, these techniques tend to be expensive and frequently unreliable [11]. Fiber optic sensors have several advantages over traditional NDE techniques [16] which include (a) intrinsic safety, (b) resistance to corrosion which plagues embedded metallic sensors in highly alkaline environments such as concrete, (c) reduced weight and size and (d) reliability. Furthermore the final aim of industrial adaptive materials programs (such as Boeing's smart skin program [16]) is to integrate the sensing device with the crew interface to advise the crew of the integrity of the structure and to deduce limitations on aircraft performance by the damage detected. Due to the above mentioned advantages of fiber optic sensors, they are ideal for real time monitoring in such applications.

In composite structures, damage frequently occurs in a direction perpendicular to

the load application. In advanced composite structures, this type of damage manifests itself as delaminations between individual ply laminates during relatively low energy impacts such as dropped tools or in-flight collision with birds [13]. For manufacturing purposes and for minimizing the structural weakening of the composite, the through-thickness weaving of the fiber optic sensor is avoided. In reinforced concrete, structures delamination damage can occur below concrete deck overlays or reinforcement planes due to the chemical attack of the reinforcement.

Previous work in fiber optic delamination sensing [10] has focused on embedding etched optical fibers with known stress sensitivity into composite laminates. The method relies on power loss detection after fiber breakage occurs due to increased stresses at the delaminated zone. The disadvantages of this method is that it gives no indication of the position and size of the delaminated zone and the large number of fibers needed for this detection scheme structurally weakens the composite. Recent work in fiber optic delamination sensing [2] has researched the use of embedded fiber optic strain sensors to determine the changes in vibration signature caused by delamination. Problems with this method are that expensive computer software is needed to process the vibration signal and actual dynamic loading requires sophisticated equipment and experienced operators.

This research focuses on the feasibility of using fiber optic strain sensors positioned parallel to the occurring damage for delamination detection by monitoring changes in strain caused by delamination growth. Attention is given to (1) presenting the theoretical elasticity mechanics required to determine the strain field for particular flexural delamination problems, (2) identification of the critical geometric damage detection parameters, and (3) presenting the sensing characteristics of common fiber optic sensors. Theoretical and numerical solution methods are used to map the effect of damage on the global strain field. The strain maps are subsequently used to locate the position of the fiber sensor for reliable damage detection by maximizing the cumulative strain effect of the crack. Two case studies are presented in order to establish

the feasibility of using the proposed detection scheme in real world aerospace and civil applications by comparing the strain perturbation caused by delamination to the strain sensitivity of current fiber optic sensors.

6.2 Mechanics of delaminated flexural members

6.2.1 Introduction

This section develops the elastic mechanics required to solve flexural delamination problems so that the strains associated with delamination can be calculated. The delamination strains are needed for studying the applicability of various fiber optic sensing schemes and the calculation of fiber damage sensing fidelity. The study of the mechanical behaviour of a delaminated cantilever beam is investigated since (a) cantilever beams frequently occur in structural components such as wings and propellor blades in aerospace applications and overhang beams in concrete structures, (b) the elastic mechanics has closed form solutions, and (c) the results can be applied to any linear distribution of moment which occur under point load flexural members and by superposition to any load distribution. Knowing the mechanical behaviour of a delaminated cantilever beam allows for the solution of more complicated delaminated flexural problems.

6.2.2 Fundamental Equations in Complex Potential Plane Elasticity Theory

This section derives the fundamental isotropic elasticity equations required to solve a cantilever rigidly supported at one end and loaded with a transverse shear load (Q) as shown in Fig. (6-1) using the complex potential method developed by Muskhelishvili [12] and Savin [14]. The theory and results in this chapter can be extended to include any boundary conditions and any number of point loads which satisfy the beam bending model by superposition.

The basic idea behind the Muskhelishvili method is to solve the unweakened (beam

without damage) elasticity problem and to superpose a solution of the elasticity problem which matches the stress boundary conditions at the hole without effecting the boundary conditions of the unweakened beam. In general, this type of solution is only possible if the effect of the hole is localized or effectively if the plate's dimensions are infinite. For practical elasticity solutions this means that the smallest dimensions of the plate must be much greater than the dimensions of the hole (Muskhelishvili [12] recommends a minimum of 5 to 1 plate to hole dimension). By the uniqueness theorem of elasticity (see for example Timoshenko [17]) any assumed solution that satisfies the elasticity equations and boundary conditions gives the unique solution to the problem.

For plane elasticity problems (plane stress or strain), it can be shown [17] that the elasticity equations need to satisfy the Airy stress function given by :

$$\frac{\partial^4 U}{\partial x^4} + 2\frac{\partial^4 U}{\partial x^2 \partial y^2} + \frac{\partial^4 U}{\partial y^4} = 0 \quad (6.1)$$

The in-plane stresses can be recovered from :

$$\sigma_x = \frac{\partial^2 U}{\partial y^2}; \quad \sigma_y = \frac{\partial^2 U}{\partial x^2}; \quad \tau_{xy} = -\frac{\partial^2 U}{\partial y \partial x} \quad (6.2)$$

Natural (stress) boundary conditions can be expressed as :

$$\begin{aligned} \frac{\partial U}{\partial y} &= \int_0^s (\sigma_x \cos(n, x) + \tau_{xy} \cos(n, y)) ds; \\ \frac{\partial U}{\partial x} &= \int_0^s (\sigma_y \cos(n, y) + \tau_{xy} \cos(n, x)) ds; \end{aligned} \quad (6.3)$$

where s represents the boundary line and n represents the normal to the boundary surface.

Muskhelishvili has shown that for two-dimensional elasticity problems, the solution

to the Airy equation (6.1) can be expressed as :

$$U(x, y) = \Re[\bar{z}\psi(z) + \chi(z)] \quad (6.4)$$

where \Re is the real part of the square brackets and $\psi(z)$ and $\chi(z)$ are conjugate functions of the complex variable $z = x + iy$ and $\bar{z} = x - iy$. The solution of the elasticity problem is then equivalent to finding the analytical functions $\psi(z)$ and $\chi(z)$ that satisfy the boundary conditions which are expressed in complex harmonic form as :

$$\frac{\partial U}{\partial x} + i\frac{\partial U}{\partial y} = \psi(z) + z\overline{\psi'(z)} + \overline{\phi(z)} = f_1 + if_2 \quad (6.5)$$

Once the functions $\psi(z)$ and $\chi(z)$ have been determined, the Kolosov-Muskhelishvili formulae give the stress components as :

$$\begin{aligned} \sigma_x + \sigma_y &= 2[\psi'(z) + \overline{\psi'(z)}] \\ \sigma_y - \sigma_x + 2i\tau_{xy} &= 2[\bar{z}\psi''(z) + \overline{\phi'(z)}] \end{aligned} \quad (6.6)$$

where a prime denotes differentiation with respect to the complex variable z and $\phi = \frac{d\chi}{dz}$.

The individual stress components are then determined by equating real and imaginary parts of equation (6.6).

For the solution of elastic plate problems weakened with a hole, it is convenient to transform the elastic region onto the inside of a unit circle by means of a mapping function $z = \omega(\xi)$. For elliptical holes this transformation is given by :

$$z = \omega(\xi) = R\left(\frac{1}{\xi} + m\xi\right) \quad (6.7)$$

where

$$m = \frac{a-b}{a+b}; \quad R = \frac{a+b}{2} \quad (6.8)$$

and a and b are the major and minor ellipse axis lengths respectively.

In polar coordinates ($\xi = \rho e^{i\theta}$) equation (6.7) and its conjugate are :

$$\begin{aligned} z = \omega(\xi) &= R\left(\frac{e^{-i\theta}}{\rho} + m\rho e^{i\theta}\right) \\ \bar{z} = \overline{\omega(\xi)} &= R\left(\frac{e^{i\theta}}{\rho} + m\rho e^{-i\theta}\right) \end{aligned} \quad (6.9)$$

Substituting $\omega(\xi)$ into equation (6.5), gives the natural boundary conditions on the unit circle in polar coordinates as :

$$\psi(\sigma) + \frac{\omega(\sigma)}{\omega'(\sigma)} \overline{\psi'(\sigma)} + \overline{\phi(\sigma)} = f_1 + if_2 \quad (6.10)$$

where $\xi = \sigma$ at the outer radius of the unit circle.

Muskhelishvili [12] has shown that the boundary conditions given in equation (6.5) can be rewritten as :

$$\psi(\xi) + \frac{1}{2\pi i} \int_{\gamma} \frac{\omega(\sigma)}{\omega'(\sigma)} \frac{\overline{\phi'(\sigma)}}{\sigma - \xi} d\sigma = \frac{1}{2\pi i} \int_{\gamma} \frac{f_1 + if_2}{\sigma - \xi} d\sigma \quad (6.11)$$

$$\phi(\xi) + \frac{1}{2\pi i} \int_{\gamma} \frac{\overline{\omega(\sigma)}}{\omega'(\sigma)} \frac{\psi'(\sigma)}{\sigma - \xi} d\sigma = \frac{1}{2\pi i} \int_{\gamma} \frac{f_1 - if_2}{\sigma - \xi} d\sigma \quad (6.12)$$

where γ is the closed contour boundary of the unit circle.

Substituting $\omega(\xi)$ into equation (6.6), the polar stresses are given by [14]:

$$\begin{aligned} \sigma_{\rho} + \sigma_{\theta} &= 2[\Phi(\xi) + \overline{\Phi(\xi)}]; \\ \sigma_{\rho} - \sigma_{\theta} &= \frac{2\xi^2}{\rho^2 \omega'(\xi)} [\overline{\omega(\xi)} \Phi'(\xi) + \omega' \Psi(\xi)] \end{aligned} \quad (6.13)$$

where

$$\Phi(\xi) = \frac{\psi'(\xi)}{\omega'(\xi)}; \quad \Psi(\xi) = \frac{\phi'(\xi)}{\omega'(\xi)}; \quad (6.14)$$

6.2.3 Derivation of Complex Potentials for the Problem of the Cantilever Beam with Elliptical Hole

This section uses the formulae from the previous section (6.2.2) to derive the stress distribution in a cantilever beam with an elliptical hole as shown in Fig (6-1). Savin [14] has derived the stress functions for an elastic isotropic cantilever beam with an elliptical hole positioned at the mid-height of the beam ($d = 0$). This analysis extends Savin's work to allow for the elastic solution of an elliptic hole at any height (d) above the beam center-line.

The stress function for the unweakened beam is given by :

$$U_o(x, y) = Q \frac{(l - c)(y^3 + 3dy^2) - xy^3 - 3dxy^2 + 3xy(h^2 - d^2)}{6J}; \quad (6.15)$$

where

U_o is the unweakened (basic) stress state.

Q is the total applied shear force.

J is the second moment of area of the beam.

l, c, d, h are the beam dimensions as shown in Fig. (6-1).

Using equation (6.2) the stress components are :

$$\begin{aligned} \sigma_x &= \frac{Q}{J} [(l - c)(y + d) - x(y + d)] \\ \sigma_y &= 0 \\ \tau_{xy} &= \frac{Q}{2J} [(y + d)^2 - h^2] \end{aligned} \quad (6.16)$$

Combining equations (6.6) and (6.2) for the basic stress state, we obtain :

$$\Delta U_o = \frac{\partial^2 U_o}{\partial x^2} + \frac{\partial^2 U_o}{\partial y^2} = 4\Re[\psi'_o(z)] \quad (6.17)$$

where the subscript o denotes the basic (unweakened) stress state. Setting $[\psi'_o(z)] = P(x, y) + iQ(x, y)$ we obtain :

$$\frac{\partial^2 U_o}{\partial x^2} + \frac{\partial^2 U_o}{\partial y^2} = 4P(x, y) \quad (6.18)$$

The function $Q(x, y)$ can be calculated using the Cauchy-Reiman equations :

$$\frac{\partial P(x, y)}{\partial x} = \frac{\partial Q(x, y)}{\partial y}; \quad \frac{\partial P(x, y)}{\partial y} = -\frac{\partial Q(x, y)}{\partial x}; \quad (6.19)$$

The function $\chi'_o(z) = \phi_o(z)$ can then be determined using equation (6.4) and writing $\chi_o(z) = R(x, y) + iS(x, y)$ as :

$$R(x, y) = U_o(x, y) - \frac{1}{2}[\bar{z}\psi_o(z) + z\overline{\psi_o(z)}] \quad (6.20)$$

Subsequently $S(x, y)$ is determined from the analogous expressions to equations (6.19).

For the stress function (6.15) :

$$\frac{\partial^2 U_o}{\partial x^2} + \frac{\partial^2 U_o}{\partial y^2} = 4P(x, y) = \frac{Q}{J}((l - c)(y + d) - x(y + d)) \quad (6.21)$$

Solving equation (6.19) gives $4Q(x, y) = -\frac{Q}{2J}(2x(l - c) - x^2 + y^2 + 2dy)$

and constant terms which do not effect the stress components are neglected. Consequently :

$$\psi'_o(x, y) = \frac{Q}{J} \left[\frac{1}{4}((l - c)(y + d) - x(y + d)) - \frac{i}{24}(6x(l - c) + 3(y^2 - x^2) + 6dy) \right] \quad (6.22)$$

Combining terms in $z = x + iy$ and integrating we get :

$$\psi_o(z) = \frac{Q}{24J}(-3iz^2(l - c) - 3dz^2 + iz^3 + 6d(l - c)z) \quad (6.23)$$

Using equation (6.20) and solving the Cauchy-Reiman equations (6.19) for S gives :

$$\chi_o(z) = \frac{Q}{48J}(-12iz^2(h^2 - d^2) - 12d(l - c)z^2 + 2iz^3(l - c) + 6dz^3 - iz^4) \quad (6.24)$$

Hence

$$\phi_o(z) = \frac{Q}{24J}(-12iz(h^2 - d^2) - 12d(l - c)z + 3iz^2(l - c) + 9dz^2 - 2iz^3) \quad (6.25)$$

Applying the principal of superposition and noting that the hole boundary is traction free gives :

$$f_{o1} + if_{o2} + f_{w1} + if_{w2} = 0 \quad (6.26)$$

where the subscript o denotes the basic (unweakened) stress state on the hole contour and the subscript w denotes the applied tractions required for zero stress on the hole boundary.

Substituting the expressions ψ_o and ϕ_o into equation (6.5) gives :

$$\begin{aligned} f_{w1} + if_{w2} = \frac{Q}{24J} & [3iz^2(l - c) + 3dz^2 - iz^3 - 6zd(l - c) - 6iz\bar{z}(l - c) + \\ & + 6z\bar{z}d + 3iz\bar{z}^2 - 12i\bar{z}(h^2 - d^2) + 12\bar{z}d(l - c) + 3i\bar{z}^2(l - c) - \\ & - 9d\bar{z}^2 - 2i\bar{z}^3] \quad (6.27) \end{aligned}$$

$$\begin{aligned} f_{w1} - if_{w2} = -\frac{Q}{24J} & [3i\bar{z}^2(l - c) - 3d\bar{z}^2 - i\bar{z}^3 + 12\bar{z}d(l - c) - 6iz\bar{z}(l - c) + \\ & - 6z\bar{z}d + 3i\bar{z}z^2 - 12iz(h^2 - d^2) - 12zd(l - c) + 3iz^2(l - c) - \\ & + 9dz^2 - 2iz^3] \quad (6.28) \end{aligned}$$

Substituting the conformal mapping equation (6.7) into equations (6.27) and (6.28) and applying the right hand side of equations (6.11) and (6.12) together with the

Cauchy Residue Theorem (see for example [7]) yields :

$$\begin{aligned} \frac{1}{2\pi i} \int_{\gamma} \frac{f_{w1} + if_{w2}}{\sigma - \xi} d\sigma &= \frac{QR}{24J} (12\xi d(l-c) - 9\xi^2 dR + 3iR^2\xi - 12i\xi(h^2 - d^2) - 2i\xi^3 R^2 \\ &+ 3m^2\xi^2 dR - 12m\xi d(l-c) + 6m\xi^2 dR + 3iR^2 m^2\xi + \\ &3im^2\xi^2 R(l-c) - im^3\xi^3 R^2 - 6im\xi^2 R(l-c) + \\ &3im\xi^3 R^2 + 3i\xi^2 R(l-c) - 6i\xi R^2 m); \end{aligned} \quad (6.29)$$

$$\begin{aligned} \frac{1}{2\pi i} \int_{\gamma} \frac{f_{w1} - if_{w2}}{\sigma - \xi} d\sigma &= -\frac{QR}{24J} (12\xi d(l-c) - 3\xi^2 dR - i\xi^3 R^2 + 9m^2\xi^2 dR - 12m\xi d(l-c) - \\ &6m\xi^2 dR - 6iR^2 m^2\xi + 3im^2\xi^2 R(l-c) - 2im^3\xi^3 R^2 - \\ &6im\xi^2 R(l-c) + 3i\xi^2 R(l-c) + 3i\xi R^2 m + 3i \\ &\xi^3 R^2 m^2 + 3iR^2 m^3\xi - 12im\xi(h^2 - d^2)) \end{aligned} \quad (6.30)$$

It can be shown [14] that in equation (6.11) the second integral is zero for elliptic holes, and :

$$\psi_w(\xi) = \frac{1}{2\pi i} \int_{\gamma} \frac{f_1 + if_2}{\sigma - \xi} d\sigma \quad (6.31)$$

Hence

$$\begin{aligned} \psi_w(\xi) &= \frac{i}{24} [BR^3\xi^3(m^3 - 3m + 2) + 3AR^2\xi^2(m-1)^2 + 3BR^3\xi(2m-1-m^2) - 24ER\xi] \\ &+ \frac{d}{24} [3BR^2\xi^2(3-2m-m^2) + 12A\xi R(1-m)] \end{aligned} \quad (6.32)$$

Here

$$A = \frac{Q(l-c)}{J}; \quad B = -\frac{Q}{J}; \quad E = \frac{Q(h^2 - d^2)}{2J} \quad (6.33)$$

Evaluating the second integral on the left hand side of equation (6.12) gives

$$\begin{aligned} \frac{1}{2\pi i} \int_{\gamma} \frac{\overline{\omega(\sigma)} \psi'_w(\sigma)}{\omega'(\sigma) \sigma - \xi} d\sigma &= \frac{\xi^3 + m\xi}{m\xi^2 - 1} \left[\frac{i}{24} (3BR^3\xi^2(m^3 - 3m + 2) + 6AR^2\xi(m-1)^2 \right. \\ &+ 3BR^3(2m-1-m^2) - 24ER) + \frac{d}{24} (6BR^2\xi(3-2m-m^2) \\ &+ 12AR(1-m))] \end{aligned} \quad (6.34)$$

Rearranging equation (6.12) gives :

$$\begin{aligned}
\phi_w(\xi) = & -\frac{\xi^3 + m\xi}{m\xi^2 - 1} \left[\frac{i}{24} (3BR^3\xi^2(m^3 - 3m + 2) + 6AR^2\xi(m-1)^2 \right. \\
& + 3BR^3(2m - 1 - m^2) - 24ER) + \frac{d}{24} (6BR^2\xi(3 - 2m - m^2) \\
& + 12AR(1 - m)) \left. \right] - \frac{i}{24} [BR^3\xi^3(1 + 2m^3 - 3m^2) \\
& + 3AR^2\xi^2(m-1)^2 + 3BR^3\xi(2m^2 - m^3 - m) - 24ERm\xi] \\
& - \frac{d}{24} [12AR\xi(1 - m) + 3BR^2\xi^2(1 + 2m - 3m^2)] \tag{6.35}
\end{aligned}$$

The stress function for the basic and unweakened beam need to be added to give the total stress state. This gives :

$$\begin{aligned}
\psi_o + \psi_w = \psi = & -\frac{i}{24} (BR^3(\frac{1}{\xi} + m\xi)^3 + 3AR^2(\frac{1}{\xi} + m\xi)^2) + \\
& \frac{d}{24} (3BR^2(\frac{1}{\xi} + m\xi)^2 + 6AR(\frac{1}{\xi} + m\xi)) + \psi_w \tag{6.36}
\end{aligned}$$

$$\begin{aligned}
\phi_o + \phi_w = \phi = & \frac{i}{24} (2BR^3(\frac{1}{\xi} + m\xi)^3 + 3AR^2(\frac{1}{\xi} + m\xi)^2 - 24ER(\frac{1}{\xi} + m\xi)) \\
& - \frac{d}{24} (9BR^2(\frac{1}{\xi} + m\xi)^2 + 12AR(\frac{1}{\xi} + m\xi)) + \phi_w \tag{6.37}
\end{aligned}$$

Constraining the crack to lie on the beam center-line (d equal to zero in the above equations), the same stress functions as derived by Savin [14] are recovered except for a negative sign in the numerator of the first term of ϕ_w which Savin has as $m\xi^2 + 1$. Since this factor is only dependent on the shape of the hole (it is the $\omega(\sigma)\overline{\omega'(\sigma)}$ term in equation (6.12)), this term is independent of the boundary conditions of the problem. An investigation of other elliptic hole problems solved by Savin [14] has shown that the geometric transformation factor $m\xi^2 - 1$ term in ϕ_w is consistent with these solutions. (See for example the stress functions derived for the elliptic hole under pure tension).

6.2.4 Derivation of Stresses and Strains

Stresses are derived from the complex stress functions from equations (6.13). Since the equations require finding the real and imaginary part of very complicated functions, this is best done numerically for any value of $\xi = re^{i\theta}$. Cartesian stresses are determined from the polar stresses by standard coordinate rotations (see for example Timoshenko [17]). The cartesian coordinates (x,y) for any value of ξ are calculated by equating the real and imaginary parts of equations (6.9).

The strains are determined in accordance with the assumed constitutive behaviour. In plane stress this is given by the standard:

$$\begin{Bmatrix} \epsilon_x \\ \epsilon_y \\ \gamma_{xy} \end{Bmatrix} = \frac{1}{E} \begin{bmatrix} 1 & -\nu & 0 \\ -\nu & 1 & 0 \\ 0 & 0 & 2(1 + \nu) \end{bmatrix} \begin{Bmatrix} \sigma_x \\ \sigma_y \\ \tau_{xy} \end{Bmatrix} \quad (6.38)$$

6.3 Validation of Theoretical Results

6.3.1 Introduction

This section validates the derived theoretical solution by comparing stresses for two numerical example problems. The first example problem confirms Savin's previously derived solution for the stresses at the hole edge. The second example problem uses a numerical boundary element method to verify the stresses away from the hole edge. The two example problems validate (a) the derived stress functions (ψ and ϕ), (b) the calculation of the polar stresses from the stress functions, and (c) the rotation of polar stresses into cartesian coordinates.

6.3.2 Example Problem 1 Description

This section compares the derived theoretical solutions for the tangential stress on the hole face with the example presented by Savin [14]. The beam geometry is given in Fig. (6-1) with :

- $c = \frac{1}{4}l$;
- $l = 10h$;
- $b = \frac{h}{4}$;
- $\frac{a}{b} = 3 : 1$;
- $d = 0$;

For these dimensions, the tangential stress on the hole face is [14] :

$$\sigma_{\theta} = \frac{Qh^2}{J(5 - 4 \cos 2\theta)} [0.5 \sin 4\theta - 7.5 \sin 3\theta + 7.25 \sin 2\theta + 15 \sin \theta] \quad (6.39)$$

The normalized stress $\frac{\sigma_{\theta}J}{Qh^2}$ from equation (6.39) is compared with the derived solution in Fig. (6-2) for polar angle $\theta = 0$ to 360° . The correlation between the two solutions is exact (to within computer round off error). The σ_{ρ} and $\tau_{\rho\theta}$ stress components are zero as expected in the derived solution.

Fig. (6-2) shows that the tangential stress on the hole edge is anti-symmetric with positive stresses indicating tension and negative stresses indicating compression. The anti-symmetric stresses are caused by the anti-symmetric loading at the beam center-line applied by direct longitudinal stresses and shear.

6.3.3 Example Problem 2 Description

The problem of section (6.3.2) does not fall within the infinite medium assumption, due to the fact that the smallest beam dimension (h) to largest hole dimension (a) has a ratio of 3 : 4 and does not fall into the 5 : 1 ratio required by the assumption in Savin's method. In order to verify the stresses away from the hole with the BEM method, a new problem with dimensions approaching an infinite domain is set up and solved by the BEM and derived solution method. The beam geometry is given in Fig. (6-1) with :

- $c = \frac{1}{2}l$;
- $l = 5h$;
- $b = \frac{h}{64}$;
- $\frac{a}{b} = 3 : 1$;
- $d = 0$;

This problem should fall well within the Savin infinite beam assumption since the ratio of minimum beam (h) to maximum hole (a) dimensions is 1:21.

6.3.4 Description of the BEM Model

The BEM uses a point collocation method to solve the weak form of the elastic differential equations. (For a full explanation of the BEM see, for example, Brebbia [3]). For stress concentration problems, the BEM has shown advantages over other numerical solutions (such as Finite Element and Finite Difference Methods) due to computational time saving both in pre-processing (meshing) and analysis [3]).

Fig. (6-3) shows the boundary element model. Three node quadratic interpolation elements are used on the boundary. The applied end loading is parabolic so that the end shear conditions in the beam are matched. The end conditions are not in exact accordance with the elasticity solutions since horizontal movement is prevented by rollers as opposed to the elasticity solution which only has prescribed displacements at the center point of the fixed end. To prevent singular stiffness matrices due to rigid body motion, the center node is pinned.

The convergence of the BEM method was studied by doubling the number of elements and checking stress differences at specific locations. The discretization chosen was such that successive doubling of elements only lead to a 2 % increase in accuracy. The comparison of stresses derived from the BEM to the proposed solution method for several horizontal locations are shown in Figures (6-4) to (6-6).

Figures (6-4) to (6-6), shows that the BEM solution begins to diverge from the derived solution near the fixed end ($x = 0$) of the beam due to the fact that the stress reflections off the boundary become dominant.

Both solutions show that the effect of the hole is localized and that the stress field approaches the “basic” beam stresses away from the hole. It must be noted that in some cases (especially the σ_x component) the small difference in the BEM results and theoretical results near the crack are due both to numerical inaccuracies in the BEM and by the difference in the position of stress sampling points.

This section has validated the derived analytical solution. The derived solution has proven to be accurate when the maximum hole dimension is significantly smaller than the the minimum beam dimension so that the “infinite” domain assumption holds.

6.3.5 Influence of a Horizontal Crack on the Global Strain Field in a Cantilever Beam

This section investigates the influence of a crack (or slit) on the global strain field. A horizontal crack or slit can be modelled by setting the vertical axis (b) of the elliptical hole to zero. For numerical modelling, the minor axis (b) cannot be set to zero since computational overflow occurs when trying to calculate the infinite stresses associated with the crack tip. In nature, perfect cracks are difficult to find since the infinite stresses cause blunting of the crack tip. Modelling of zero crack width also has the complication of interpenetration occurring in the compressive zone. Interpenetration cannot be handled by conventional classical elasticity nor is it likely to have significant effect on the global stress field and therefore strains away from the crack are not significantly effected. To avoid the numerical and interpenetration problems, the minor axis is set to 5 percent of the major axis. The 5 percent minor to major axis ratio is chosen since stresses at locations of three crack widths away from crack are effected by less than 2 % by any further decrease in the hole width

which is within the numerical accuracy of the BEM. Further decrease in hole width leads to increased solution time with no overall increase in numerical accuracy. This work does not deal with the possible frictional contact of the crack face after crack closure that can change the global stress field depending on degree of crack closure and frictional stress transfer.

6.4 Crack Detection by Fiber Optic Sensors

Recent advances in birefringence analysis [4] has proven the potential of integrated optic fiber sensing in detecting strain changes. Previous work [10] in fiber optic sensing has relied on the breaking of the optic fiber for actual crack detection. This method of crack detection only allows for point-wise crack detection since the fiber would have to pass close to a crack for the stresses to be sufficiently high to cause fiber rupture. Since in general applications, the position of a crack is not known *a priori*, the point-wise crack detection method could only be successful by introducing a large number of sensors into the sensing domain which in turn made the structure weaker and expensive to manufacture. Integrated sensing techniques measure the total strain associated with crack presence and fidelity of the sensing system is dependent on the changes in global strain fields integrated along the length of the fiber.

The success of a damage detection technique is characterized by its reliability in detecting both the extent and position of the damage. In all damage detection techniques, the reliability of the system is also influenced by the position of detector. In two-dimensional damage detection problems, the four parameters that can be varied are :

- Longitudinal position of the crack (c).
- Vertical Position of the crack (d).

- Crack Length (2a).
- Sensor position (f).

With increasing crack length, the size of the K (stress singularity) dominant zone increases causing a larger strain influence zone. An increasing strain influence zone in turn leads to better detection reliability. Since the effect of crack length is known to give increased reliability, the effect of crack position on sensor system reliability is investigated independently of crack length.

6.4.1 Interferometric Optic Sensors

Interferometric optic sensors rely on axial fiber strain to cause a change in the fiber length and a subsequent interference of the input light field due to the increased light traveling time. This integrated technique is unlikely to work in delamination detection since the axial strains caused by the presence of a delamination crack is anti-symmetric as seen in Figure (6-4). Antisymmetric axial strain causes the increase in fiber length due to tensile strains to be offset by the decrease in fiber length due to compressive strains and thus the overall length in the fiber remains unchanged. No change in overall fiber length means that no interference takes place since the light travelling time remains constant.

6.4.2 Bragg Grating Sensors

Bragg grating sensors allow for point wise longitudinal strain sensing by monitoring the time taken for backscattered light to move through an etched grating along a small portion (approximately 5 mm) of the fiber length. The advantage of this type of sensor over traditional point sensors is that several Bragg grating can be etched onto each fiber. It must be noted that this type of fiber sensor system although being more reliable than traditional point sensors, is less reliable than integrated sensors (such as birefringent sensors) since the position of the gratings relative to the occurring damage greatly effects sensor system reliability.

6.4.3 Birefringent Optic Sensors

Optical birefringence refers to a light polarization phenomena and subsequent electric power loss due to the rotation of the fiber's optical axis along the fiber length. Figure (6-7 a) shows a general state of stress along any fiber cross-section in the y-z plane. The initial (unstrained) polarization axes are marked by labels y and z. The strained polarization axes are marked y' and z'. The degree of birefringence and subsequent power loss depends on the degree of rotation between strained and unstrained axes. By rotation into the principal axes, any state of stress (or strain) can be decomposed into purely dilatational strains (marked with a subscript I) as shown in Figure (6-7 b) and distortional strains (marked with a subscript D) as shown in Figure (6-7 c). The dilatational component of strain causes a pure volume change with no change in shape since the unstrained polarization axes remain the same through pure dilatational strains. Distortional strains causes a change in shape as shown by rotation of the polarization axes from y to y' and z to z' in Figure (6-7 c). Hence rotation of the fiber axis and subsequent power loss can only be caused by a shape change of the fiber cross-section as caused by distortional strains while dilatational strains cause no birefringent behaviour.

Previous work on photoelastic sensing [15] has analyzed the sensitivity of generally strained fiber optic sensors. In a general anisotropic photoelastic material, the phase difference between any two eigenmodes ($\Delta\phi$) and hence fiber sensitivity is given by :

$$\Delta\phi = f\left[\int_l \delta\epsilon \, dx\right] \quad (6.40)$$

where :

f is a scalar photoelastic operator.

We define the sensitivity to be $\delta\epsilon$ which is the strain difference between the unstrained and strained case, and ϵ is the generalized three dimensional strain tensor.

In the case of damage detection, $\delta\epsilon$ refers to the difference between the basic (or un-weakened) solid body and the damaged solid body. Note that for birefringent

fiber, $\delta\epsilon$ is always positive since shifting of the optical axis in any symmetric direction has equal effect on the power loss.

The aim of this section is to determine the effect of crack and sensor position on the sensitivity components in equation (6.40).

6.4.4 Integral Strain Field Mapping

In order to maximize each sensitivity component of equation (6.40), the line-integral strain deviation (along the optical fiber) between weakened (cracked) and the basic (uncracked) stress state is studied for various crack and sensor position. Fig. (6-8) to (6-10) show the various sensitivity band plots for a typical fiber position ($f = 0.1$ h). The sensitivity maps are generated by the following method :

1. Fix sensor position at a vertical height f .
2. Fix crack position (c and d).
3. Calculate the basic stresses (σ_o) for the un-weakened beam using equation (6.16) along line f .
4. Calculate the basic strain field (ϵ_o) from the basic stresses using equation (6.38).
5. Calculate the weakened beam stresses using the method developed in section (6.2) at the strain sensor position f .
6. Calculate the weakened beam strains using equation (6.38).
7. Find the difference between the basic and un-weakened strain states $\delta\epsilon$.
8. Calculate the sensitivity ($\int_l \delta\epsilon \, dx$) for each strain component ϵ_x , ϵ_y , ϵ_{xy} at position f .
9. Change crack position and repeat step (3) to (8).
10. Change strain sensing position and repeat steps (2) to (9).

Here it is assumed that the damage can occur at any position within the beam. Since the problem is symmetric (with respect to absolute strains) about the beam center-line (which is assumed to be the neutral axis in this case), one half of the beam is studied with symmetric distribution of fiber sensors about the beam center-line being understood. The typical case that is studied is for the following beam configuration :

- $\frac{l}{h} = 20 : 3;$
- $\frac{a}{h} = 1 : 60;$

6.4.5 Interpretations of the Integral Strain Field Maps

The band plots for typical strain sensing positions Fig. (6-8) to (6-10) show that for any fixed strain sensing position, the longitudinal position of the crack (c) has little effect on the overall strain sensing capability of the sensor. Restated this means that for a fixed loading condition, the strain sensor is incapable of detecting the horizontal position of the damage. This in turn means that the two crack position parameters (c and d) are only weakly coupled. Due to the assumptions of the infinite beam, The maximum sensitivity occurs when the crack is at the sensor position ($d = 0.1 h$ in Fig. (6-8) to (6-10)) and decreases with vertical distance from the fiber position.

At any position in the beam the crack is being subjected to predominantly Mode II (shear) and since the shear stress is constant along horizontal sections of the beam, the effect on the global strain field in the beam is basically the same. Along any vertical section (y), the shear strain field varies parabolically and hence the effect of changing vertical crack position (d) should be detectable.

The sensitivity of the fiber is dependent on both crack and fiber position. Since the crack can occur at any position along the beam but the position of the fiber is controllable, it is the objective of the designer to ensure that the chosen sensor position gives the most reliable sensing ability for any crack position. For a particular crack position, the fiber sensitivity is given by the strain deviation integral along the

sensor. Allowing the crack to occur at any position in the beam, the total reliability of the sensor system is given by summing the contribution of each individual sensitivities over the entire area of the beam.

Hence reliability ($\Delta\epsilon$) is given by the area integral of the sensitivity integral($\int_l \delta\epsilon dx$):

$$\Delta\epsilon = \int_A [\int_l \delta\epsilon dx] dA \quad (6.41)$$

Figure (6-11) shows the unit normalized area integral ($|\Delta\epsilon|$) of the strain maps for various sensing position and strain components. All reliability components ($|\Delta\epsilon|$) show increasing values with distance from the beam center-line. It must be noted that increasing shear strain contribution is due to the the infinite boundary condition assumption since near the top free face both the weakened and basic stress states should approach zero and hence there should be zero sensitivity at this fiber position. The effect of boundary conditions are studied in the next section. The theoretical solution cannot be considered accurate for fiber sensing positions $f/h > 0.8$ since the assumption of infinite boundary conditions is violated as discussed in section 6.2.

6.4.6 Effects of Finite Boundary Conditions

The previous section has shown that the two position coordinates of the crack are essentially independent. This in turn means that further studies can be performed by varying the height of the crack alone (at a fixed longitudinal crack position c). This section studies the effect on strain sensing reliability of varying the length and y position (d) of the crack by the BEM.

Effects of finite beam depth

The theoretical solution derived in section 6.2 is only valid when the length of the crack is 10 times smaller than the distance of the crack from the horizontal boundary ($h-d$) [12]. The BEM does not restrict the position of the crack and this section studies the effect of finite beam depth by comparing the sensor reliability as calculated by the theoretical and BEM methods as the position of the crack approaches the beams

upper surface. The beam dimensions are as previously used and with the crack at midspan ($c = 1/2$). A comparison of the normalized reliability by the theoretical and BEM methods are presented in Figures (6-12) to (6-14). The BEM results are consistent with the theoretical results for the normal strain components ($\Delta\epsilon_x$ and $\Delta\epsilon_y$). As expected, the BEM shear strain components ($\Delta\epsilon_{xy}$) approaches zero as the fiber position approaches the free surface ($f = h$). The BEM results also show increasing fiber sensitivity with distance away from the beam center-line the normal strain components ($\Delta\epsilon_x$ and $\Delta\epsilon_y$) when $f/h < 0.8$. The BEM results show a decrease in sensitivity in normal strain components for fiber positions greater than $f/h = 0.8$ and hence with respect to normal strain components the maximum sensitivity is when the fiber is placed at 80 % of the beam height. The effects of finite beam width are shown in Figures (6-12) and (6-13) for $f/h > 0.8$ since the BEM solutions show a decrease in sensor system sensitivity while the theoretical solutions continue to show an increase.

Effects of crack length

For the same beam dimensions as previously used and with the crack at the beam midpoint ($c = 1/2$ and $d = 0$), the BEM is used to study the effects of increasing crack length on fiber reliability. The fiber is placed at $f = 0.8 h$ which from the previous analysis is the most reliable position for normal strain component sensing (see section 6.4.6) . Figure (6-15) shows that as proposed in section (6.4), sensing reliability increases with increasing crack length.

6.5 Case Studies

This section deals with two possible applications of fiber optic sensors in civil and aerospace applications by studying the feasibility of their application in concrete and composite structures. Existing point sensors (interferometric and Bragg) rely on detecting longitudinal (ϵ_x) strains. Existing integrated sensors rely on detecting transverse (ϵ_y) strains by polarization. Calero et al. [4] have shown that the sensitivity

of birefringent fiber sensors is dependent on :

- Sensitivity of optical equipment.
- Optical properties of the fiber.
- Stiffness of the plastic fiber jacket which effects the transmissibility of strains to the glass core.

Kersey et al. [6] have shown that the sensitivity of point sensors can be as high as $1\mu\epsilon$ while integrated sensors require transverse strains greater than $5\mu\epsilon$ (un-jacketed) and greater than $400\mu\epsilon$ with soft jacket (Calero et al. [4]) acting over a length of 152 mm. In advanced plastic matrix composites, the fiber can be stripped of its jacket, and transverse strain sensitivity of $5\mu\epsilon$ acting over a sensing length of 152 mm can be realized. Calero et al.'s [4] finding indicate integral sensing capabilities of :

- Un-jacketed fiber with $5\mu\epsilon$ acting over $152mm = 760\mu\epsilon mm$.
- Jacketed fiber with $400\mu\epsilon$ acting over $152mm = 60800\mu\epsilon mm$.

In concrete structures, the jacket is needed to protect the glass from chemical embrittlement and failure.

This section studies the feasibility of using both the point and integrated sensing schemes for the two applications mentioned above.

6.5.1 Case Study 1. Delamination Detection in $[0_m/\pm 45_n/90_k]_s$ Advanced Composite Laminates.

General advanced composite laminates used in the aerospace industry can be orthotropic. In order to use the elastic isotropic sensing detection theory developed above, strictly only quasi-isotropic laminates can be considered. However, in this analysis we release the strictly isotropic assumption and consider quasi-isotropic and nearly quasi-isotropic laminates. Section (6.4.6) has shown that normal-strain sensor

reliability increases with increasing distance away from the beam center-line. Since all strain-sensing reliability calculations in previous sections are normalized by the load to elastic modulus ratio (Q/E), greater sensitivity is achieved by increasing the applied load (Q) and decreasing the elastic modulus (E) of the material. During damage inspection, the goal is to maximize the applied load in order to increase the strain (and hence detection ability) in the fiber but to prevent any damage to the aircraft component during inspection. In this analysis, the applied load (Q) is set to 40 % of first ply failure (FPF) which is less than the load that causes first damage to the laminate by a factor of 2.5 (typical for civil structures) during aircraft inspection. E is set for the particular composite stacking sequence and material properties. The position of the fiber is chosen to be at 80 % of the beam height since from Figures (6-12 and 6-13) this is the most reliable sensing position. The crack is placed on the center-line ($d = 0$) since this is the furthest location from the given fiber position hence giving the minimum sensitivity and thus tests the possibility of crack detection to the extreme.

Beam Elastic Modulus and Applied Load

The typical composite that is studied in this section is the T300/5208 $[0_m/\pm 45_n/90_k]_s$ quasi-isotropic laminate. The composite ply is assumed to have the following properties (taken from Tsai [18]):

- Longitudinal elastic ply modulus (E_l) = 181 GPa.
- Transverse elastic ply modulus (E_t) = 10.3 GPa.
- In-plane shear modulus (G_{lt}) = 7.2 GPa.
- In plane Poison ratio (ν_{lt}) = 0.28.
- Out of plane elastic modulus (E_z) = 10.30 GPa.

- Out of plane Poisson ratio (ν_{tz}) = 0.28;
- Ply thickness (t) = 0.125 mm.
- Maximum longitudinal tensile ply strength (X) = 1500 MPa.
- Maximum transverse tensile ply strength (Y) = 60 MPa.
- Maximum shear strength (S) = 68 MPa.

The laminate is assumed to have $m + 2n + k = 100$ with $m > 20$. The schematic layout and coordinate system used in further analysis are presented in Figure (6-16). The stresses in any ply ($k = 2$ to $n-1$) are given by the Lekhnitskii solution [8] for the bending of a cantilever subject to tip load Q :

$$\sigma_x^{(k)} = \frac{6E_1^{(k)}Qx}{hS}(S_2 - 2S_1y) \quad (6.42)$$

$$\sigma_y^{(k)} = 0 \quad (6.43)$$

$$\begin{aligned} \tau_{xy}^{(k)} = \frac{6P}{hS} & \left(S_1 \left(\sum_{i=1}^{k-1} (b_i^2 - b_{i-1}^2) E_1^{(k)} + (y^2 - b_{k-1}^2) E_1^{(k)} \right) \right. \\ & \left. - S_2 \left(\sum_{i=1}^{k-1} (b_i - b_{i-1}) E_1^{(k)} + (y - b_{k-1}) E_1^{(k)} \right) \right) \end{aligned} \quad (6.44)$$

The engineering flexural elastic modulus for each ply $E_1^{(k)}$ is calculated using standard tensor transformations where for ply (k) with fiber orientation ($\theta^{(k)}$) :

$$E_1^{(k)} = Q_{11}c^4 + 2(Q_{12} + Q_{66})s^2c^2 + Q_{22}s^4 \quad (6.45)$$

$$Q_{11} = \frac{E_l}{1 - \nu_{lt}^2 E_t / E_l};$$

$$Q_{12} = \frac{\nu_{lt} E_t}{1 - \nu_{lt}^2 E_t / E_l};$$

$$Q_{22} = \frac{E_t}{1 - \nu_{lt}^2 E_t / E_l};$$

$$Q_{66} = G_{lt}$$

$$s = \sin \theta^{(k)}$$

$$c = \cos \theta^{(k)}$$

also :

$$\begin{aligned}
S_1 &= \sum_{k=1}^n (b_k - b_{k-1}) E_1^{(k)} \\
S_2 &= \sum_{k=1}^n (b_k^2 - b_{k-1}^2) E_1^{(k)} \\
S_3 &= \sum_{k=1}^n (b_k^3 - b_{k-1}^3) E_1^{(k)} \\
S &= 4S_1 S_3 - 3S_2^2
\end{aligned} \tag{6.46}$$

The engineering elastic modulus (E_o^f) is given by :

$$E_o^f = \frac{S}{S_1(2h)^2} \tag{6.47}$$

Tsai [18] has found that for long beams (with span-to-depth ratios greater than five), the interlaminar shear stresses did not effect the overall FPF load of the composite which occurred at the outer laminate fiber. Constraining the span to equal 5 times the thickness of the laminate, the FPF load can be calculated using the maximum stress criterion :

$$\begin{aligned}
Q_{FPF}^x &= \frac{X}{\sigma_x c^2} \\
Q_{FPF}^y &= \frac{Y}{\sigma_x s^2} \\
Q_{FPF}^{xy} &= \frac{S}{\tau_{xy}(c^2 - s^2)} \\
Q_{FPF} &= \min[Q_{FPF}^x \mid Q_{FPF}^y \mid Q_{FPF}^{xy}]
\end{aligned} \tag{6.48}$$

$$Q_{FPF} = \min[Q_{FPF}^x \mid Q_{FPF}^y \mid Q_{FPF}^{xy}] \tag{6.49}$$

The stress (σ_i) is calculated using a unit load in each ply and is then rotated into the individual ply coordinate system. The maximum ply stress for each of the stress components is then used to calculate the first ply failure load Q_{FPF}^i for each ply. The applied load Q is set to 40 % of Q_{FPF} which is the minimum of the ply failure load components Q_{FPF}^i . Figure (6-17) shows the variation of Q for various numbers of m and n, as expected the applied load Q increases for increasing numbers of m and increases with increasing n (for a fixed m). Figure (6-18) shows the variation of elastic

modulus E_f^o for various numbers of m and n, as expected the engineering laminate modulus E increases for increasing numbers of m and increases with increasing n (for a fixed m). Figure (6-19) shows the variation of the Q/E ratio for various m in the $[0_m/\pm 45_n/90_k]_s$ composite. It must be noted that since the failure mechanism is dominated by the transverse tension in the 45° layers, the Q/E ratio is the same for all n and is hence only dependent on m. In order to study the worst case, the smallest Q/E ratio (m = 20) laminates are studied.

The BEM method is used to study the effect of crack length on strain deviation for the $[m/n/k]_s = [20/30/50]_s$ laminate (engineering elastic modulus is $E_e = 111.2GPa$, $Q = 101kN$ and orthotropy ratio $E_{11}/E_{22} = 0.6$). It must be noted that though this laminate is probably too soft for real-world engineering application, it is presented here as giving the worse case results with respect to crack detection. The effect of increasing crack length on absolute normal strain difference (basic to weakened) is plotted for various crack lengths in Figures (6-20) and (6-21) for the crack at the center of the beam ($c = 62.5$ mm and $d = 0$) and the fiber at $f = 0.8$ h = 10 mm.

Interpretation of Results

The strain deviation shown in Figure (6-20) indicates that crack lengths of the order of 0.25 mm can be detected by existing axial point sensing techniques with maximum axial strain deviation being $20\mu\epsilon$ for ϵ_x which is within the $1\mu\epsilon$ sensing range given by Kersey [6]. For transverse strain sensing, cracks equal and greater than 0.25 mm are needed in order that the sensitivity ($\int_l \delta\epsilon$) falls within the sensitivity range of $76\mu\epsilon cm$ sensing range of the Calero [4] sensing fiber. The accurate strain readings possible by point-wise sensors indicate that smaller damage zones can be detected, though these reading cannot be assumed to be reliable since they fall into the range of strains that can be caused by secondary mechanical effects such as creep and thermal strains. For example, though point axial sensors can detect strain of the magnitude of $1\mu\epsilon$ [6], a temperature differences of $0.5^\circ C$ can cause axial strains of the order of $5\mu\epsilon$ for the $[0_{20}/\pm 45_{15}/90_{50}]_s$ composite studied above which indicates that parasitic thermal

strains can effect the interpretation of the results for small delamination lengths.

As previously stated the proposed sensing technique can only detect the y-axis location of the damage with both other geometric parameters (x-axis position and damage length) being essentially independent. A possible way to overcome this problem is the introduction of a moving load along the x-axis of the beam. As the moving load passes the crack position, the shear stresses at the crack position falls to zero and the crack becomes essentially unloaded. Figure (6-22) shows the influence line for the integral strain deviation when the fiber is at 0.8 h above the neutral axis and the crack is at the center of the beam ($d = 0$, and $c = 1/2$). Figure (6-22) is normalized by the Calero unjacketed polarized fiber sensor sensitivity of $5\mu\epsilon$ over a 152 mm sensing range, so that sensitivity greater than 1 indicates a detectable crack.

As expected the strain deviation is zero before the load passes the crack (line A) and is unchanged when the load passes the crack (line B). The exact center of the crack is marked by a peak in the influence line which is 10 % above the load-at-tip position. The peak in the strain integral ($\Delta\epsilon$) influence diagram (Figure (6-22)) is attributed to the interference of the crack with the stresses under the point load. Figure (6-23) shows the characteristic stress intensity under the point load for the basic (uncracked) beam. The influence of the crack on the point load stress distribution can be shown by plotting the stress difference between basic and weakened beams as shown in Figure (6-24). The relatively large effect of the crack on the point load stress distribution near the point load causes the peak in the strain integral influence diagram.

Figure (6-25) shows the effect of increasing crack height (d) from the center-line on sensor reliability. As expected the constant post-peak behaviour (line B) increases with increasing crack height (d) due to the decreasing distance ($f-d$) between the sensor and crack. The relative increase in peak to post peak strain integral ($\Delta\epsilon$) from 10 % ($d = 0$) to 300 % ($d = 0.6 h$) is attributed to the increasing influence of the crack on the point-load stress distribution as the distance between the point load and crack

decreases. Previously the post-peak strain integral (line B) was used to locate the vertical position (d) of the crack. The increasing peak in the strain integral influence diagram has the added advantage that it not only locates the center of the crack but also gives an independent indication of the height (d) of the crack.

Figure (6-26) shows the effect of increasing crack length on the strain integral influence diagram. As expected from previous results the post peak strain integral (lines marked B) increases with increasing crack length. The length of zero strain integral (pre-peak line strain integral marked A) to post-peak strain integral (lines B) increases with increasing crack length giving a rough indication of the crack length. Figure (6-26) shows that crack length can be deduced by considering both the post-peak sensor strain integral and the distance between post and pre-peak reliability. Comparing the peak to post peak sensitivity, Figure (6-26) shows that the peak in the influence line diagram should be detectable by the Calero sensor for crack lengths (2a) of 4 mm, since the difference in peak to post-peak sensitivity is greater than 1, where values greater than 1 indicates sensitivity within the sensing range.

The proposed loading scheme can also be effectively used to detect the presence of multiple cracks. Since it has been shown that reliability of the sensor is solely dependant on shear stress, linear superposition can be used to detect the presence of non interfering cracks. Figure (6-27) shows the sensitivity influence line for the composite cantilever beam with two cracks at $x = 31.25$ mm ($c_1 = l/4$) and $x = 93.75$ mm ($c_2 = 3l/4$). Both cracks are on the beam center-line ($d = 0$ mm) and the half crack length (a) is 1 mm. For point load positions near the tip of the beam (as x approaches $l = 125$ mm), the sensitivity is twice the sensitivity calculated in the single crack case (see figure (6-22)). As the point load passes the influence zone of the first crack, the influence line becomes the same as in the single crack case of figure (6-22). The position of crack centers can again be determined by the peaks in the influence line diagram.

6.5.2 Implications

Traditional non-destructive evaluation techniques such as x-ray and CATSCAN detection require expensive, sophisticated equipment which is only capable of detecting damage over a small area. Previously used fiber-optic sensor techniques are only able to detect the presence of damage but are incapable of quantifying position, extent or number of damaged zones. This section has shown that one relatively simple moving load test can be used to both detect the presence of delamination damage and to quantify all needed sensing parameters which include (1) crack position, (2) length, and (3) number of cracks. Reinforced concrete structures are often subjected to moving point load tests which are applied by driving heavy trucks over the tested structural member. For aerospace structures, a simple loading test can be devised as shown in Figure (6-28), which consists of moving a wheel with the required test load by means of an over-head crane. Interpretation of the moving point load test is relatively simple with a single continuous measurement of light power intensity (for birefringent sensors) or interference (for interferometric point sensors) giving all required sensing parameters. Furthermore, the nature of fiber optic sensors allows for detection over a large area which overcomes the problems of traditional non-destructive evaluation techniques.

6.5.3 Case Study 2. Delamination study in Reinforced Concrete Beams

This section checks the feasibility of using fiber optic sensors for detection of debonding damage along the reinforcement or between concrete overlays in typical reinforced concrete beams. Since debonding damage occurs primarily at the steel reinforcement (or at overlays), practical positioning of the optic fiber sensor would be near the position of the damage for greatest reliability. Figure (6-29) shows the typical reinforced concrete cross-section to be investigated. The tip load is constrained to give a maximum deflection of $l/200$ where the length of the beam l is taken to be 4 meters. Using the ACI [1] Code we find the maximum allowable tip load = 18 kN. Under

these conditions, the equivalent elastic constants are :

- Longitudinal elastic modulus $E_1 = 13GPa$
- Transverse elastic modulus $E_2 = 24GPa$
- Poisson ratio = 0.3

Figure (6-30) shows the schematic representation of the concrete beam layout. The crack position is on the center-line at midspan ($c = 2$ m). The fiber sensor is placed at $f = 0.152$ m with the delamination occurring at $d = 0.162$ m which is assumed to be the position of the top steel. Figures (6-31) and (6-32) show the sensitivity components for various crack lengths. For transverse polarized sensing, stiff jacket fiber sensors can be used to detect delamination lengths of 0.2 meters (total sensitivity equal to $1300\mu\epsilon$ mm which is greater than the required $720\mu\epsilon$ mm for the Calero un-jacketed sensor [4])). The sensitivity lies outside the sensing range of current soft jacket sensing polarized fibers for practical delamination lengths which requires sensitivities of $60800\mu\epsilon$ mm. Longitudinal point sensors (such as Bragg grating sensors) can be used to reliably detect delamination lengths of 0.2 meters. The moving load test can be used to detect crack lengths in a similar way as described in section (6.5.1). Since concrete structures typically occur with simply-supported spans, the sensitivity influence diagram is calculated for a simply-supported span. Figure (6-33) shows the influence diagram for a simply-supported span with fiber at $f = 0.8$ h and the crack at midspan and $d = 0.152$ m. With the same concrete layout, the simply supported beam length is increased to 12 meters (which is a typical free length for reinforced concrete members) with the load being unchanged. As expected from the previous work, the influence diagram closely resembles the influence diagram for the shear stress of the midpoint of a simply supported beam except for the peak occurring when the load crosses the center of the crack which is once again attributed to point-load stress distribution interference. Note that the normalizing parameter in Figure (6-33) is for the Calero un-jacketed fiber sensor which implies that a stiff jacket sensor needs to be used for birefringent sensing. The peak value of 2.5 exceeds

the pre-peak value of 1.5 by 1 which indicates that the peak (and hence approximate crack position) in the influence diagram should be easily distinguishable from the pre-peak value with the Calero stiff-jacket sensor.

This section has shown that fiber-optic sensors can be effectively used to find all the sensing parameters required to characterize reinforcement debonding damage in concrete structures. A simple moving load test can be used to determine (a) the horizontal location, (b) the severity (length) and (c) the vertical location of the debonded region. As shown in section (6.5.1), the method can be simply extended to include the detection of multiple debonded regions by the use of superposition.

Bibliography

- [1] *ACI design handbook*. (ACI, Detroit). 1991.
- [2] D. Allaei. *Smart aircraft by continuous condition monitoring of aircraft structures and components*. 2nd European Conference on smart structures and materials. (Glasgow, UK). 152-155.
- [3] C. A. Brebbia. *The boundary element method for engineers*. (Wiley, New York) (1978).
- [4] J. Calero, S. P. Wu, C. Pope, S. L. Chuang, J. P. Murtha. *Theory and Experiment on Birefringent Optical Fibers Embedded in Concrete Structures*. *J. of Light. Tech.* **12**. 1081-1090. (1994)
- [5] S. Girshovich, T. Gottesman, H. Rosenthal, E. Drukker and Y. Steinberg. *Impact damage assessment of composites*. *Damage Detection in Composite Materials*. ASTM STP 1128. 183-199.
- [6] A. D. Kersey, T. A. Berkoff and W. W. Morey. *Multiplexed fiber Bragg grating strain-sensor system with a fiber Fabry-Perot wavelength filter*. *Opt. Lett.* **18**. 1370-1375. (1993).
- [7] E. Kreyszig. *Advanced engineering mathematics*. (Wiley, New York) (1993).
- [8] S. G. Lekhnitskii. *Anisotropic plates*. (Gordon and Breach, New York) (1968).
- [9] K. I. McRae, A. G. McCray, A. J. Russell and C. P. Bowers. *Ultrasonic imaging of delamination damage around fastener holes in graphite/epoxy composite*. *Damage Detection in Composite Materials*. ASTM STP 1128. 163-179.

- [10] R. M. Measures. *Progress Towards Fiber Optic Smart Structures at UTIAS*. Proceedings: Fiber Optic Smart Structures and Skins III. (San Jose). SPIE vol. 1370. 46-68. (1990).
- [11] R. M. Measures, N. D. W. Glossop, J. Lymer, M. Leblanc, J. West, S. Dubois, W. Tsaw and R. C. Tennyson. *Structurally integrated fiber optic damage assessment system for composite materials*. *Applies Optics*. **28**. 2626-2633.
- [12] N.I. Muskhelishvili. *Some basic problems of the mathematical theory of elasticity*. (Noordhoff, Gronigen) (1953)
- [13] T. K. O'Brien. *Delamination, durability and damage tolerance of laminated composite materials*. Computational methods for failure analysis and life prediction. (Hampton). 311-312. (1993).
- [14] G. N. Savin. *Stress concentration around holes*. (Pergamon Press, New York) (1961).
- [15] J. S. Sirkis. *Phase-strain-temperature model for structurally embedded interferometric optical fiber strain sensors with applications*. Proceedings: Fiber Optic Smart Structures and Skins IV. (Boston). SPIE vol. 1588. 26-43. (1991).
- [16] K. Talat. *Smart skins and fiber-optic sensors application and issues*. Proceedings: Fiber Optic Smart Structures and Skins III. (Bellingham). 103-114. (1990).
- [17] S.P Timoshenko and J. N. Goodier. *Theory of elasticity*. (McGraw-Hill, New York) (1970).
- [18] S. W. Tsai. *Composites Design*. (Think Composites, Dayton) (1988)

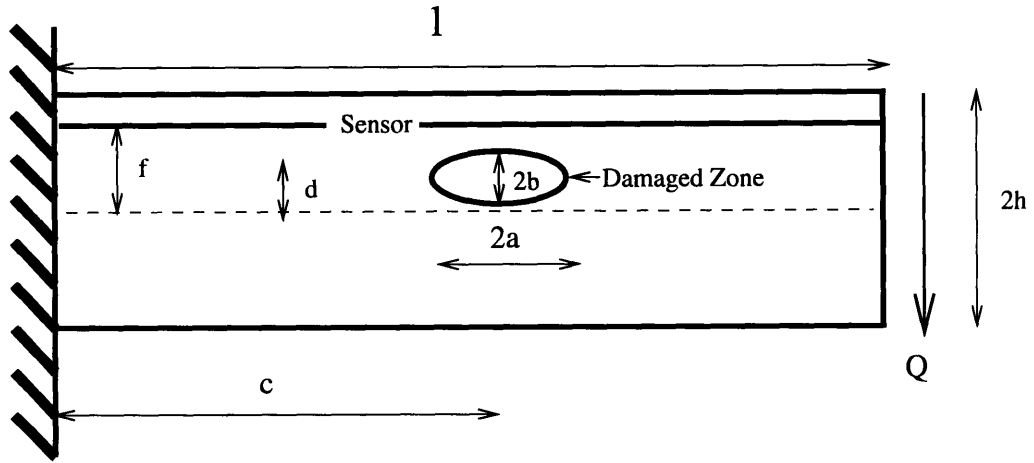


Figure 6-1: Physical elasticity model of weakened cantilever beam.

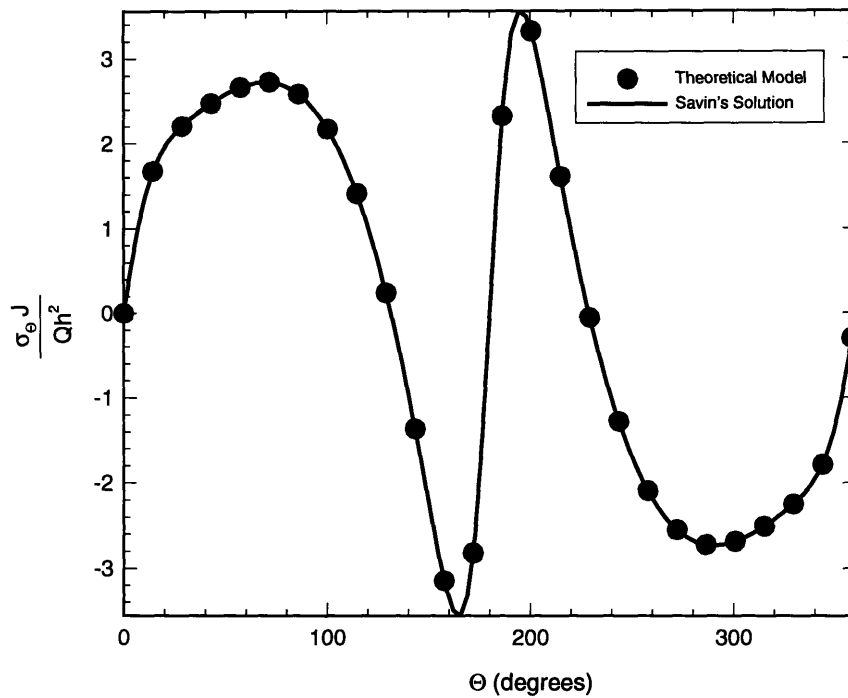


Figure 6-2: Comparison of derived theoretical solution with Savin's solution for the normalized tangential Stress $\frac{\sigma_{\theta} J}{Q h^2}$ on the hole edge.

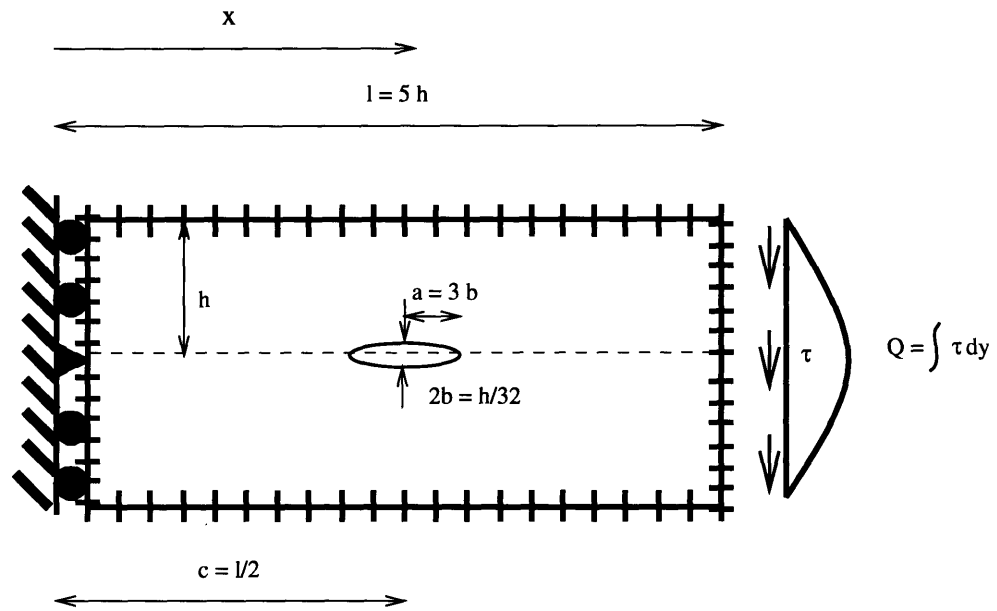


Figure 6-3: Boundary Element Model of weakened cantilever beam.

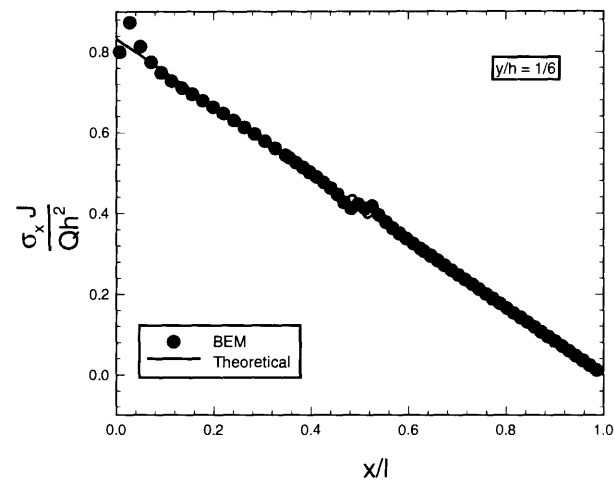
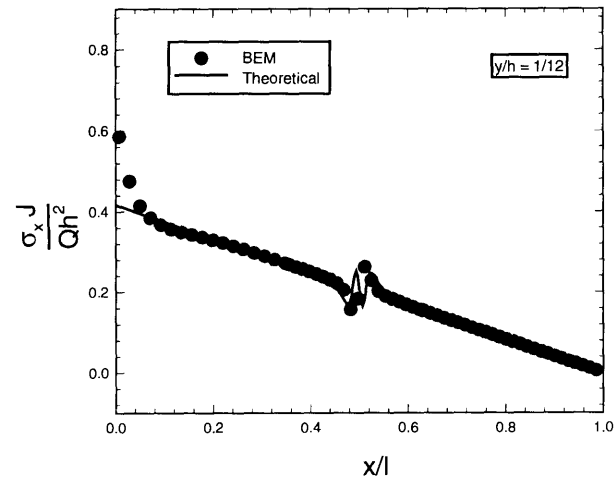
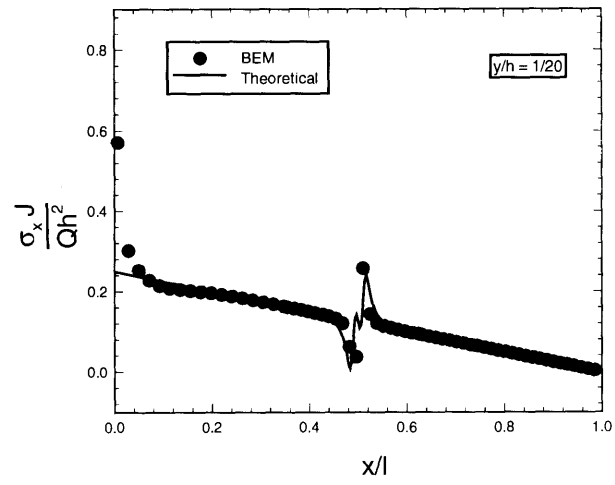


Figure 6-4: Comparison of BEM and theoretical solutions (σ_x) at various distances from the elliptic hole.

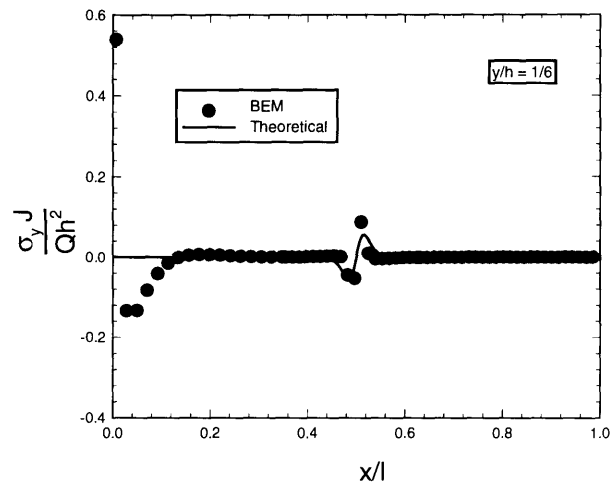
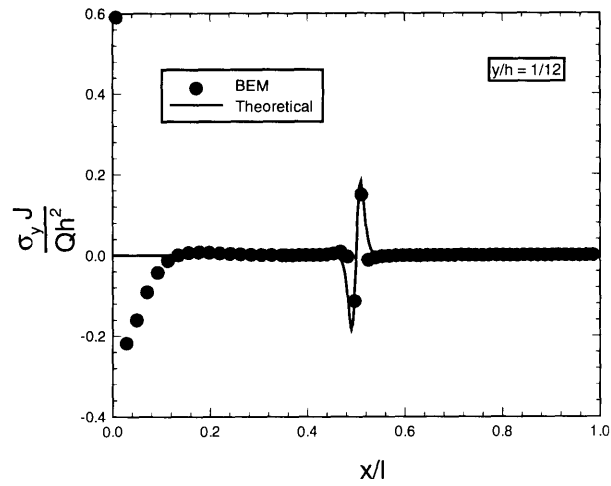
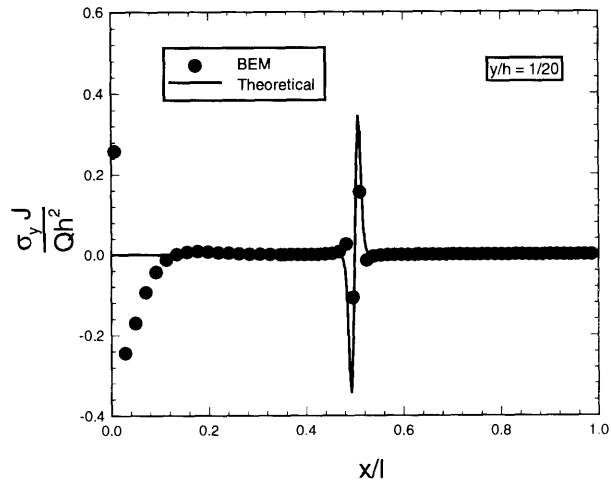


Figure 6-5: Comparison of BEM and theoretical solutions (σ_y) at various distances from the elliptic hole.

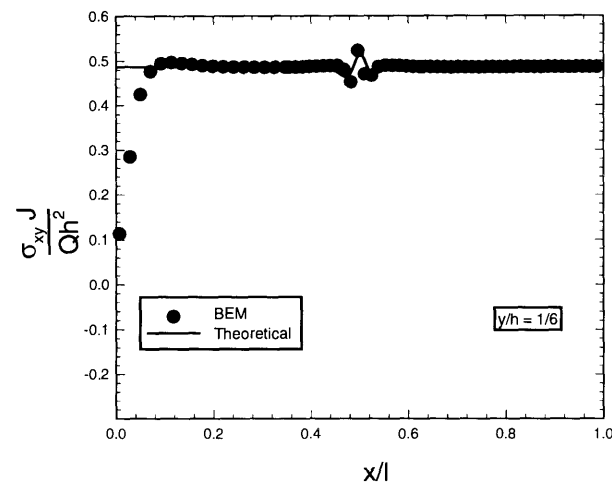
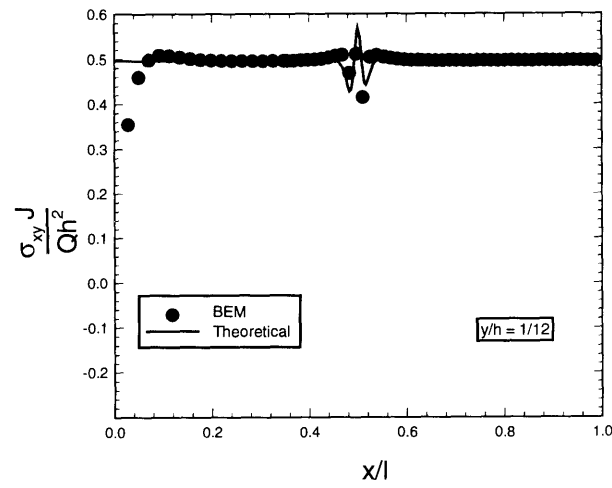
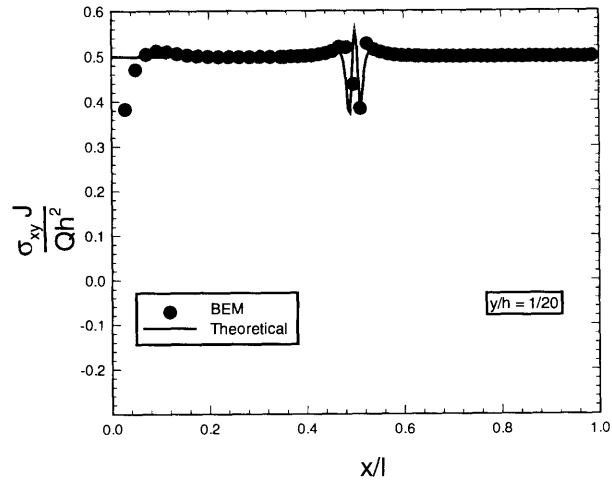


Figure 6-6: Comparison of BEM and theoretical solutions (σ_{xy}) at various distances from the elliptic hole.

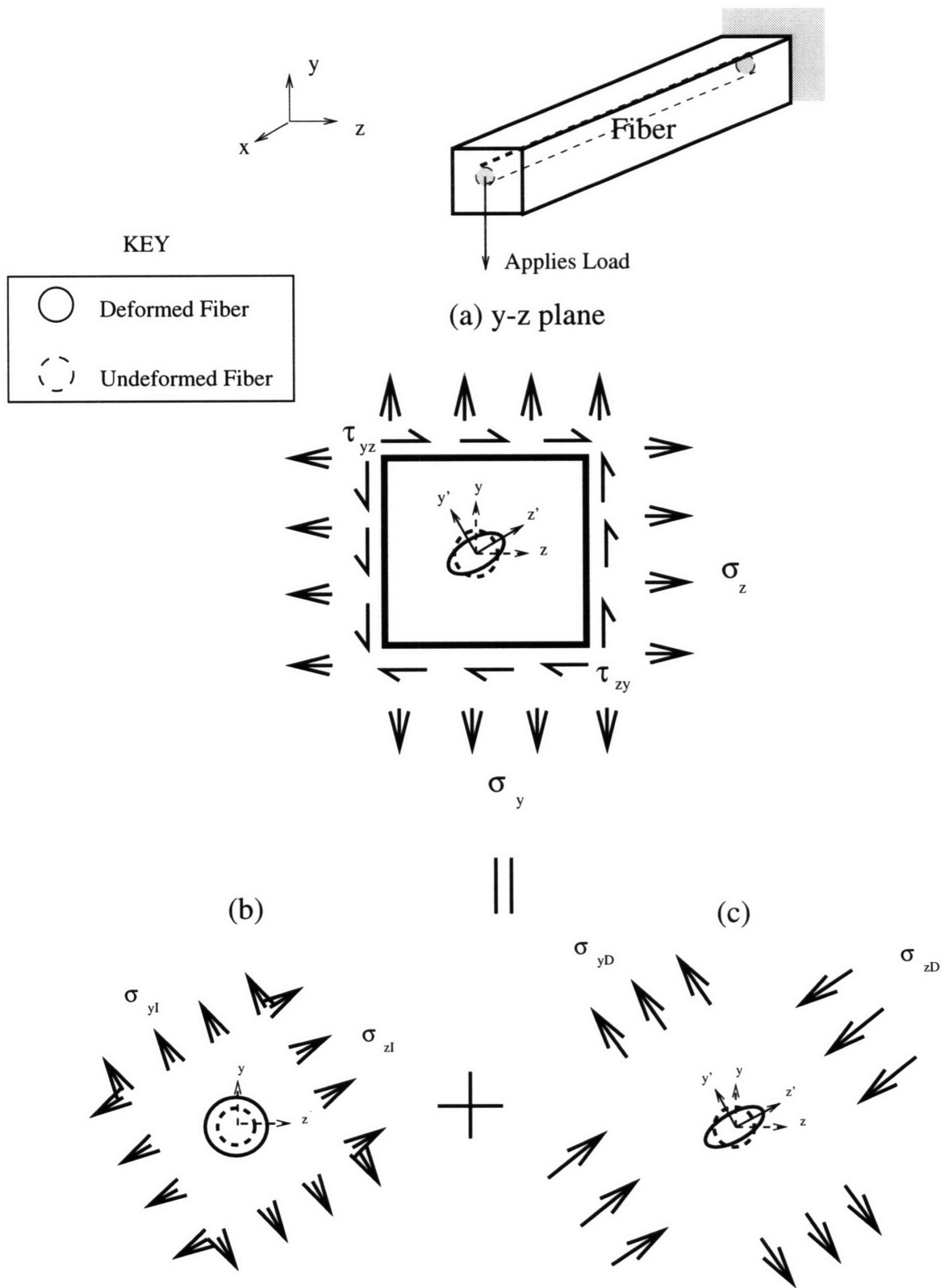


Figure 6-7: Rotation of Birefringent axes due to applied stress.

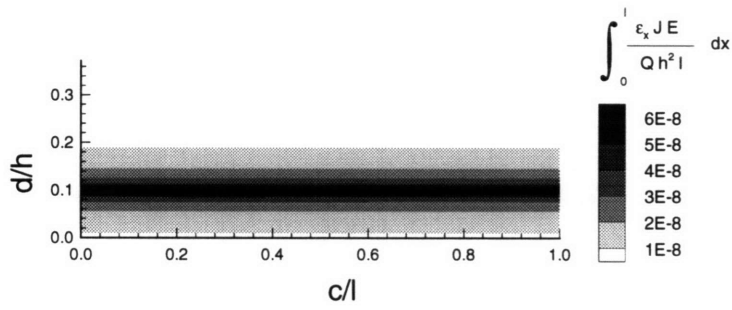


Figure 6-8: ϵ_x Sensitivity map at sensor position $f/h = 0.1$

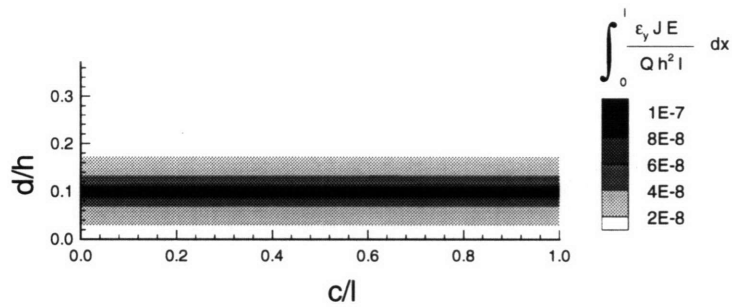


Figure 6-9: ϵ_y Sensitivity map at sensor position $f/h = 0.1$

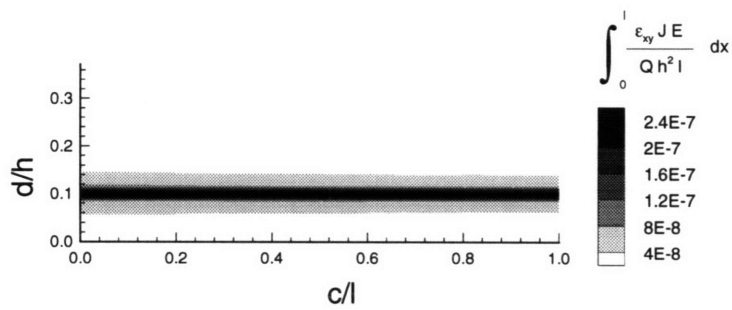


Figure 6-10: ϵ_{xy} Sensitivity map at sensor position $f/h = 0.1$

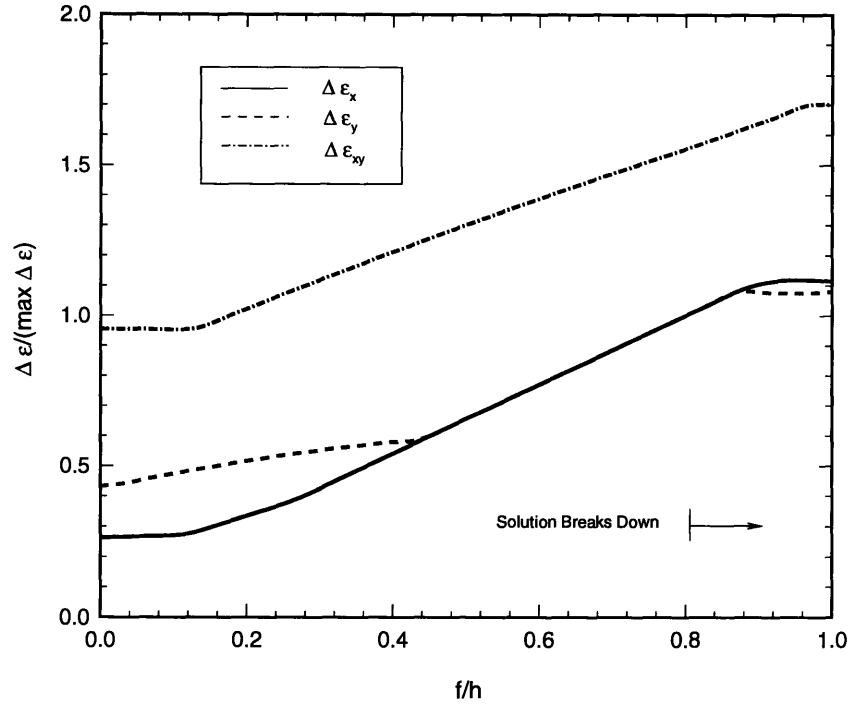


Figure 6-11: Effect of sensor position on theoretical sensor reliability.

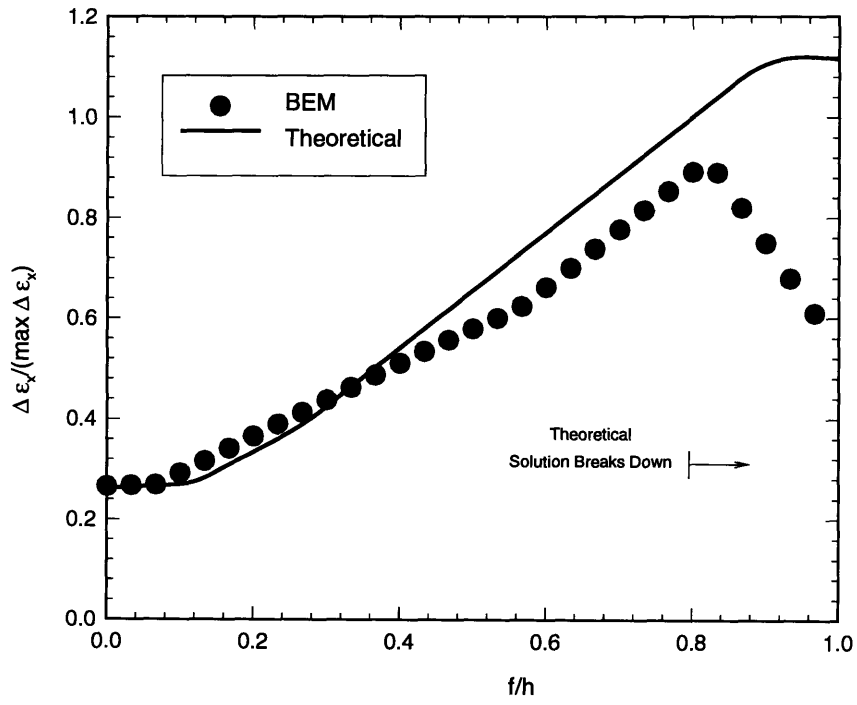


Figure 6-12: Effect of finite beam depth on ϵ_x sensor reliability.

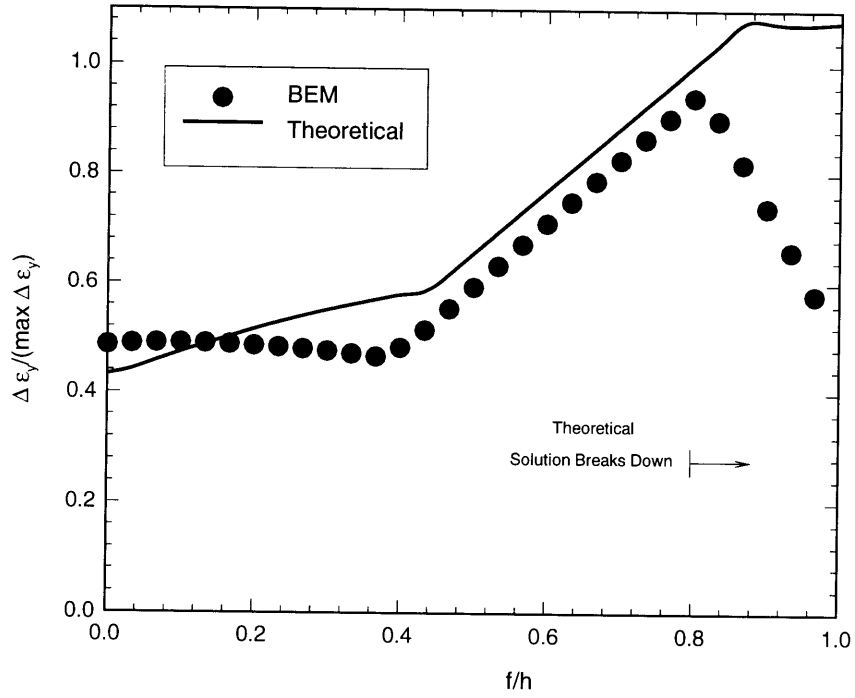


Figure 6-13: Effect of finite beam depth on ϵ_y sensor reliability.

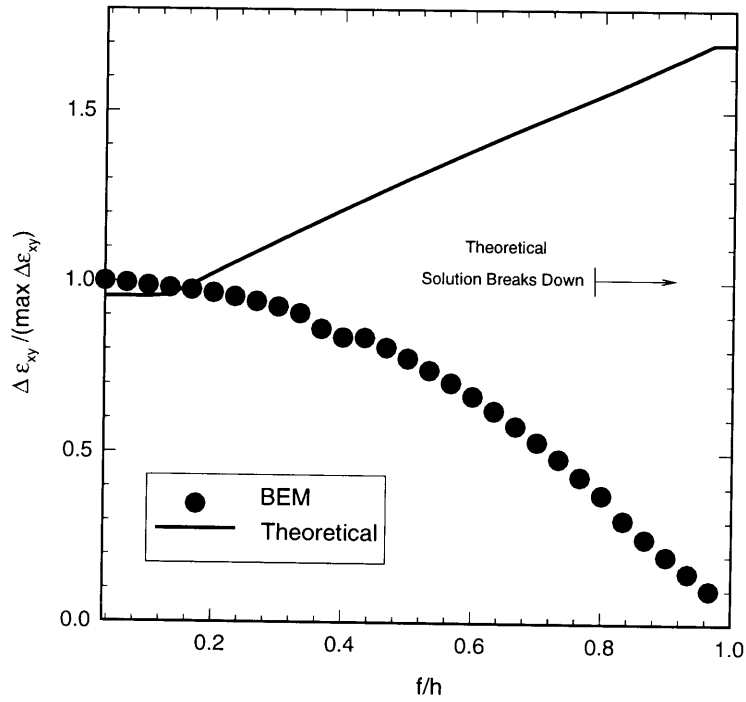


Figure 6-14: Effect of finite beam depth on ϵ_{xy} sensor reliability.

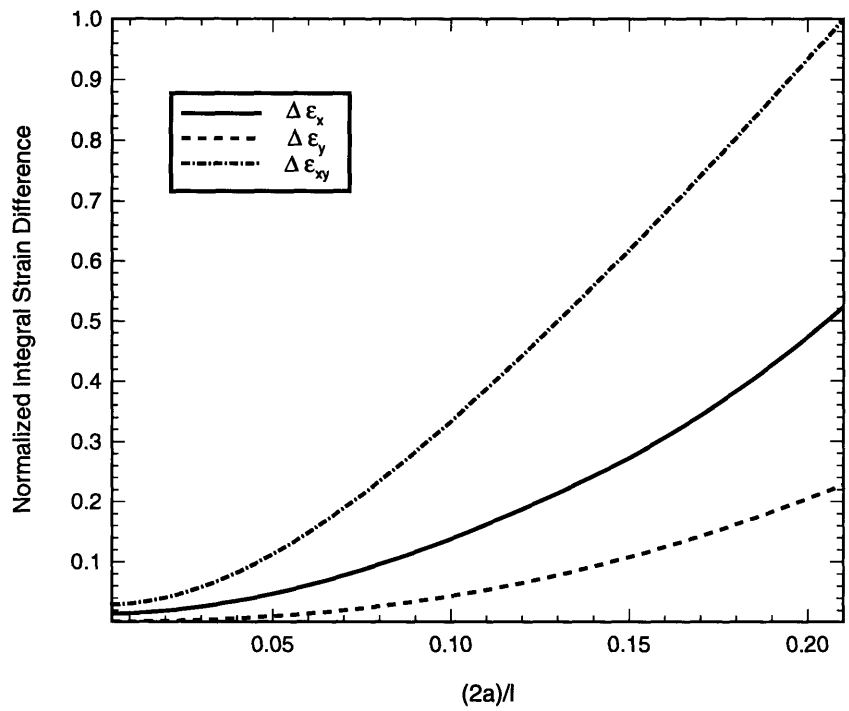


Figure 6-15: Effect of crack length $(2a)$ on sensor reliability. Normalizing parameter is the maximum shear sensitivity component.

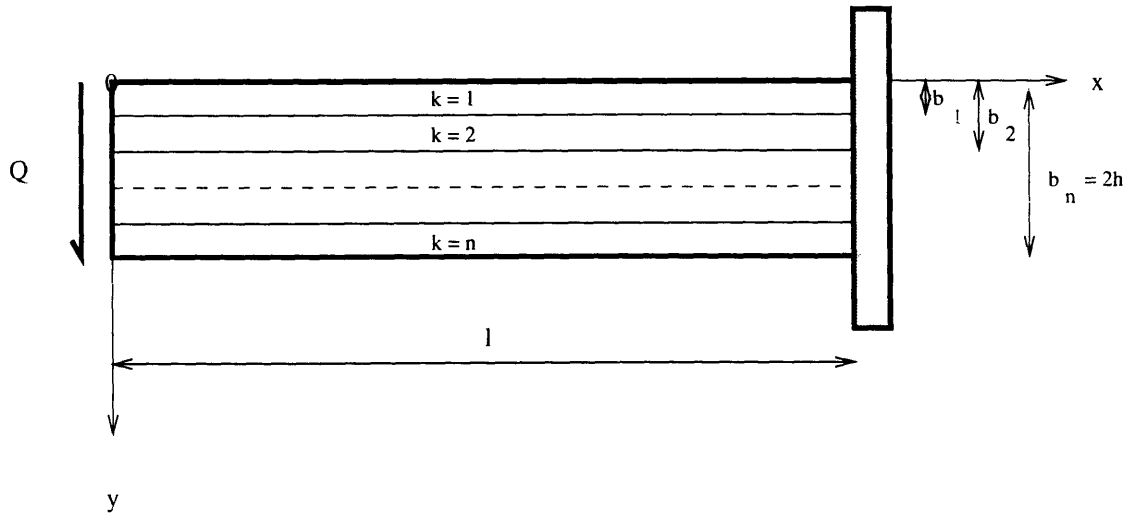


Figure 6-16: Schematic layout of laminated cantilever beam.

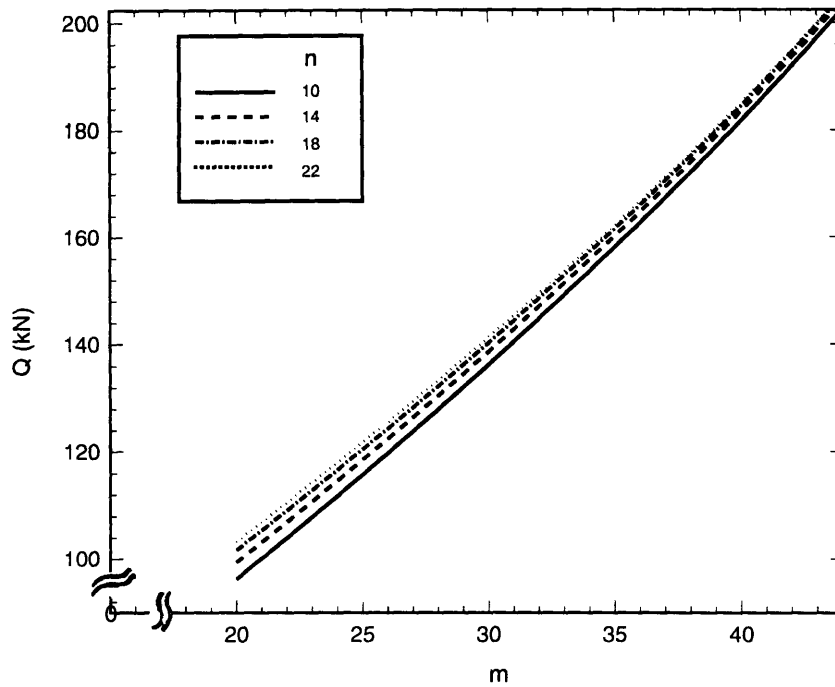


Figure 6-17: Allowable applied load of $[0_m / \pm 45_n / 90_k]_s$ laminate. $k = 100 - m - 2n$

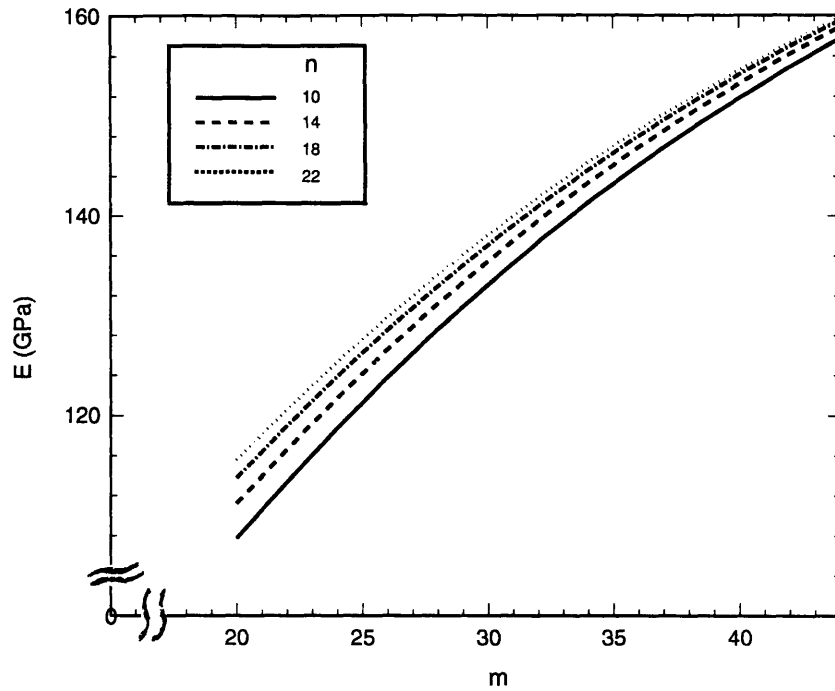


Figure 6-18: Engineering elastic modulus of $[0_m/\pm 45_n/90_k]_s$ laminate. $k = 100-m-2n$

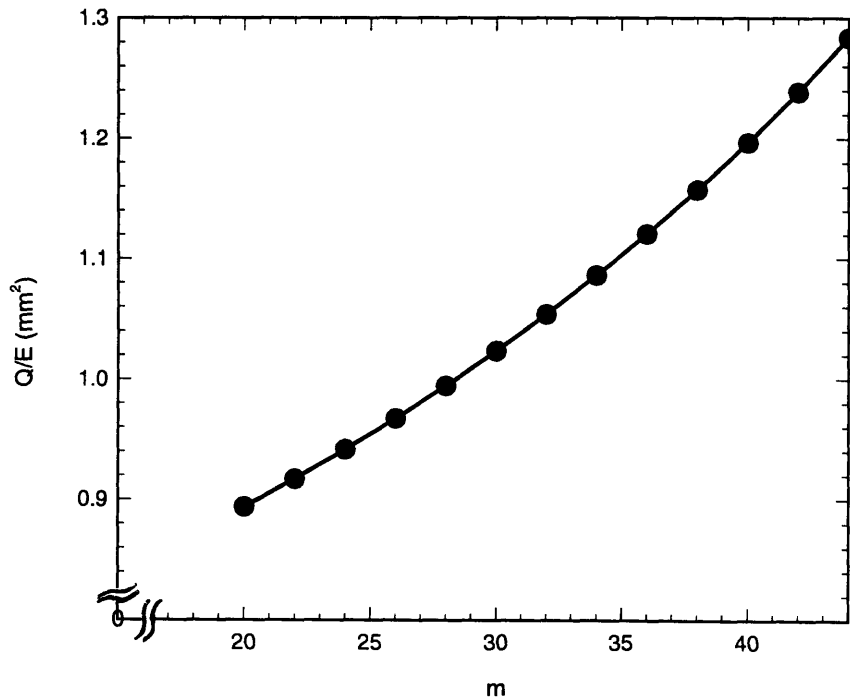


Figure 6-19: Load to elastic modulus ratio for all n of $[0_m/\pm 45_n/90_k]_s$ laminate. $k = 100-m-2n$

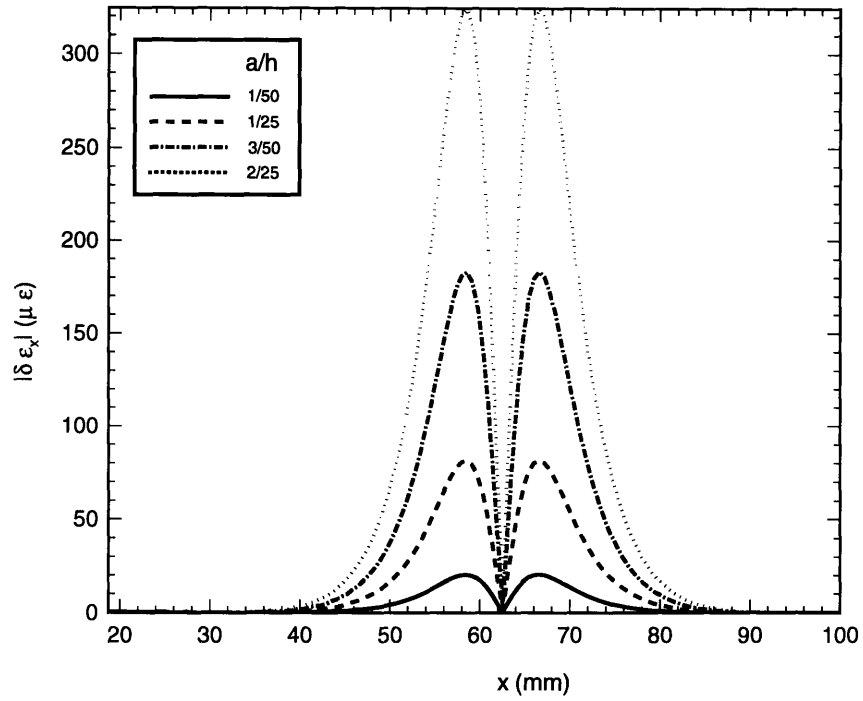


Figure 6-20: Effect of crack length (a) on the strain difference ($\delta\epsilon_x$) for delaminated beam. Crack position at beam mid-point $c = 62.5$ mm and $d = 0$. Fiber position at $f = 0.8 h = 10$ mm.

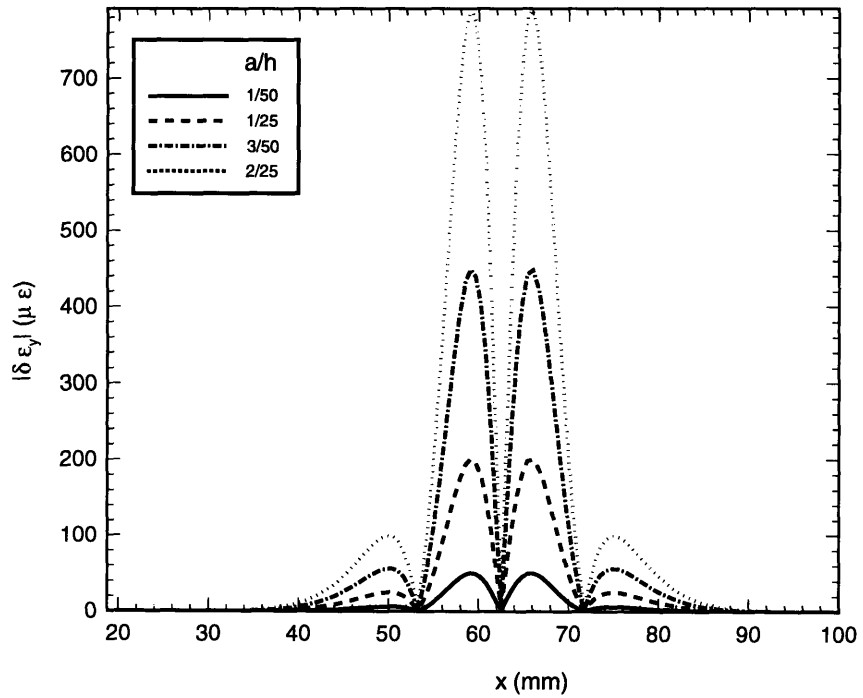


Figure 6-21: Effect of crack length (a) on the strain difference ($\delta\epsilon_y$) for delaminated beam. Crack position at beam mid-point $c = 62.5$ mm and $d = 0$. Fiber position at $f = 0.8h = 10$ mm.

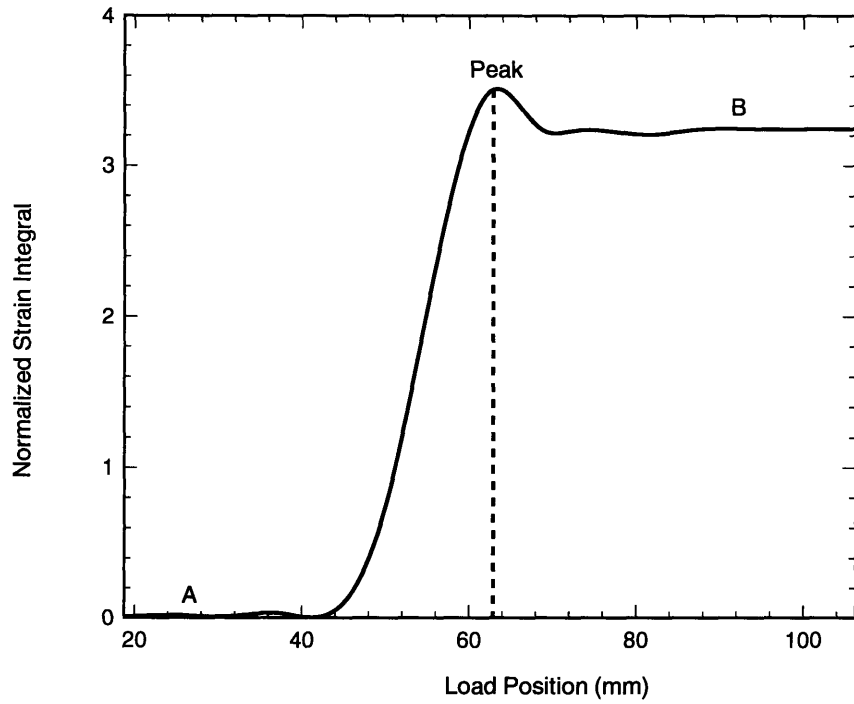


Figure 6-22: Influence line for normalized sensitivity ($\delta\epsilon_y$). Crack Length $a = 1$ mm. Crack Position $c = 62.5$ mm. Fiber position at $f = 22.5$ mm. Normalizing sensitivity given by Calero sensor of $5\mu\epsilon$ over 152 mm.

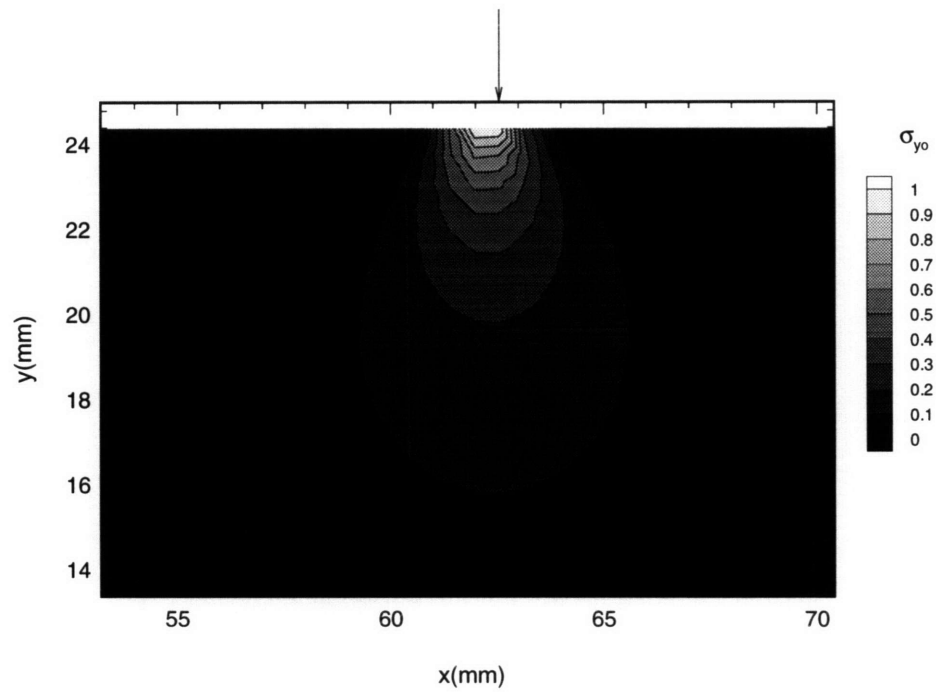
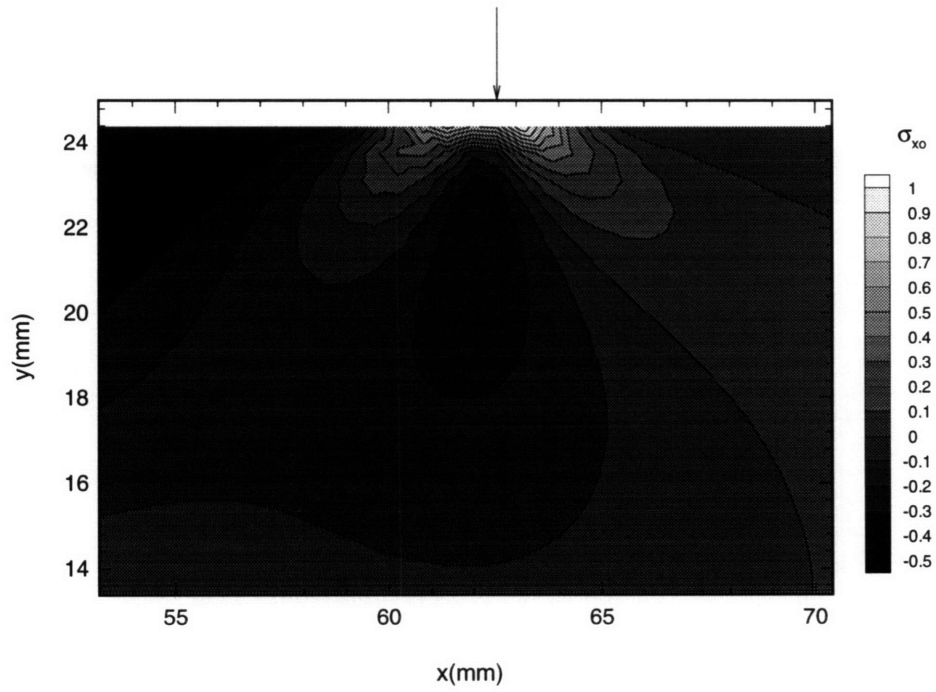


Figure 6-23: Normalized stresses under point load acting on unweakened beam. Normalizing factor taken as the maximum stress.

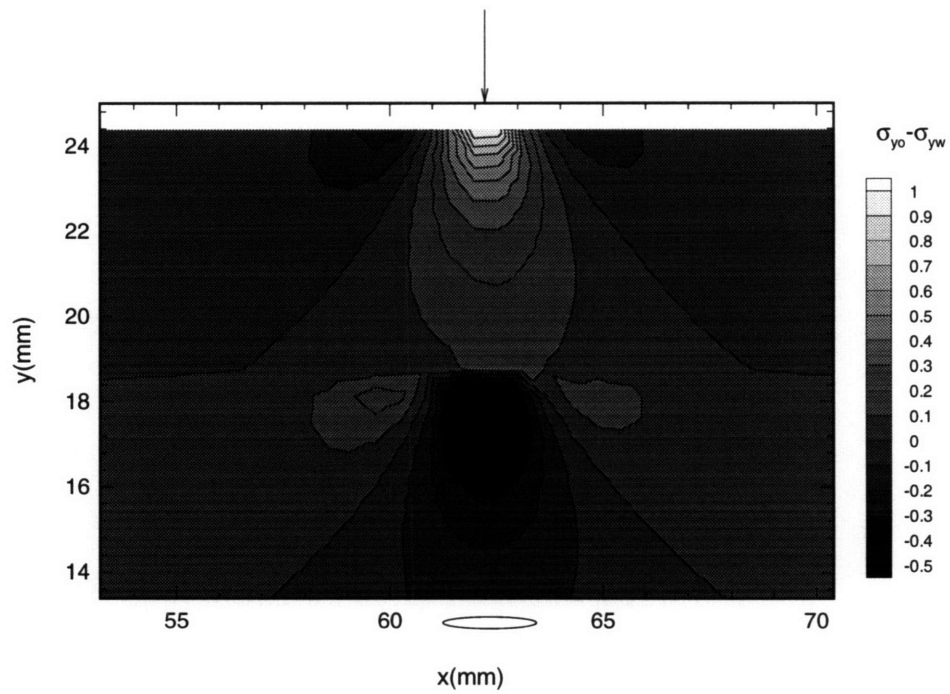
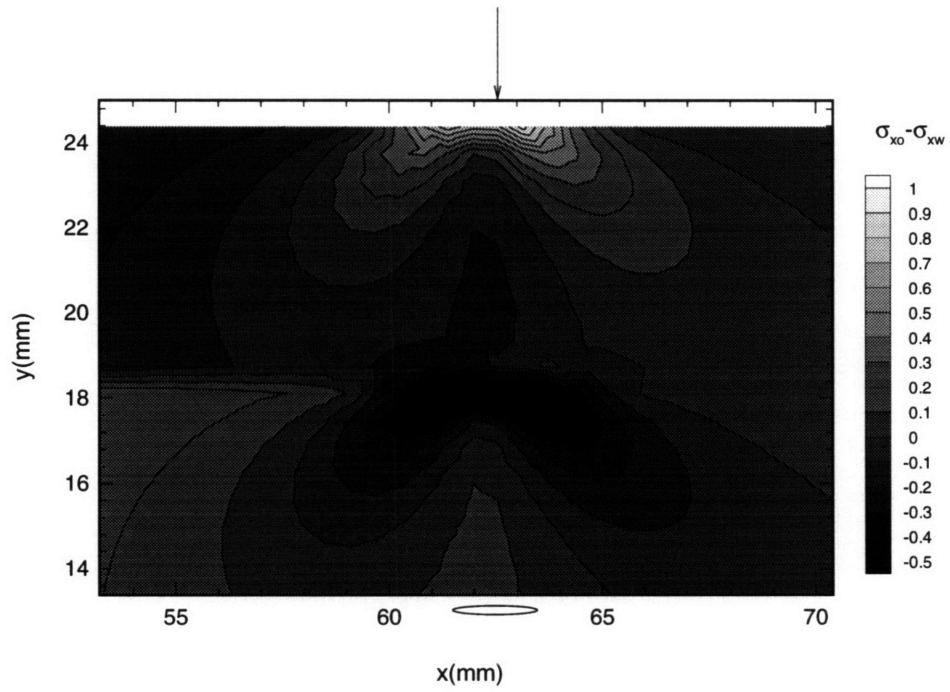


Figure 6-24: Normalized stress difference between cracked and uncracked beam subjected to point load. Normalizing factor equal to maximum stress difference.

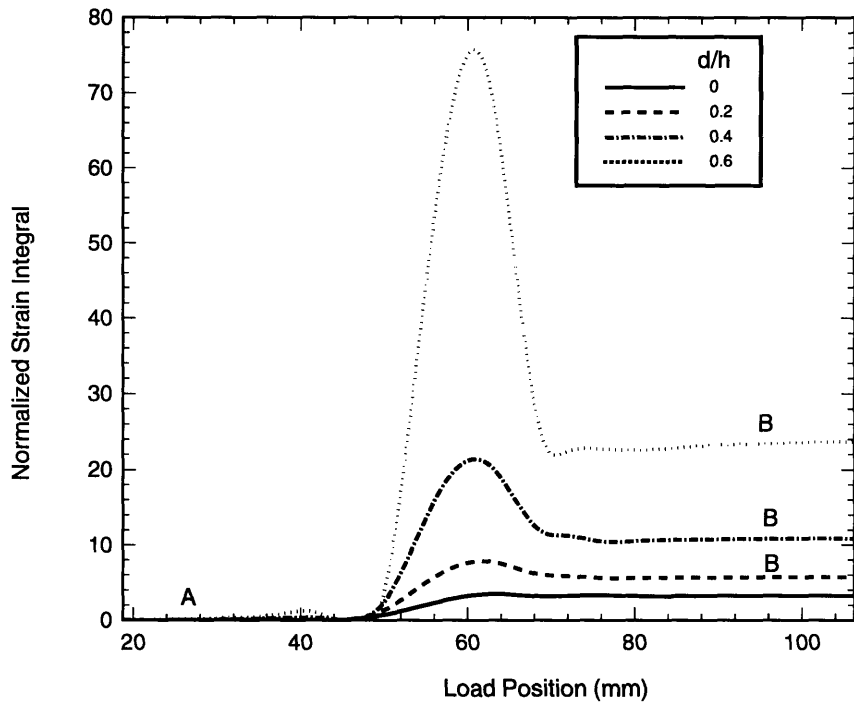


Figure 6-25: Influence lines for normalized sensitivity ($\delta\epsilon_y$) for various crack heights d/h . Beam height $h = 25$ mm. Crack Length $a = 1$ mm. Normalizing sensitivity given by Calero sensor of $5\mu\epsilon$ over 152 mm.

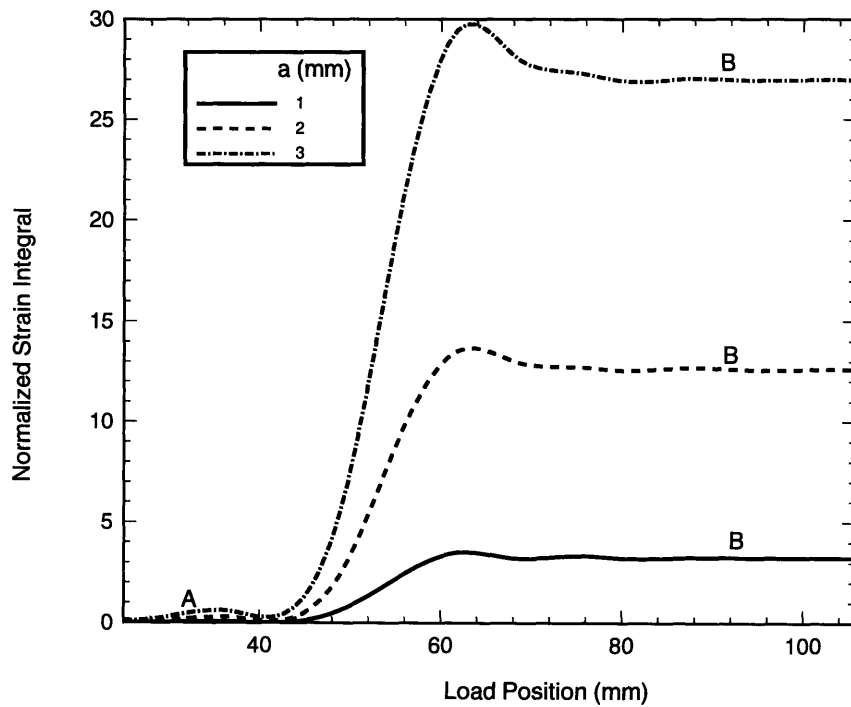


Figure 6-26: Influence lines for normalized sensitivity for various crack lengths a . Crack position $c = 62.5$ mm. Crack depth $d = 0$ mm. Normalizing sensitivity given by Calero sensor of $5\mu\epsilon$ over 152 mm.

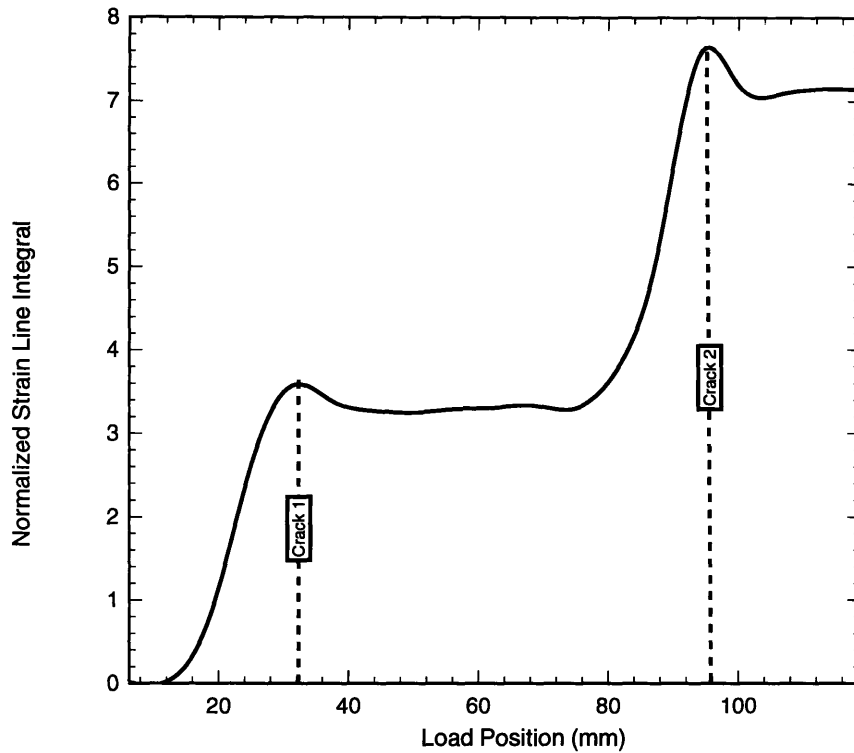


Figure 6-27: Influence lines for normalized sensitivity ($\delta\epsilon_y$) for two cracks. Crack positions at $c_1 = 31.25\text{mm}$ and $c_2 = 93.75\text{mm}$. Crack depths at $d = 0\text{mm}$. Crack lengths $a = 1\text{mm}$. Normalizing sensitivity given by Calero sensor of $5\mu\epsilon$ over 152 mm.

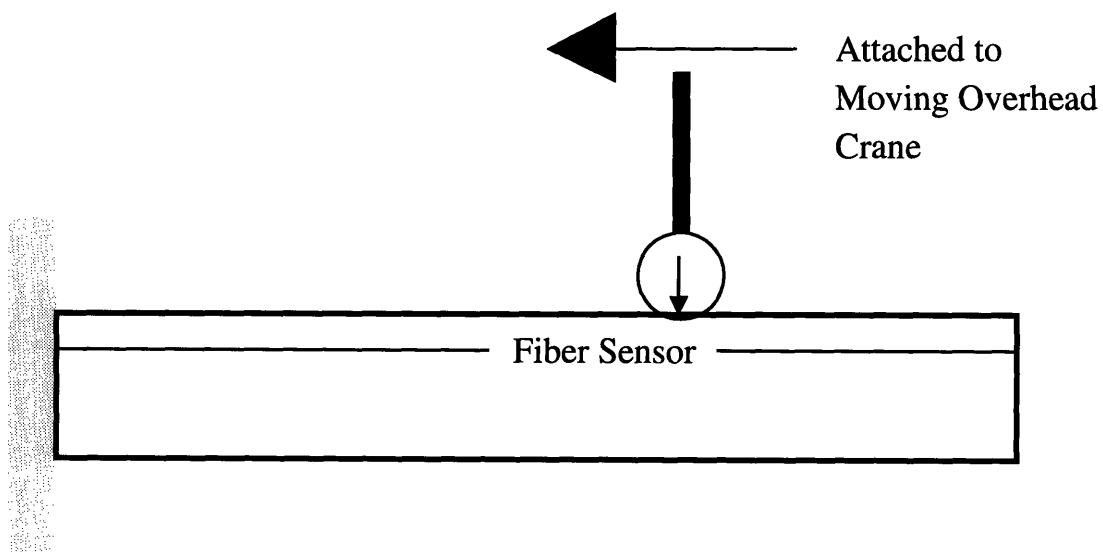


Figure 6-28: Schematic representation of a moving load test for an aircraft component.

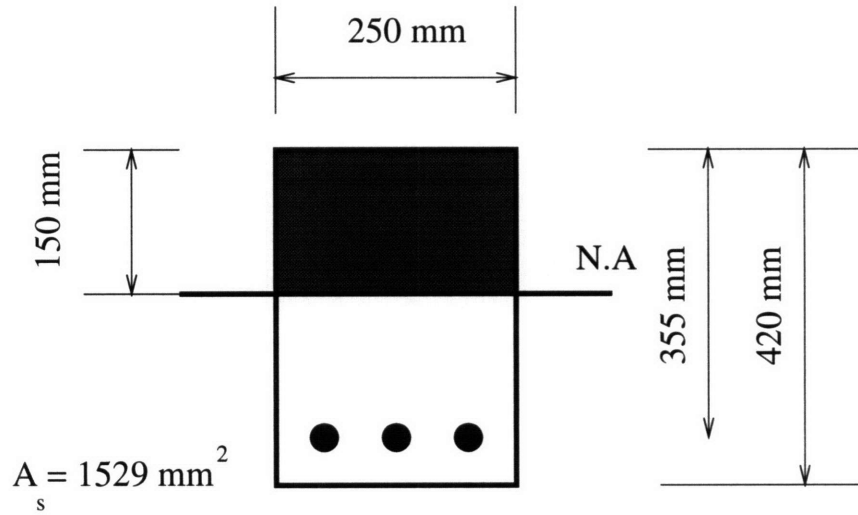


Figure 6-29: Reinforced concrete cross section.

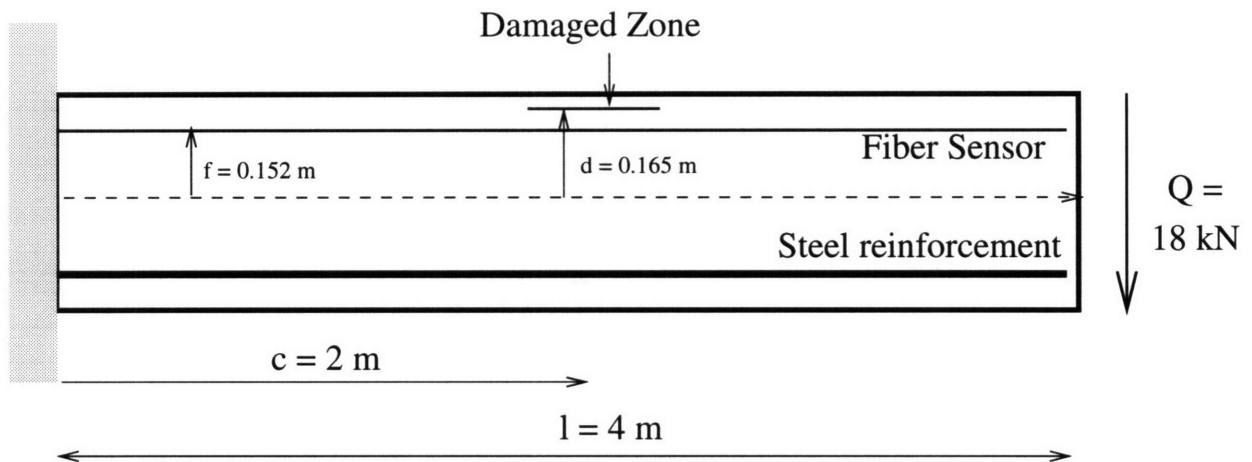


Figure 6-30: Reinforced concrete beam and sensor layout.

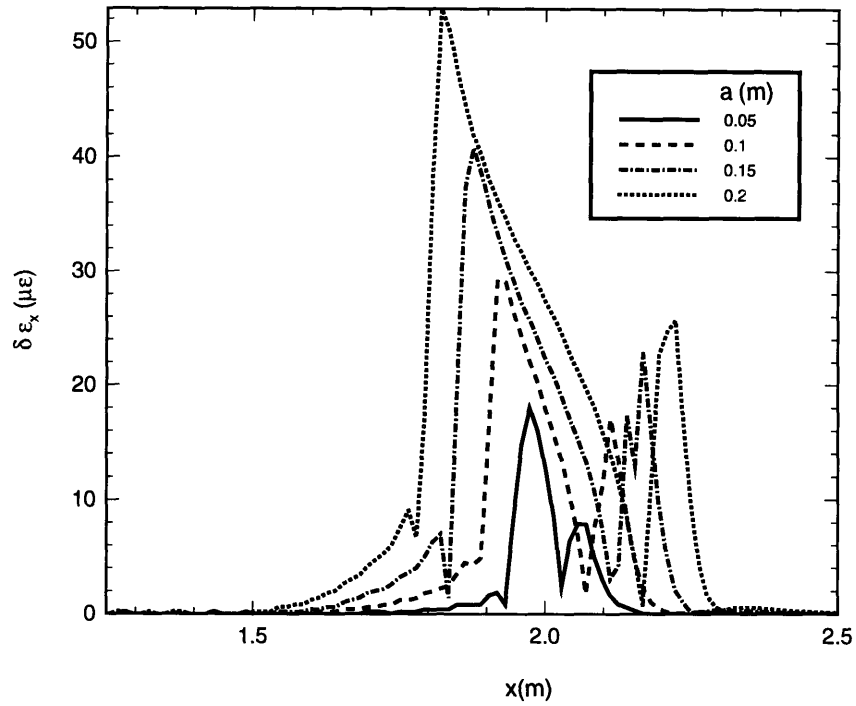


Figure 6-31: Effect of crack length (a) on the strain difference ($\delta\epsilon_x$) for delaminated concrete beam. Crack position at $c = 2$ m and $d = 0.165$ m . Fiber position at $f = 0.8 h = 0.152$ m.

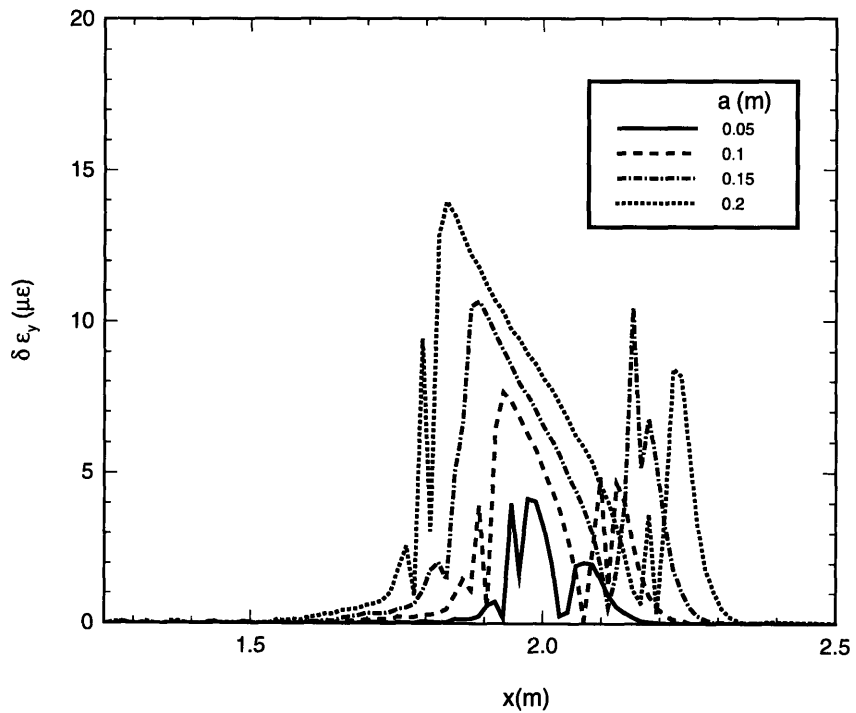


Figure 6-32: Effect of crack length (a) on the strain difference ($\delta\epsilon_y$) for delaminated concrete beam. Crack position at $c = 2$ m and $d = 0.165$ m . Fiber position at $f = 0.8 h = 0.152$ m.

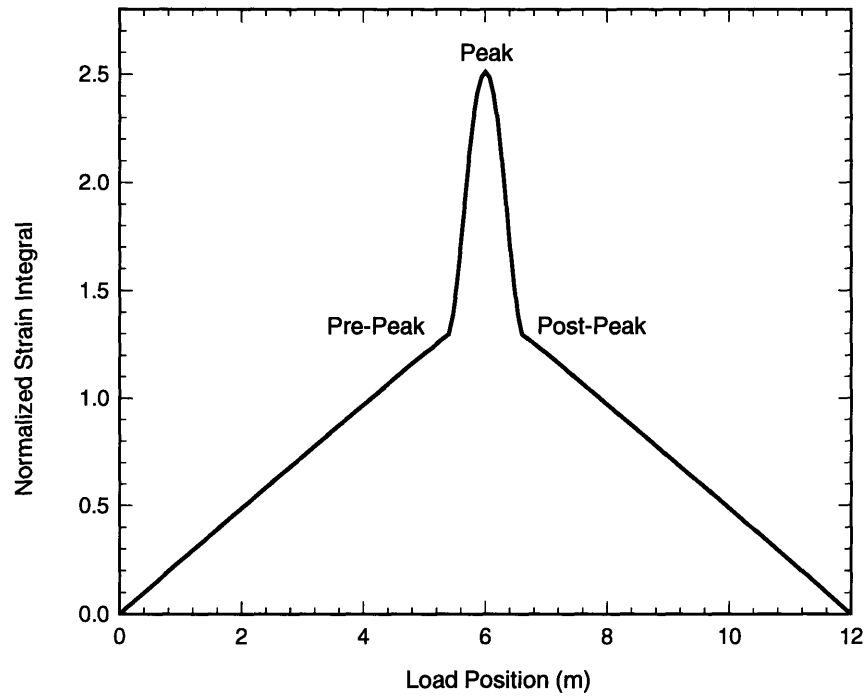


Figure 6-33: Influence lines for normalized sensitivity ($\delta\epsilon_y$) for a simply supported beam. Crack position at $c = 2m$. Crack depths at $d = 0.165 m$. Fiber position at $f = 0.8 h = 0.152 m$. Normalizing sensitivity given by Calero sensor of $5\mu\epsilon$ over 152 mm.

Chapter 7

Conclusion

The work presented in this thesis has concentrated on characterizing the behaviour of fiber optic sensors used for integrity and damage monitoring in civil and aerospace applications. Numerical and theoretical techniques have been implemented for the analysis of combined mechanical and electromagnetic behaviour of fiber optic sensors. For tensions cracks which typically occur in concrete structures, a microbend sensor which bridges the crack faces was shown to be capable of determining the extent of damage by monitoring sensor power loss caused by increasing crack opening displacements. The sensing capability of a microbend fiber optic sensing system was found to be dependent on (a) crack opening displacement, (b) optical characteristics of the fiber, (c) fiber jacket stiffness, and (d) fiber inclination angle at the crack face. The microbend sensor was found to be able to detect cracks in the 0.01 mm range which makes them ideal for the inspection of civil engineering structures which have strict crack opening restrictions for leak protection (e.g. in dams and hazardous waste containment structures) and durability (e.g. in bridges).

Birefringent and interferometric sensors were studied for the detection of delamination damage in advanced aerospace composites, and the similar debonding damage typical of reinforced concrete structures. The success of a delamination damage detection scheme has been found to depend on (a) position of the delaminated zone, (b) position of the sensor, (c) optical sensitivity of the fiber, (d) length of delami-

nated zone, (e) applied test load and (f) elastic modulus of the structure. A simple moving point load test has been proposed that can detect the position and extent of the damage as well as the number of damaged zones. For advanced aerospace composites, delamination lengths less than 1 mm can be detected which makes the proposed sensor system suitable for the monitoring of delamination damage in flexural aerospace components such as helicopter rotor blades and wings. In reinforced concrete structures, debonding damage lengths in the 0.1 meter range can be detected by the proposed delamination sensors allowing for the monitoring of damage which often plagues typical reinforced concrete structures (e.g. bridges, heavy vehicle support beams such as in parking garages and highways).

Future research in microbend sensors should concentrate on (1) verification of the theoretical results with experiments, (2) extension of the electromagnetic analysis to include general three dimensional optical behaviour and multi-mode behaviour, (3) extension of mechanical analysis to account for possible plastic behaviour of the jacket material and spalling of the concrete matrix, and (4) development of techniques for the effective coupling of the fiber sensor to a real world concrete structure.

Future research in delamination detecting optical fiber sensors should concentrate on (a) verification of theoretical results through experimentation, (b) extension of the mechanical analysis to include the non-linear behaviour of crack closure and quantification of crack closure on damage detectability, (c) extension of the physical model to include the effects of realistic three-dimensional delamination zones and (d) accounting for material anisotropy.

Appendix A

BPM Example Problem

The objective of this section is to explain the FFT BPM by means of an example problem. The problem consists of calculating the power loss associated with propagation along a curved step index mono-mode slab waveguide. The geometry and optical properties are as follows :

- Refractive index of waveguide core $n_1 = 1.4613$
- Refractive index of waveguide cladding $n_2 = 1.458$
- Light wavelength $\lambda = 1.3\mu m$.
- Slab width $2a = 6\mu m$.
- Radius of curvature $R = 5mm$.
- Wavenumber $k_0 = \frac{2\pi}{\lambda} = 4.83/\mu m$.

Calculation of the input straight fiber fundamental mode.

This section calculates the input electric field into a straight waveguide for the monomode fiber.

1. Check if fiber is monomode by calculating $v \leq \frac{\pi}{2}$.

$$v = ka\sqrt{n_1^2 - n_2^2} = 1.42 < \frac{\pi}{2}$$

Hence fiber is monomode

2. Calculate the base refractive index n_a by solving the non-linear equation

$$\sqrt{n_1^2 - n_a^2} \tan(ka\sqrt{n_1^2 - n_a^2}) = \sqrt{n_a^2 - n_2^2}$$

giving $n_a = 1.460$

3. Unit normalize the input electric field ϕ by setting $A_1 = 1$ so that

$$\phi_1 = \cos(k\sqrt{n_1^2 - n_a^2}x)$$

for $|x| < a$

4. Calculate A_2 from

$$A_2 = A_1 \frac{\cos(k\sqrt{n_1^2 - n_a^2}a)}{e^{-k\sqrt{n_a^2 - n_2^2}a}}$$

giving $A_2 = 1.9$

5. Total input field is given by

$$\phi_1 = \cos(k\sqrt{n_1^2 - n_a^2}x)$$

for $|x| < a$

$$\phi_2 = A_2 e^{-k\sqrt{n_a^2 - n_2^2}x}$$

for $|x| > a$

Figure (A-1) shows the distribution of the input electric field.

BPM

This section outlines the steps in calculating the electric power distribution for a constant curvature waveguide by means of the BPM.

1. Transform refractive index by using

$$n_i^{new} = n_i^{old} \left(1 + \frac{x}{R}\right)$$

the old and transformed refractive index is shown in figure (A-2).

2. Discretize the propagation length into discrete steps. Here $\Delta z = 2\mu m$.
3. Discretize the slab width (computational window) into a power of 2 number of interval points (n) for efficient FFT computation. Here $n = 128$.
4. FFT the input signal to find ϕ_n . The discrete fourier transform of the input signal is given in figure (A-3). Note that there is no imaginary component since the input electric field is symmetric and thus even.
5. Propagate the fourier transformed electric signal through an homogenous medium with an effective index n_a and over a length $\Delta z/2$, giving ϕ_n^-

$$\phi_n^-(z + \Delta z/2) = \exp\left(j \frac{\Delta z}{2} \frac{k_{xn}^2}{2n_a k}\right) \times \phi_n(z)$$

6. Phase shift the propagating wave through a thin lens giving ϕ_n^+

$$\phi_n^+(z + \Delta z/2) = \exp\left(-j \Delta z \frac{k(n_i^2 - n_a^2)}{2n_a}\right) \times \phi_n^-(z + \Delta z/2)$$

7. Inverse FFT the propagating wave to find the electric power $\phi^+(z + \Delta z/2)$.
8. Absorb the electric field at the computational window edge in order to prevent aliasing problems. For a full discussion of this procedure see for example Baets and Lagasse [1].

9. Repeat steps (5) to (8) until the required propagation distance has been reached.
For the case of a 3 mm propagation length and radius of curvature 5 mm, the output electric field is shown in figure (A-4).

Bibliography

- [1] R. Baets and P.E. Lagasse. *Loss calculations and design of arbitrary curved integrated-optic waveguides*. J. Opt. Soc. Am. **73**. 177-182 (1983)

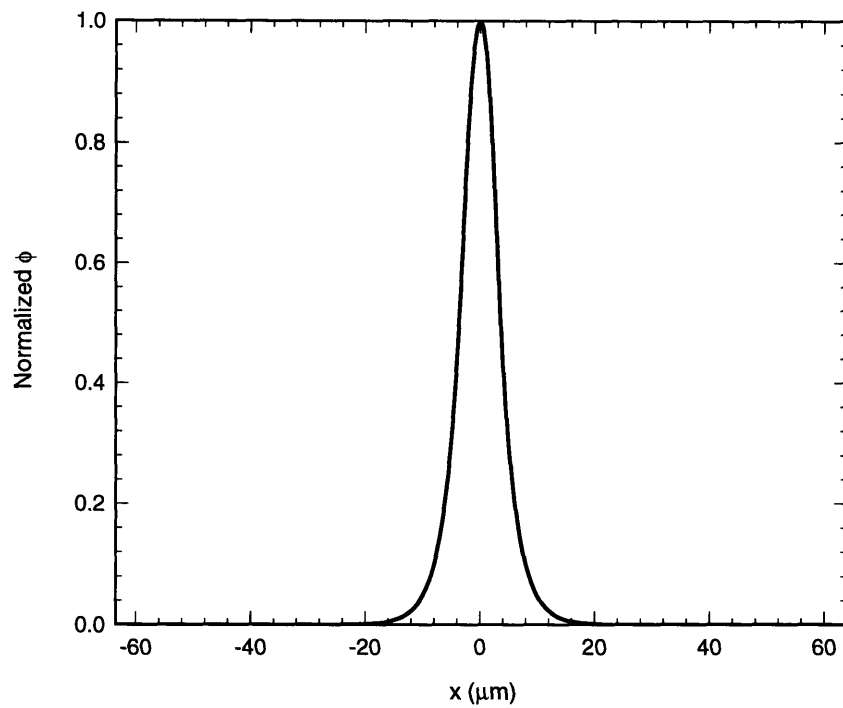


Figure A-1: Input fundamental mode for a straight slab waveguide.

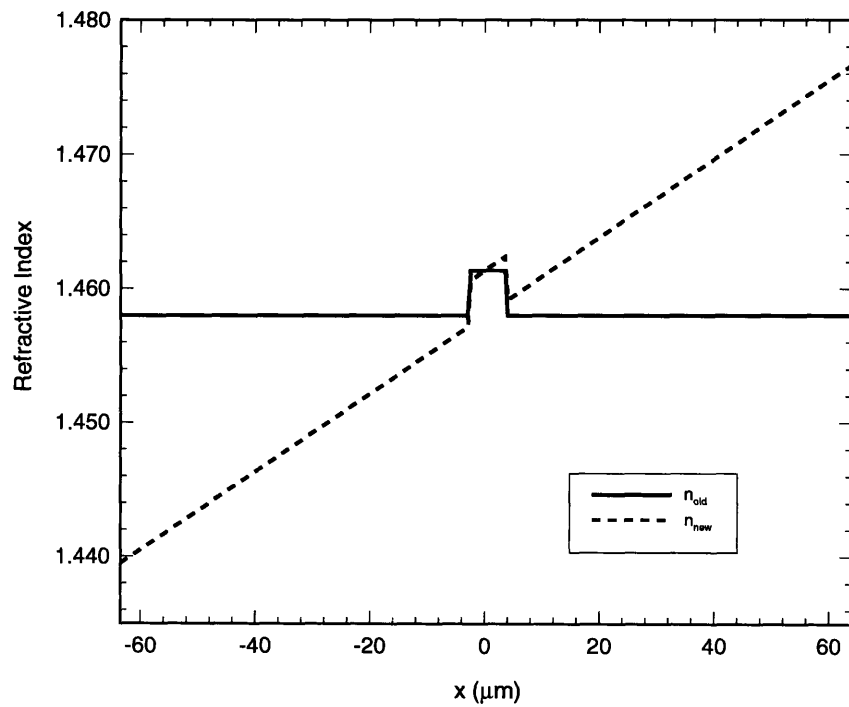


Figure A-2: Input and transformed waveguide index.

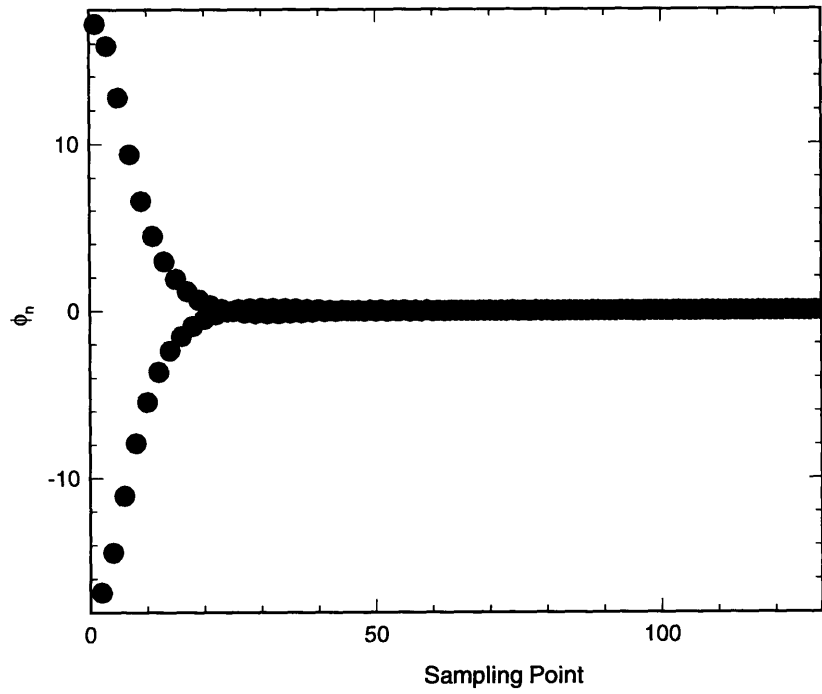


Figure A-3: FFT components of the input electric field.

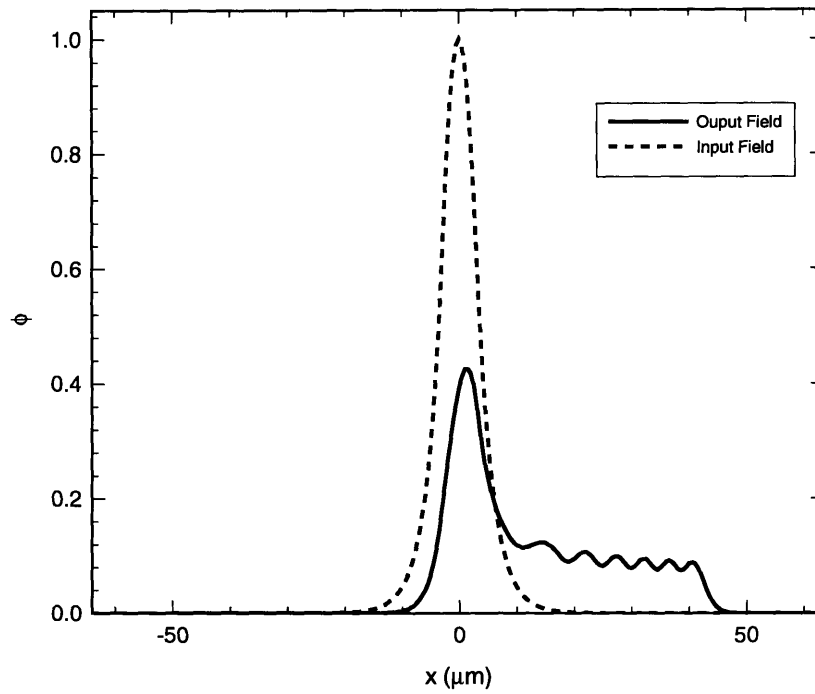


Figure A-4: Output electric field after propagation of 3 mm in a 5 mm radius of curvature fiber.